Analyse quantitative des propriétés mécaniques de fraises dentaires rotatives en NiTi et étude de la fabrication de larges microstructures par polymérisation induite à deux photons

Chao Yuan Liu

UNIVERSITÉ DE GRENOBLE

THÈSE

Pour obtenir le grade de

DOCTEUR DE L'UNIVERSITÉ DE GRENOBLE

préparée dans le cadre d'une cotutelle entre l'*Université de Grenoble* et National Taiwan University

Spécialité : **Physique-Physique Appliauee**

Arrêté ministériel : le 6 janvier 2005 -7 août 2006

Présentée par

« Chao Yuan LIU »

Thèse dirigée par **« Patrice BALDECK »**
codirigée par **« Chow Shing SHIN »**

préparée au sein des **Laboratoires LiPhy et Fatigue Lab**

dans **l'Ecole doctarle de Physique de Grenoble et Colledge of Engineering, National Taiwan University**

Analyse quantitative des propriétés mécaniques de fraises dentaires rotatives en NiTi et étude de la fabrication de larges structures microstructurées par polymérisation induite a deux photons

Thèse soutenue publiquement le **« 18/07/2014 »**,
devant le jury composé de :

M, Patrice, BALDECK
Directeur de recherche au CNRS-UJF-Grenoble, Directeur de thèse
M, Chow Shing, SHIN
NTU, Taiwan, Codirecteur de thèse
M, Kevin, HEGGARTY
Brest Telecom, Brest, Rapporteur et Membre
M, Ming Chuen, YIP
NTHU, Taiwan, Rapporteur et Membre
M, Tien Tung, CHUNG
NTU, Taiwan, Membre
M, Marc, JOYEUX
LiPhy, Grenoble, Membre

Université Joseph Fourier / Université Pierre Mendès France / Université Stendhal / Université de Savoie / Grenoble INP

CONTENTS

Acknowledgement

First and foremost, I would like to show my deepest gratitude to my supervisors, Pr. Chow-Shing SHIN and Pr. Patrice BALDECK. They led me into the world of fracture analysis and two-photon induced polymerization, providing an excellent environment to practice my learning. Without their training, I cannot have such wide and strong background as well as a serious attitude towards research. I would also like to thank Pr. C.-L. LIN, Pr. C.-P. LIN for their interests in my study and being an integral part of the dissertation committee.

I appreciate Pr. Chow-Shing SHIN and Pr. Chih-Lang LIN, they helped me to get the Fourier dual degree scholarship, giving me the chance to study abroad in France to sharpen my academic skills. Also, I appreciate Pr. Patrice BALDECK, who taught me photon-induced polymerization. With his great help, let me learn how to perform an interesting research and analyze the results. I would also like to thank J. SITBON, M. BOURIAU, L. GREDY, Y.-H. Hsueh and other members of Laboratoireinterdisciplinaire de Physique (LiPhy), I really enjoy the cooperation with team in Grenoble, France. I want to specially thank Pr. Olivier Stephan for the development of stable photopolymer and Y-H Hsueh for the development of software controlled system. Under their great help, the experiment has good repeatability and reliability.

Here, I want to list the members in Lab who contributed their experiences when I implemented researching projects: S.-E. HUANG, C.-T.LIN, T. MHALLA, J.-P.MALVAL. They helped me a lot during the project periods or in TPP study. I am also grateful to the other young members in our laboratory. Workings with them are joyful.

Finally, I would like to express my deep gratitude to my girlfriend Claire and both of our parents for their unconditional support and encouragement. With their strong support, I can concentrate on my PhD study. I love my family very much.

Chao-Yuan LIU written on June 1st, 2014

ABSTRACT

One third of dental emergencies and a high percentage of toothaches are endodontics related. Rotary instruments employed in endodontic treatment may break inside the root canal due to material fatigue. Once broken, extracting the fractured part from the canal is a difficult job and is annoying to both the patient and the dentist. Therefore, warning of an imminent fracture during clinical use or developing good strategies to increase its mechanical properties will be a great help to avoid medical/ legal complications.

The research is studied from two parts. The first part established a standard testing platform, simulating several root canal parameters, proposing a series of strategies to improve the fatigue life and material's mechanical properties. Also, a monitoring system employing Fiber Bragg Grating (FBG) sensors has been attempted. The reason of using FBG is its small size which is very promising in integrating with the handpiece of the endodontic equipment. In the current work, by picking up and analyzing the stress wave through Fast Fourier Transform (FFT), we can reveal the energy variation and the frequency shifting phenomenon under some characteristic frequencies. It is hoped that with these information, we can avoid/alleviate the occurrence of unexpected fracture. As for the fatigue test, data showed that the fatigue life can be improved when certain heat treatment or reciprocating rotation method applied. Such phenomenon may be closely related to the phase composition in Ni-Ti Alloy and the maximum tension stress is decreased when reciprocating movement applied. Studies showed that the more content of martensite phase in the needle, the more fatigue life can be achieved. However, it may need to take compromise with needle's cutting efficiency. For this issue, we can combine cryogenic treatment and heat treatment to get better fatigue life without compromising with its cutting efficiency.

The second part is to fabricate high resolution, large size of new type endodontic needles by employing two-photon polymerization (TTP) technique. The work is done in the university of Joseph-Fourier LiPhy lab, France. Unlike traditional TPP manufacturing, which had a limitation of its products size due to small lase power, repetition rate and piezo driven stage, we use Ormocer resin, 130 kHz, 1W powerful 532 nm laser with step motor driven X-Y stage to fabricate high bio-compatible 800 μm cell scaffold and 1.2 cm height needle. Also, to improve the product quality of TPP, the laser power correction approach had been attempted. During TPP fabrication, the laser focusing shape changed when the fabrication surface was moved up in z direction. This results in that we need more power to ensure the voxel size is the same at different z. To correct such defect, a method of the laser power correction and

formula for the correcting power are proposed. The formula is derived from the concept of keeping exposure condition the same.

Keywords: Ni-Ti rotary instrument, root canal parameter, FBG, characteristic frequency, reciprocating movement, martensite phase, cryogenic treatment, two-photon polymerization, Large size of TPP, scaffold, laser correction method.

LIST OF FIGURES

LIST OF TABLES

Chapter 1 Introduction

Ni-Ti rotary instruments in endodontic treatments are used to remove the disease tissue and nerves in the curved root canals [1]. As a result, the instrument is under simultaneous rotation and bending during operation and is prone to break inside the root canal through metal fatigue. Although investigations into various aspects of rotary instrument fracture exist, no effective way has as yet been drawn up to prevent such failure. Therefore, we proposed several heat treatments to improve material properties, Fiber Bragg Grating (FBG) sensors based monitoring system to warn before fracture and use two-photon polymerization (TPP) method to develop new type of needles in the end. In this chapter, we reviewed the basic principle of metal fatigue in rotary endodontic instruments, FBG sensor, TPP fabrication process and some related controversial papers,

1.1 Introduction of root canal therapy

The outermost structure of human teeth is enamel and the next layer is dentine, which is coated on the pulp chamber. Pulp cavity contains blood vessels, nerves and lymphatic vessels. Its narrow cavity is so called the root canal, as shown in Fig.1-1[1]. The purpose of root canal therapy is to clean the lesion pulp (nerves) to prevent from further spread of infections[2]. In addition to reducing the patient's pain, such therapy not only maintains the natural teeth but also satisfy the aesthetic demands [3]. The main steps of root canal treatment are as follows:

i. Gain entry to the pulpal chamber

ii. Removal of pulp tissue and moisture from the canal

iii. Fill the canal to avoid bacterial growth

iv. Restore the tooth back to its original form

Root canal treatment early use of stainless steel equipment is now gradually being replaced by nickel-titanium material rotary instruments, since its super-elasticity and superior compliance made the negotiation of the curved canals and as a result the root treatment a lot easier.

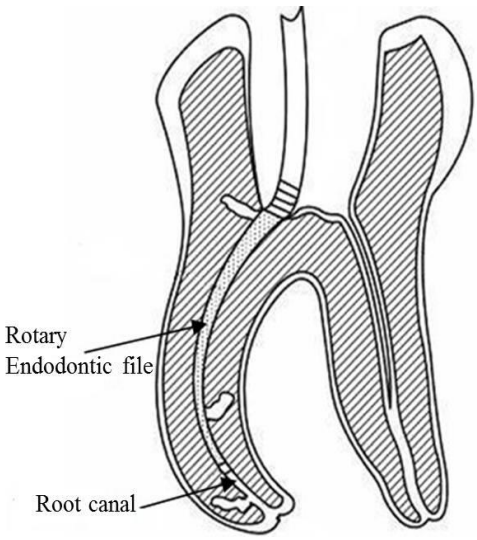

Fig.1-1.Schematic diagram of a tooth showing the rotary file in root canal[1].

1.2 Introduction of Ni-Ti rotary instruments

The endodontic rotary instrument, also known as root canal filing, is made from nickel-titanium alloy. The combination ratio of nickel and titanium is a trade secret and various in different manufacturers, but according to previous studies and open access data, the current ration of the alloy is generally 51 % from nickel and 49 % from titanium in atomic scale, 56 % nickel with 44 % titanium by weight [4]. Alloy materials are first processed into a wire, then, followed by a series of processing. The process involves a complex forging, annealing and a series of rolling to have a specific taper gradient [5]. In order to increase its cutting force, surface grinding is also employed to have helical path of groove [3]. Such grooves can also have function of bringing out of the cut chips from the root canal.

1.2.1 Phase transformation

In the early 1960s, Buehler and his co-workers at the U.S. Naval Ordance Laboratory discovered the shape memory effect in an equiatomic alloy of nickel and titanium, which can be considered a breakthought in the field of shape memory materials. Since that time, intensive investigations have been made to elucidate the mechanics of its basic behavior. The basic phenomenon of the memory effect is governed by thermoelastic behavior of two temperature-dependent crystal structures, called martensite (lower temperature) and austenite (higher temperature or parent phase). Several properties of austenite Ni-Ti and martensite Ni-Ti are notably fifferent.

When martensite Ni-Ti is heated, it begins to change into austenite (see Fig.1-2.a). The temperature at which this phenomenon starts is called austenite start temperature (A_s). The temperature at which this phenomenon is complete is called austenite finish temperature (A_f). When austenite Ni-Ti is cooled, it begins to change onto martensite. The temperature at which this phenomenon starts is called martensite temperature (M_s). The temperature at which martensite is again completely reverted is called martensite finish temperature (M_f).

Composition and metallurgical treatments have dramatic impacts on the above transition temperatures. From the point of view of practical applications, Ni-Ti can have three different forms: martensite, stress-induced martensite (superelastic), and austenite. When the material is in its martensite form, it is soft and ductile and can be easily deformed (somewhat like soft

pewter). Superelastic Ni-Ti is highly elastic (rubber-like), while austenite Ni-Ti is quite strong and hard (similar to titanium) (Fig.1-2.b).

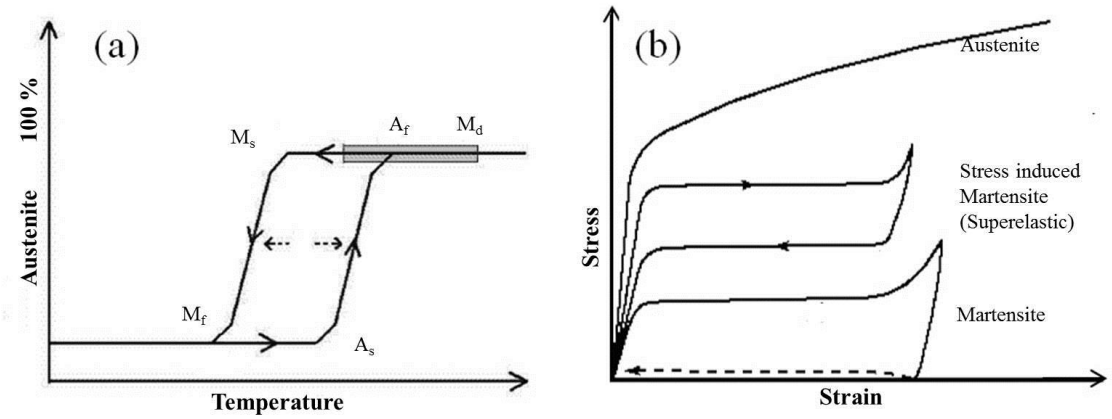

Fig.1-2. (a). Martensite transformation and hysteresis (=H) upon a change of temperature. M_d is the highest temperature to strain-induced martensite. Gray area is the area of optimal superelasticility. (b). Stress-strain behavior of different phases of Ni-Ti at constant temperature.

1.2.2 Hysteresis

The temperature range for the martensite-to-austenite transformation, i.e. soft-to-hard transition, that takes place upon heating is somewhat higher than that for the reverse transformation upon cooling (Fig. 1-2.A). This difference between the transition temperatures upon heating and cooling is called hysteresis, which is generally defined as the difference between the temperature at which the material is 50 % transformed to austenite upon heating and 50 % transformed to martensite upon cooling. Such difference can be up to 20-30 ℃[6-7]. In practice, this means that an alloy designed to be completely transformed by body temperature upon heating (A_f< 37 ℃) would require cooling to about +5 ℃ to fully retransform into martensite (M_f).

1.2.3 Shape memory effect

Ni-Ti senses a change in ambient temperature and is able to convert its shape to a preprogrammed structure. While Ni-Ti is soft and easily deformable in its lower temperature form (martensite), it resumes its original shape and rigidity when heated to its higher temperature form (austenite) (Fig.1-3). This is called the one-way shape memory effect. The ability of shape memory alloys to recover a preset shape upon heating above the transformation temperatures and to return to a certain alternate shape upon cooling is known as the two-way shape memory effect. There's also an all-round shape memory effect, which is a special case of the two-way shape memory effect [8].

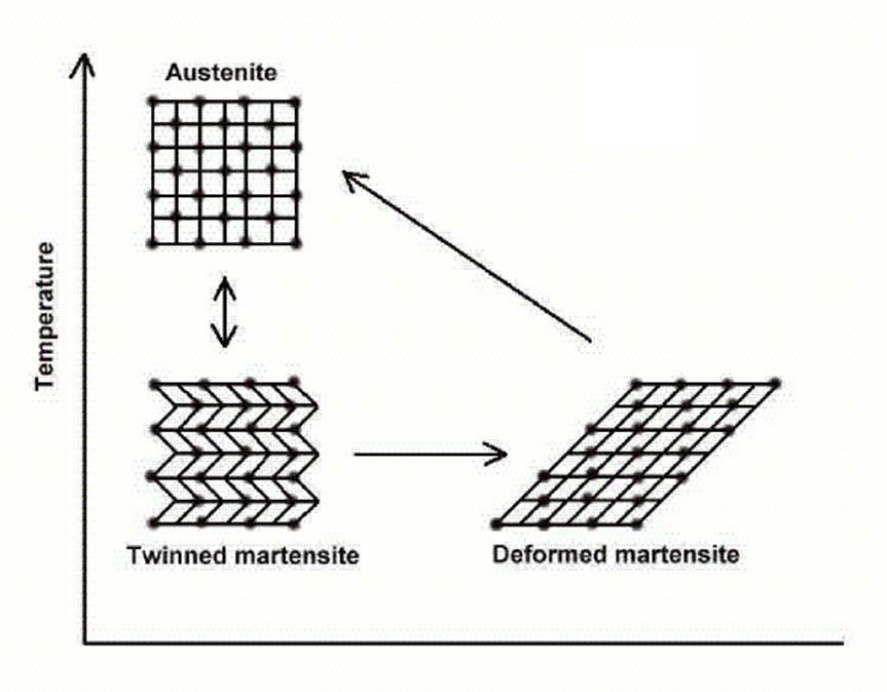

Fig.1-3.Transformation from the austenite to the martensite phase and shape memory effect.

The high-temperature austenite structure undergoes twining as the temperature is lowered. This twinned structure is called martensite. The martensite structure is easily deformed by outer stress into a particular shape, and the crystal structure undergoes parallel registry. When heated, the deformed martensite resumes its austenite form, and the macroscopic shape memory phenomenon is seen[8].

1.2.4 Fracture mechanism of Ni-Ti rotary instruments

The fracture mechanism of endodontic files can be divided into two types: torsional fracture and fatigue failure. Sattapan B. used Quantec Series 2000 Ni-Ti instruments, analyzing the appearance of fracture surface and found that the fracture patterns are 55.7 % in torsional fracture and 44.3 % in fatigue failure [9]. B. Peng and other scholars first used macro observation method to determine the failure mechanism of 122 Protaper S1 file, then, applied scanning electron microscope (SEM) to detect the fatigue striations. By macro observations, 25 files were belonged to flexural fatigue among 27 broken files. However, after SEM testing, only 18 files were found fatigue striations in the fracture surface. This implies that one may not know the correct failure mechanism only from macro observations, the SEM testing for identification is needed [10]. N. P. Kerezoudis*et al* gathered 46 Protaper endodontic files, which were after clinical applications, for failure identification. The files' models include Sx, S1, S2, F1, F2 and F3. It was found that only 5 files were fatigue failure among 34 samples, the rest were mostly broken due to single overloading [11]. Such different conclusions may deduce from not only dentists operation proficiency but also the root canal passage varies from person to person. Although the main failure mechanism of root canal files in clinical applications has not yet a conclusion, it is contemplated that if we can do some

special treatments to the files to improve its fatigue properties, the occurrence of unexpected fracture will decrease.

1.2.5 Fatigue properties of Ni-Ti rotary instruments

In material science, fatigue is the weakening of a material caused by repeatedly applied loads. It is the progressive and localized structural damage that occurs when a material is subjected to cyclic loading. The fundamentals of fatigue failure are based upon the incipient fatigue crack evolution process. Under cyclic loading, either pre-existing flaws (holes, keyways, sharp changes of direction etc.) or cracks initiated from a smooth surface at a highly stressed region slowly grow to a critical length and then propagate to a larger size that leads to the failure of the structures [3].

In general, fatigue fracture of Ni-Ti rotary instruments can be divided into three stages (see Fig.1-4.a for overall fracture surface SEM result):

i. Crack initiation and growth (The fatigue crack exhibited as a fan-shaped appearance as shown in Fig.1-4.b)

ii. Crack propagation

iii. Ultimate ductile fracture

The total fatigue life comes from the sum of both time in crack initiation and propagation. In fractography, scientists often observe and calculate the striation numbers in crack propagation region, since each striation represents one entire cyclic loading (Fig.1-4.c)[12].

Based on this common knowledge, a number of investigations on the fatigue properties of Ni-Ti alloys and components have been carried out by the material engineers [13][22] and the endodontics [23][36] communities. The former concentrated on understanding the microstructural mechanisms behind the fatigue failure and the factors that affects fatigue life. It has generally been concluded that the major factor that determines fatigue life is the applied strain amplitude. The relation can be expressed by Coffin-Manson formula shown as Equation (1.1).

$$\varepsilon_a N_f^{\beta} = \alpha \qquad (1.1)$$

Where, ε_a is the strain amplitude, N_f is the prediction of cycles to failure and the moduli α and β are considered as empirical material constants.

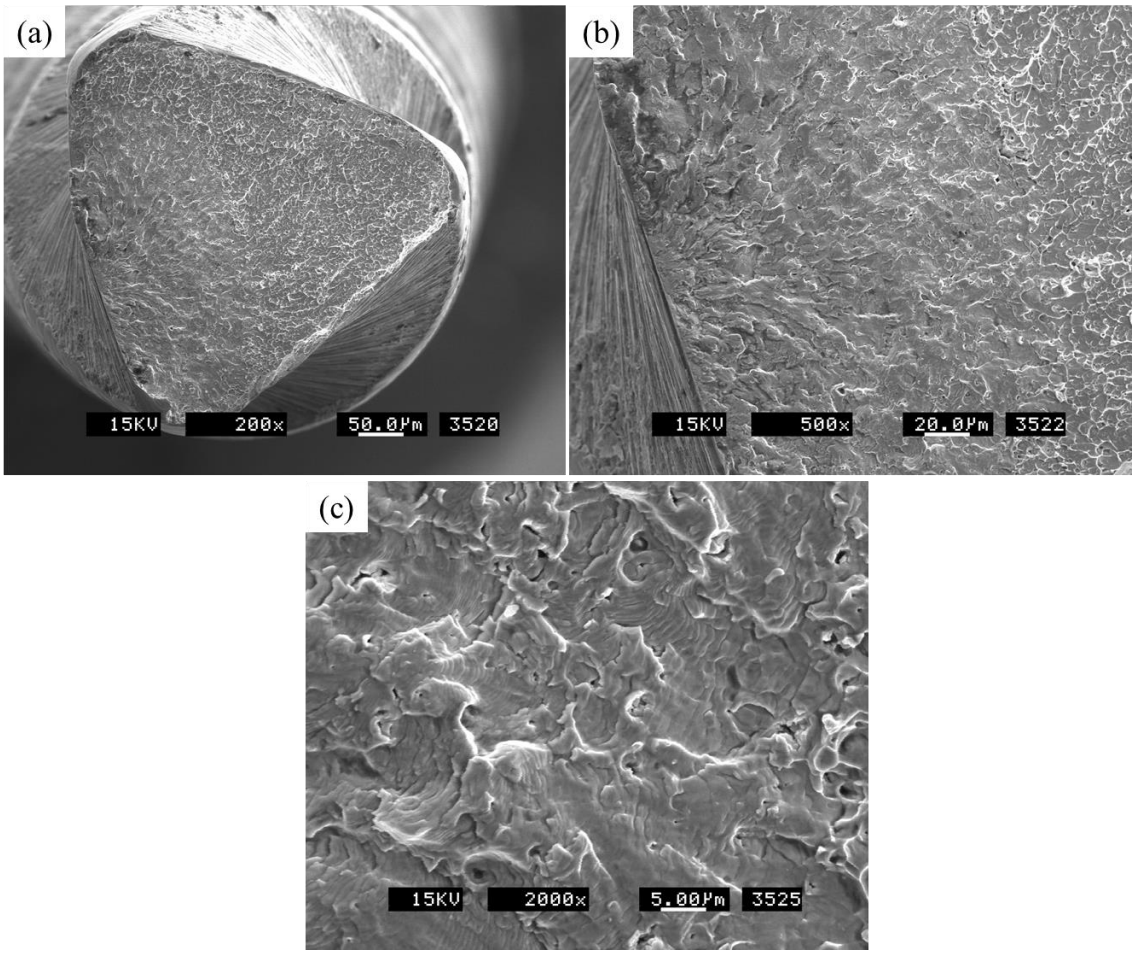

Fig.1-4. (a) SEM image of the fracture surface in ProTaper F2 Ni-Ti file. (b) SEM image of crack initiation region. (c) SEM image of striations in crack propagation region[12].

Fatigue life in air has also been found to decrease when the loading frequency is increased. The cause of this phenomenon has been attributed to the larger increase in temperature as the accumulation of hysteretic heat during a loading cycle is more serious under high loading frequency [14][17]. This frequency effect disappears when fatigue tests were carried out in constant temperature water [14][15] or oil [15][19] baths. Fatigue tests were originally done on bulk material such as bars and plates [37]-[38], but were recently focused on wires [13][22], presumably because Ni-Ti components in the forms of wire and tubing find wide medical applications. The wire diameter tested ranged from 0.75 to 2.16 mm, which were considerably larger than the critical sections used in endodontics applications. It has generally been established that a rotating bending testing technique is adequate for fatigue properties evaluation. This involves rotating a wire gripped at both ends and bent it into a semi-circular arc as shown in Fig.1-5. No additional loading is applied and the alternating strain is controlled by the radius of the semi-circular arc. Fatigue lives are normally correlated in terms of the alternating strain amplitude in a quantitative manner. On the other hand, although the works by the endodontics community were also carried out using rotating bending, they often concerns with the failure of the actual rotary instruments under a loading condition that closely mimics the service setting. The effects of rotating speed, high temperature sterilization, corrosive environment of sodium hypochlorite irritants, clinical uses and different instrument designs have been studied. Fatigue lives are correlated in terms of curvature radius and/or angle of bending. However, different workers quantified the degree of bending in different terms. Previously, for example, some researchers used the Schneider's

method [39], as shown in Fig.1-6, to quantify the severity of bending [e.g.31]] while the others used a radius of curvature together with an angle of curvature [e.g.24],27]]. The strains involved were normally not reported. This makes comparison on a common basis difficult and the results can only be viewed largely in a quantitative manner. Young & Van Vliet[40] tried to bridge this gap by testing Ni-Ti wires in a way closely simulated the endodontics operation yet correlated the fatigue life results in terms of alternating strain amplitude. The wire diameters employed were typical of the rotary instruments and a comprehensive number of parameters have been investigated systematically. They concluded that the fatigue life of Ni-Ti wire is a strong function of both strain amplitude and volume under strain, and a weaker function of loading frequency and the specific heat of the environmental medium. An equation relating fatigue life to the above α and β factors has been proposed as Equation (1.2), Equation (1.3)respectively.

$$\alpha = -0.76\ln[rpm] + 2.10\left[C_{p,e}/C_{p,NiTi}\right] \tag{1.2}$$

$$\beta = 0.10\left[C_{p,e}/C_{p,NiTi}\right]\ln[rpm] - 0.75 \tag{1.3}$$

Where rpm is the rotating speed, $C_{p,e}$ is the specific heat of environment and $C_{p,NiTi}$ is the specific heat of Ni-Ti wire. It has been suggested that the clinician can input the relevant parameters to obtain an estimate of possible lifetime of a rotary instrument. From Equation (1.1), (1.2) and (1.3), it can be interpreted as when N_f increases, the lifetime variability decrease with increasing $C_{p,e}/C_{p,NiTi}$. Physically, this means that the capacity for the surrounding fluid to absorb the heat generated by the cycling Ni-Ti wire correlates with increased lifetime.However, the experimental fatigue lives in this study are considerable higher than that those obtained by the material engineering and the endodontics research communities. Therefore, its use may lead to serious overestimation. Young & Van Vliet attributes this to a difference in chemical compositions, fabrication routes and a difference in testing technique that lead to different amounts of material volume under cyclic strain.

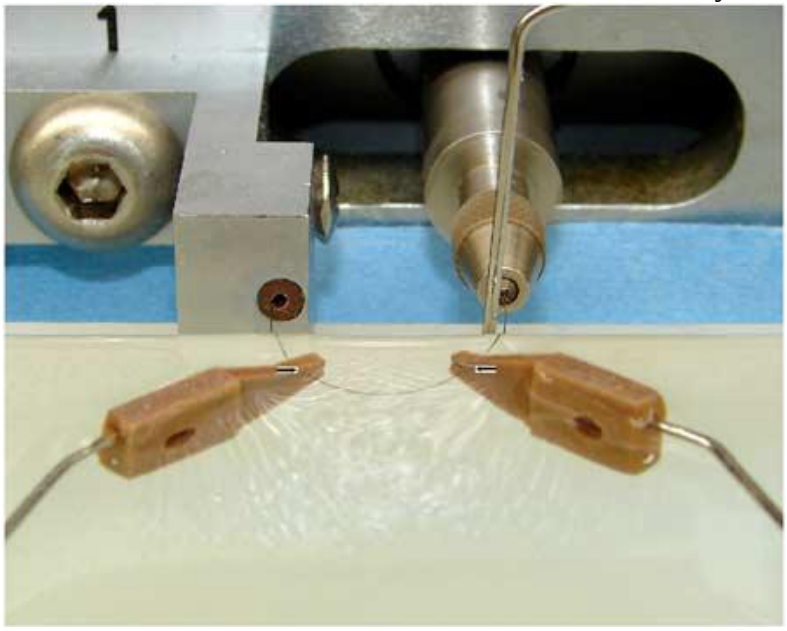

Fig.1-5.U-bend of Nitinol wire mounted within rotary chuck and bushing [22].

Fig.1-6.Schneider's method for characterizing file severity by Schneider's angle α [39].

1.3 Introduction of Two-Photon Polymerization

Two-Photon Polymerization (TPP) is a practical method for fabricating three-dimensional micro-scale complicated structure which is initiated by two-photon absorption (TPA)[41[44]. TPA is a nonlinear optical phenomenon and the absorption of the two-photons is often explained by a three-state model as seen in Fig.1-7. As the absorbing species interacts with the first photon, a virtual intermediate state is created. The second photon is available only when it arrives within the lifetime of the virtual state, i.e. typically about 10^{-9} to 10^{-12} second [44]. Hence more intense energy is required for TPA. The energy of the incident photon is given by $h\nu$, where h is the Planck's constant which is 6.626×10^{-34} J·s divided by 2π, and ν is the frequency of the incident light. The absorbing species is raised to an excited state after absorbing the energy of two photons, which is equal to S_1-S_0, where S_0 is the energy level at the ground state and S_1 is the energy level at the excited state.

In general, this process has inverse dependence on the laser intensity.Therefore, it has high spatial selectivity. Furthermore, since TPA is only possible if a molecule receives two photons in a very short period, a femtosecond laser is needed.However, thedelivery of the second photon can also be accomplished by micro-chip pulsed lasers with a high peak power and a narrow pulse width of a nanosecond scale [42]. Two-photon phenomenon have been studied with both nanosecond and femtosecond lasers. The easy availability of micro-chip pulsed lasers has led to their widespread use for studying nonlinear optical phenomena like TPA. Although femtosecond lasers have an ultra-narrow pulse width of femtosecond scales, femtosecond lasers are still very expensive to be used for many applications in terms of cost, running cost and energy expenditure. An easy alternative is the use of micro-chip lasers [41][43].

The polymerization caused by TPA is called photopolymerization. Photopolymerization is defined as a polymerization process requires to absorbing energy from photons. As a laser beam is focused by a microscopic objective lens (see Fig.1-8.a), the density of photons decreases with the distance away from the focal plane, but the total number of photons in each cross section of the laser beam remains the same, as shown in Fig.1-8.b. Thereafter, the resin is solidified completely in the illuminated region even beyond focal point, leading to a poor resolution. This means that the linear response of the materials to the light intensity based on single photon absorption does not have optical sectioning capability. However, if material response is proportional to the square of the photon intensity, the integrated material response is enhanced greatly at the focal point (see Fig.1-8.c) and therefore the two-photon absorption-based polymerization occurs only in a small volume within the focal depth.

A two-photon polymerizable medium would contain a photo-sensitizer/initiator that is capable of absorbing two photons in the working wavelength range to give raise to a reactive species. There are generally two types of initiating species namely a radical initiator which is used in the case of free radical polymerization of the photo-patternable media like acrylate derivatives; or a photo acid generator in the case of cationic polymerizations for epoxy resins.

Three steps of initiation, propagation, and termination are usually applied to explain the TPP chain reaction. The photochemical reaction in the case of a radical initiated TPP can express as:

$$\begin{aligned} A &\xrightarrow{2h\nu} 2R^{\bullet} \\ R^{\bullet} + M &\longrightarrow R - M^{\bullet} \end{aligned} \tag{1.4}$$

Here A is a photo-initiator, $R^{\bullet}$ is an initiating radical species, M is a monomer, and $R-M^{\bullet}$ is a growing polymer chain with radical end. The photo-initiator receives energy through TPA and becomes radical species. Then the initiating radical species will start the polymerization reaction by reacting with a monomer to form a growing polymer chain with radical end. Since the growing polymer chain has a radical end, it is going to capture more monomers and become longer. Such propagation process can be expressed as:

$$\begin{aligned} R-M^{\bullet} + M &\longrightarrow R-M_2^{\bullet} \\ R-M_n^{\bullet} + M &\longrightarrow R-M_{n+1}^{\bullet} \end{aligned} \tag{1.5}$$

The reaction proceeds at the end of the reaction either due to unavailability of energy/monomers, or due to the remaining species chemically combined to terminate the reaction. The termination process can be expressed as:

$$R-M_n^{\bullet} + R-M_m^{\bullet} \longrightarrow R-M_{m+n}-R \tag{1.6}$$

A wide range of materials, like photo-polymerizable resins, ceramic precursors as well as dispersed metal solution have been used as raw materials for creating microstructure with TPP [45][51].

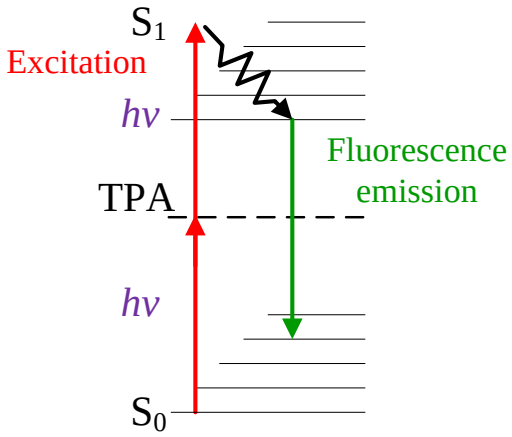

Fig.1-7.Three-state energy model diagram for TPA [41].

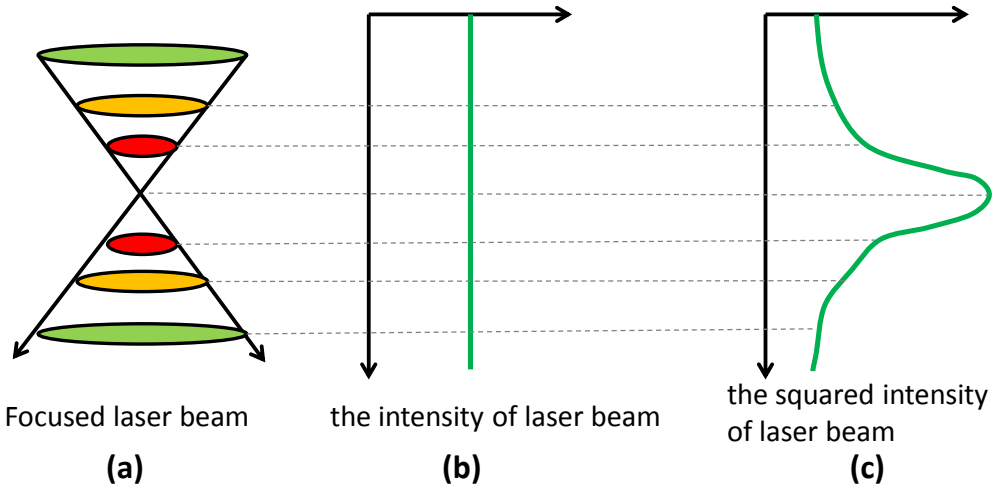

Fig.1-8. Single/two-photon absorption generated by a focused beam: (a). schematic diagram of a focused beam, (b). total energy calculated with single-photon absorption, (c). total energy calculated with two-photon absorption.

1.4 Resolution of two-photon polymerization

TPP is a well-known approach to produce micro objects with complex three-dimensional shapes, and is widely applied in optical devices, for example optical gratings. The products are the combination of all polymerized voxels, the basic TPP element [52]. Voxel features were considered as the main factor to control the surface quality of micro objects, so that the sizes of TPP voxels have been studied. Voxel features include lateral size, axial size, and aspect ratio. The aspect ratio, a ratio of the axial size and the lateral size, is an important feature for 3D precise fabrication with TPP. To minimize the aspect ratio of voxels, a method of minimum power and minimum exposure time (MPMT) has been proposed [52][53]. The concept of MPMT is that the voxel size can be reduced by decreasing the laser power and shortening the exposure time. The MPMT scheme is shown inFig.1-9Kueble*et al.* have reported the minimum size of their fabricated voxels is 200 nm in lateral and 700 nm in axial in 2001 [54]. Tanada*et al.* have improved the lateral size of voxels to 120/100 nm[55].See*et al.* have derived a direct-laser-writing mechanism to describe the relationship among the feature size and fabricating parameter[56]. They defined a threshold condition for line fabrications, and the condition is based on the single voxel fabrication.

In addition, heat is also an important issue for the fabrication with a high resolution[57]. When the temperature is rising, the molecules will diffuse more quickly than that in a normal temperature. Numerical models including temperature, diffusion, and concentrations of molecules is useful to study the effects[58[60].

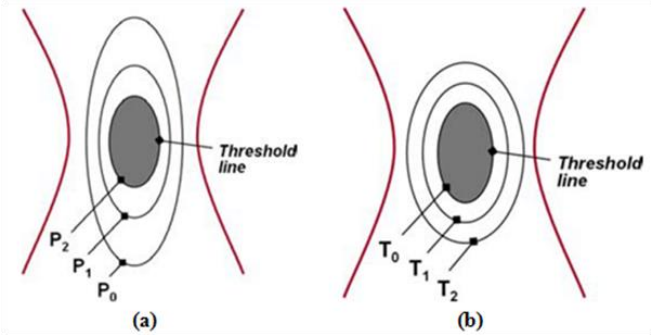

Fig.1-9.Schematic illustration of voxel size reduction with the decrease of (a).laser power and (b). exposure time [54].

1.5 Applications in Bio-compatible large structure using Two-Photon Polymerization

As the mentions earlier, it is beyond all doubt that the TPP provides a powerful approach to fabricate fully 3-D sub-micron or nano-structures for various applications, but recently, with the advance of TPP technology, the feasibility of TPP manufacturing in some large millimeter scale bio-compatible structures had been explored. For example, Heler*et al*. fabricated millimeter scale scaffold which can be used in tissue engineering as shown in Fig.1-10[68].Pauliu*set al*. manufactured $9 \times 9 \times 2$ mm^3 disc-shaped scaffold for cell culture (Fig.1-11.a-b) and $9 \times 3 \times 0.5$ mm^3 artificial blood vessel prosthesis stent (Fig.1-11.c), which can be made up to 50 % in porosity (Fig.1-11.d) [69]. Unlike previous studiesoften applied piezo-driven stages to get great resolution, Pauliusused linear motor driven X-Y stages to get larger working distance in X/Y axes so that not only the fabrication time can be saved but also the larger structures can be made. Their fabrication steps and optical system are shown as Fig.1-12.a and Fig.1-12.b respectively.

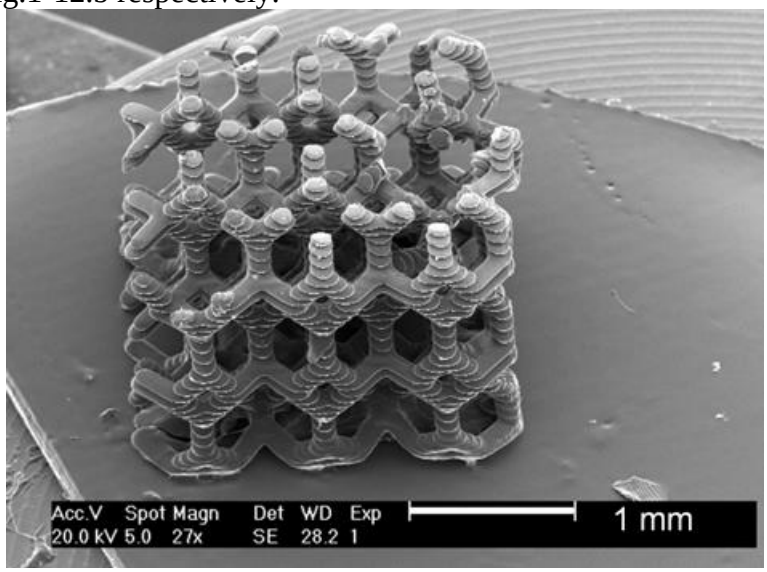

Fig.1-10.SEM image of scaffold [68].

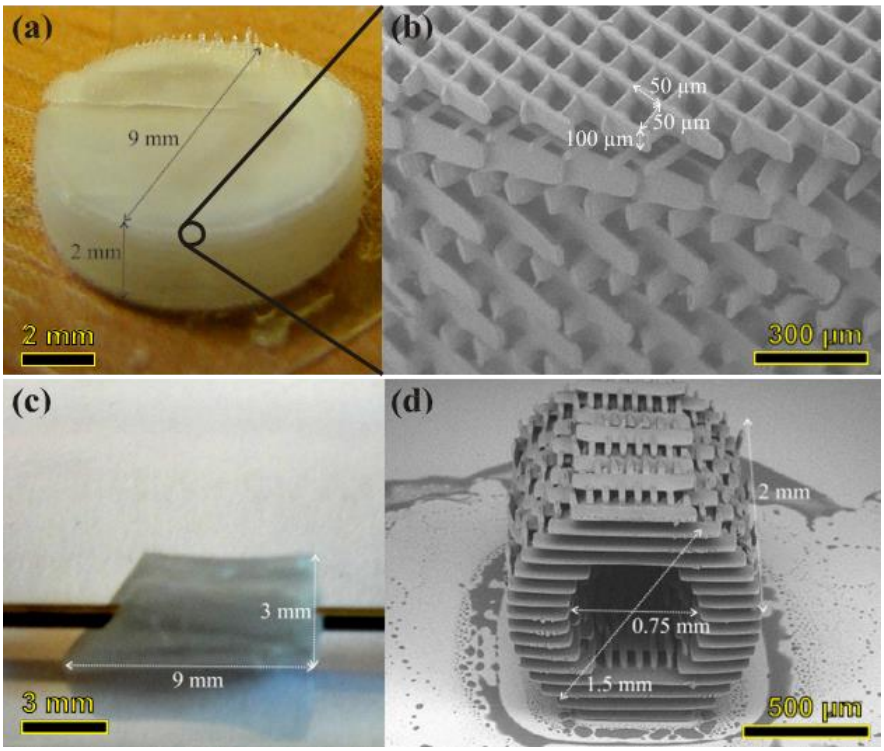

Fig.1-11. (a) A photo of $9\times9\times2mm^3$ disc shape scaffold out of SZ2080 polymer; (b) Inset shows SEM image of internal structure of the disc shape scaffold. The pore size is $50\times50\times100\mu m^3$,and the general porosity is 60%. 5 mm/s sample translation velocity and 10×0.3NA objective were used; (c) An artificial blood vessel scaffold out of Ormoclear polymer with outer diameter of 3 mm; (d) SEM image of artificial blood vessel scaffold with outer diameter 1.5mm and internal diameter 0.75mm[69]

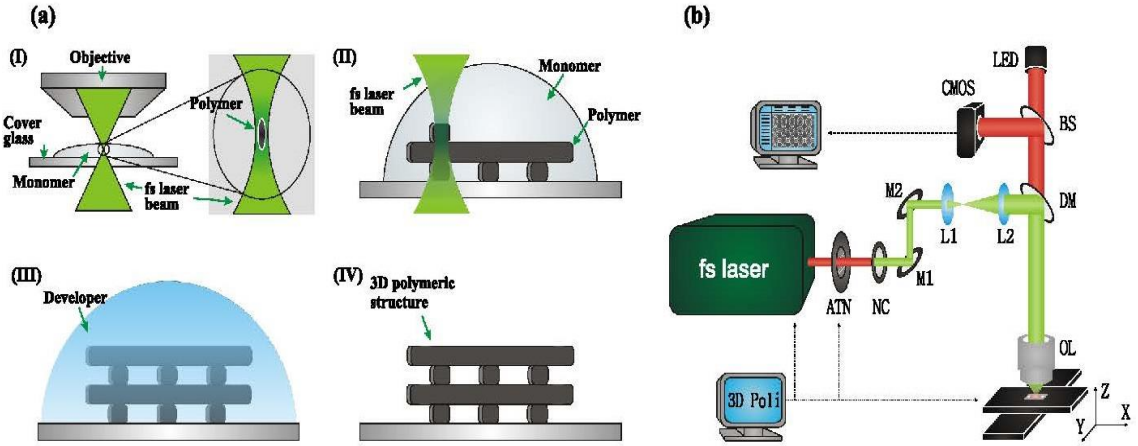

Fig.1-12. (a) Fabrication steps: (I) photopolymerization process initiation, (II) structure is directly written by moving the sample in regard to the focal spot, (III) organic developer

washes unexposed material, (IV) 3D free-standing scaffold is obtained; (b) DLW fabrication setup: ATN-attenuator, NC-second harmonic non-linear crystal, M1-M2-mirrors, L1-L2-telescope, DM-dichroic mirror, OL-objective lens, BS-beam splitter, CMOS-camera [69].

1.6 Motivation

A recent survey of clinical fracture cases showed that the major causes of rotary instrument fracture are torsional overload and cyclic fatigue. With better training and torque control driving unit, the problem of torsional overload should be alleviated to a large extent. However, there is no effective solution to the cyclic fatigue fracture in sight. The method of testing for cyclic fatigue properties of rotary instruments and the parameters to accurately quantify such properties has not yet been standardized. Different testing and interpretation methods add to our phenomenological knowledge of the issue but not the quantitative assessment and prediction. A more rigorous quantification of fatigue damage has been established in the current work. With this tool we can compare fatigue properties such as fatigue life and cutting efficiency on a common basis.

In order to achieve our goals, which is not only to propose a good strategy to extend fatigue lives but also to hold the cutting efficiency, series of test under different heat treatments should be investigated.Furthermore, it is reasoned that when a crack develops in the instrument, its compliance and natural vibration frequency will change. In fact, during cyclic fatigue testing, peculiar sounds that are markedly different from those under normal operation did arise just prior to instrument fracture. This phenomenon inspired us to develop a mean to capture the strain waves using FBG sensors and to try to analyze for the characteristic wave properties accompanying the development of a crack.

We also want to take the positive driving preventive measure, investigating the feasibility of manufacturing new type of rotary needles. The material candidate is polymer, which gives us the chance to put reinforcing fibers or powders inside the needle before fabrication. Although the fatigue problem still exists in polymer, it is reasoned if we use abrasive powder and polymer which are biocompatible so that even the needle is broken inside the root canal, the material can biodegrade on its own. SinceTPP technology has been recognized as the powerful fabrication of complex 3-D micro/nano structures in polymer, it is better for us to apply this technology to have a prototype first. Unlike previous micro-scale applications in TPP, our case is in millimeter scale. In order to fabricate such a big object, self-Q-switched microchip Nd:YAG laser with high power and repetition rate is required. Moreover, accurate control of power/focal point to keep the product resolution and fast fabrication is our goal. Not only needles but also other large structures will then be discussed.

It is hoped that with all these information, the fatigue lives of rotary instruments can be predicted and closely monitored to avoid/alleviate the occurrence of unexpected fracture or even get completely avoidedby applying new type of needles.

1.7 Thesis Outline

This thesis focuses on two parts: fatigue prevention/monitoring system in clinical therapy and large/quick fabrication in TPP manufacturing. The following chapter will present the subjects in this thesis. Before the discussion of the subjects, the basic principle of fatigue, FBG sensors and TPP will be introduced in Chapter 2, such as fracture mechanism, optical system and chemical reaction model. Then the development of fatigue/cutting efficiency

testing machine, FBG based monitoring system and TPP setup in order to achieve large and fast manufacturing will be demonstrated in Chapter 3. A LabView program for analyzing captured data from FBG sensors as well as its background related knowledge is also presented. Chapter 4 will discuss the characteristics and results of fatigue, cutting efficiency properties and the FBG monitoring system. An optimized strategy of the combination in heat treatment in order to get the best performance of Ni-Ti rotary instruments and a reliable warning systemare proposed to solve current clinical issues.Chapter 5 will study the characteristics of large and fast TPP fabrication. The cm-size needle, mm-size scaffold and massive laser beam parallel fabrication achieved by phase mask are proposed to show the potential of TPP manufacturing in the future. The conclusions and recommendations for future work are presented in Chapter 6.

Chapter 2 Principles

This chapter introduces the basic knowledge of the thesis, including fracture mechanism, FBG sensors, optics and chemical model. The concepts, theories, methods, and mathematic models will be applied to develop the works in this thesis.

2.1 Fatigue life prediction

The basic mechanism of fatigue had been introduced in Chapter 1. Here we mainly focus on the mechanics of fatigue and the prediction of fatigue life.

There are three commonly recognized forms of fatigue: high cycle fatigue (HCF), low cycle fatigue (LCF) and thermal mechanical fatigue (TMF). The principle distinction between HCF and LCF is the region of the stress strain curve where the repetitive application of load (and resultant deformation or strain) is taking place.

It has been found that Ni-Ti rotary instrument belongs to LCF,which can be characterized by high amplitude low frequency plastic strains.The more recent approach is based on local strain, referred to as the strain-life (ε - N) method. This approach relates the reversals to failure $2N_f$ and to the strain amplitude $\frac{\Delta\varepsilon}{2}$ .The relationship is as follows:

$$\frac{\Delta\varepsilon}{2}=\frac{\Delta\varepsilon_e}{2}+\frac{\Delta\varepsilon_p}{2}=\frac{\sigma'_f}{E}(2\mathrm{N}_f)^b+\varepsilon'_f(2N_f)^c \tag{1.7}$$

where $\frac{\Delta\varepsilon}{2}$, $\frac{\Delta\varepsilon_e}{2}$ and $\frac{\Delta\varepsilon_p}{2}$ are the total, elastic, and plastic strain amplitudes respectively. In this equation, the two additional fatigue properties needed are the fatigue ductility coefficient ε'_f and the fatigue ductility exponent c . The strain-based approach considers the plastic deformation that often occurs in localized regions where cracks nucleate. Also, the strain-based approach may be regarded as a comprehensive approach describing both elastic and inelastic cyclic behavior of a material [70].

2.2 Principles of optic fiber grating sensors

2.2.1 Basic parameters of optical fibers

i. Numerical aperture (NA):

By definition, the numerical aperture is equal to the sine of one half the acceptance angle of a fiber optic. The incident angle should confirm to a boundary condition which is[71]:

$$\sin\theta_i \le NA=(n_{core}{}^2-n_{clad}{}^2)^{1/2} \tag{1.8}$$

where NA is the numerical aperture, θ_i is incident angle. Fig.2-1 explains the concept of acceptance cone in relation to θ_i . Light entering the core from within this cone will be propagated by total internal reflection. Light entering from outside the cone will not be propagated. Thus a large NA makes it easier to inject more light into a fiber, while a small NA tends to give the fibber a higher bandwidth.

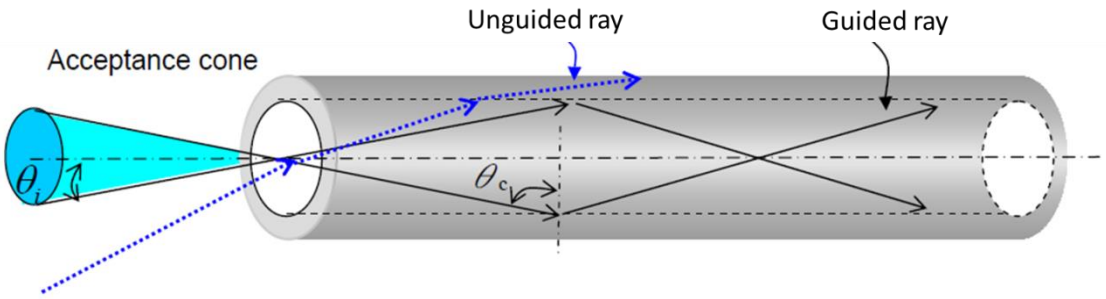

Fig.2-1. Scheme of the opto-guide in the optical fiber: the opto-guide is transmitted within the fiber core due to total reflections. θ_i is the incident angle and θ_c is the critical value of the reflection angle [71].

ii. Mode propagation constant (β):

Mode propagation constant β, according to the electromagnetic wave theory, each different mode has a different light propagation velocity. We can define the mode propagation constant β as [71]:

$$\beta = \frac{2\pi}{\lambda} n_{eff} \tag{1.9}$$

where n_{eff} is the effective refractive index of the optical fiber, λ is light wavelength. In the case of Fig.2-1, the mode propagation constant can be written as $\beta = \frac{2\pi}{\lambda} n_{core} \sin\theta_i$.

2.2.2 Theory of FBG

Fiber Bragg grating (FBG) consist of a section of periodic variation in reflective index in the optical fiber core. When a broadband light spectrum encounters the Bragg gratings, a narrow band spectrum at the Bragg wavelength λ_B will be reflected. This phenomenon was based on the grating diffraction principle [72]. Fig.2-2 explains the optical grating principle schematically. The guide modes relation is as follows:

$$\beta_2 = \beta_1 - \frac{2\pi}{\Lambda} \tag{1.10}$$

where β_1 is the undistributed mode propagation constant. $\beta_2 < 0$ describes modes that propagate in the $-z$ direction. Where Λ is the grating pitch or the periodicity of the grating, and n is the effective index of the fiber core. A typical FBG has a very short period Λ in the order 1 μm with a total grating length of about 1~2 cm.

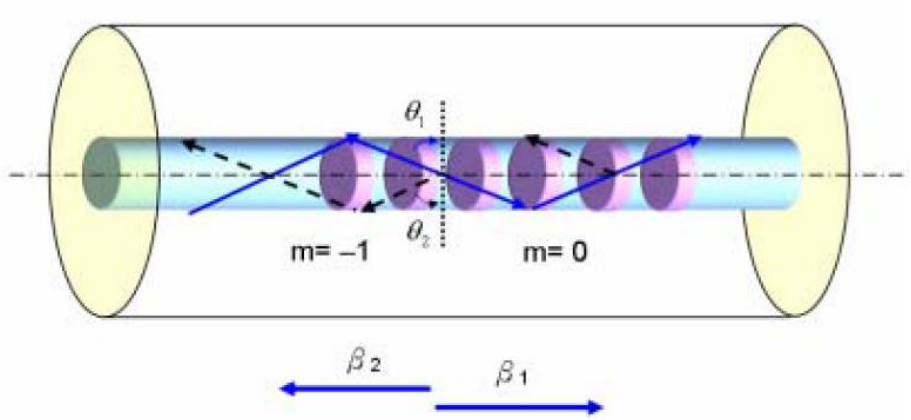

Fig.2-2.Scheme to explain the principle of single-mode fiber grating.

By using equation (1.9)and (1.10), the resonant wavelength for reflection of a mode of index $n_{eff,1}$ into the other mode of index $n_{eff,2}$ can be found as $\lambda_B = (n_{eff,1} + n_{eff,2})\Lambda$. For a single-mode fiber, the two modes are identical so that the result for Bragg reflection is obtained:

$$\lambda_B = 2n_{eff}\Lambda \qquad (1.11)$$

2.2.3 Optic fiber grating sensors interrogation system

To use an FBG as a sensor, it is illuminated by a light source with a broad spectrum and the reflected wavelength is measured and related to the local measurands of interest. Shifts in the Bragg wavelength can be monitored by the following techniques:

- An interferometer may be used to convert wavelength light into phase shifts, which can be detected by measuring variations in the light intensity as the path difference in the interferometer is varied. In application use, this method is considered relatively expensive and prone to environmental interference.
- A sloped optical filter, which may be another Bragg grating, can be used to convert wavelength shifts directly into wavelength changes. If the filter is designed to have a known pass/reject ratio which varies with wavelength, then the wavelength of a narrowband reflection from a single grating can be determined simply by measuring and comparing the passed and rejected intensities. For the filter with a transmission spectrum shown in Fig.2-3, as the Bragg wavelength increases from λ_1 to λ_2, the transmitted intensity it decreases and the reflected or rejected intensity will increases correspondingly. The advantage of this way is one can get high sensitivity of the signal while the disadvantage is it can address only one grating at a time.

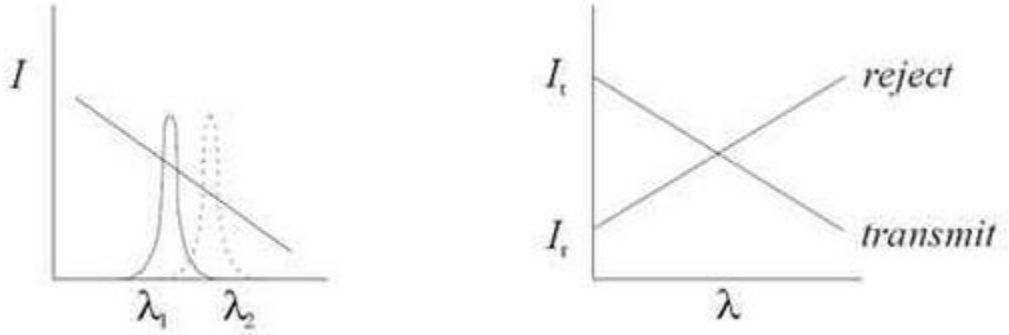

Fig.2-3.Demodulating FBG with a passive filter. Wavelength shifts (left) are converted into intensity changes (right).

Today, the most popular interrogation schemes are based on intensity modulation. It is usually consist of an optical tunable edge filter called OTF used to modulate the intensity of reflective light from an FBG; therefore, the power of the output light from the edge filter will change as FBG wavelength shifts. In the current work, since the signal-to-noise ratios of the data we captured is too small to allow a clear definition of the stress wave from the rotating Ni-Ti rotary instruments, it is better for us to applyanother FBG as a sharp tunable edge filter to create steep slope in experiments. The related system setup will then be introduced in Chapter 3.

2.3 Optics of two-photon polymerization

In this section, fundamental theory and fabrication process of TPP will briefly introduced.

2.3.1 Fundamental theory of TPP process

As mentioned in 1.3, the voxel size, which is recognized as the basic element of TPP, is significant for deciding different manufacturing accuracy. Such resolution is governed by optical properties of objective lens, laser wavelength, intensity applied and exposure time. To have a better idea of voxel size in TPP process, we need to start from the laser beam simply assumed as a Gaussian beam, whose electric field and intensity distribution are well approximated by Gaussian function.

Recall from Fig.1-8, the distribution I of the photon flux intensity of the laser with a cylindrical coordinate system under perfect Gaussian beam approach can be defined by:

$$I(r,z) = I_0 \frac{{\omega_0}^2}{\left(\omega_z(z)\right)^2} \exp\left[-2\left(\frac{r}{\omega_z(z)}\right)^2\right] \qquad (1.12)$$

where ω_0 is the beam waist in the focal plane, and $\omega_z(z)$ is the beam radius along the laser propagating direction. Such relationship among the beam profile and the parameters is shown as Fig.2-4.

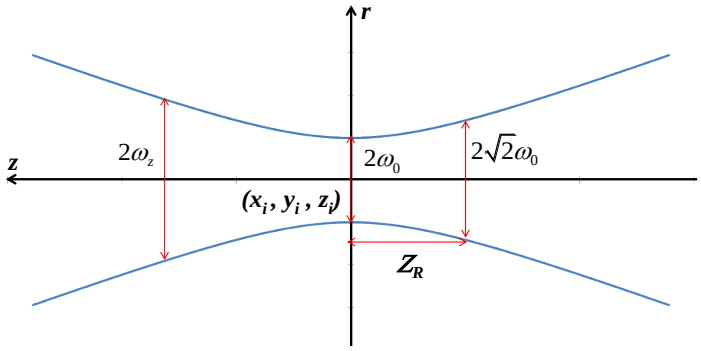

Fig.2-4.Propagation profile of Gaussian beam and its characteristic parameters in a cylindrical system.

Full width half maximum (FWHM) is the common factor to describe the size of the Gaussian distribution, and is the distance where the intensity is half of the peak value. Laser waist ω_0 is another conventional factor, and is defined by the minimum beam radius where the intensity decreases to $1/e^2$ (=13.5%). In general, a laser waist of a Gaussian beam can be computed by [76]:

$$\omega_0 = \frac{0.61\lambda}{NA} \tag{1.13}$$

where λ is the light wavelength in a vacuum. In addition to Equation (1.13), there have been several equations to evaluate laser waist [76],63]. The beam radius ω_z along the propagation direction is expressed as:

$$\omega_z(z) = \omega_0\sqrt{1+\left(\frac{z}{z_R}\right)^2} \tag{1.14}$$

where Z_R is the Rayleigh length, and is typically defined by $\omega_z(Z_R) = \sqrt{2}\omega_0$.

To predict voxel size on the vocal point, we need the distribution I of the photon intensity of the laser at $z = 0$, that is:

$$I(r,0) = I_0 e^{\frac{-2r^2}{\omega_0^2}} \tag{1.15}$$

where I_0 is the maximum intensity per unit area. A voxel produced by TPP is shown inFig.2-5[77].

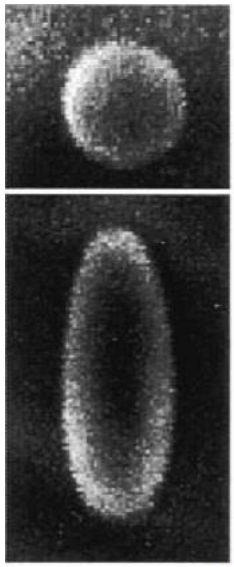

(a) Top-view and side-view of a voxel

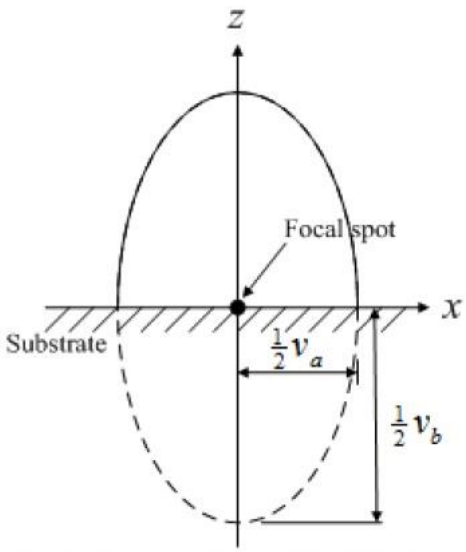

(b) A spinning ellipsoid simulating a voxel

Fig.2-5. A voxel produced by TPP [77].

The voxel width v_a and voxel height v_b can be predicted by finding the region above the threshold intensity, that is $I(\mathrm{R},0)^2 = {I_{th}}^2$, where ${I_{th}}^2$ is the threshold energy intensity of the resin. Therefore, the width and height can then be obtained from the square of Equation (1.15):

$$v_a = \omega_{xy}\sqrt{\ln\left(\frac{I_0}{I_{th}}\right)^2} \tag{1.16}$$

$$v_b = \omega_z\sqrt{\ln\left(\frac{I_0}{I_{th}}\right)^2} \tag{1.17}$$

From above introduction, we can see that the voxel size is influenced by the exposure time, intensity of laser, beam waist and the threshold energy governed by the material of resin. Since the roughness and resolution of microstructure is affected by the size and aspect ratio of the voxel. For different products, the required manufacturing quality and acceptable fabrication time are two major and interdependent factors for considering the fabrication process which are decided by voxel dimension and the exposed distance between voxels.

2.3.2 The optical setup of TPP fabrication system

A traditional TPP optical system is shown in Fig.2-6, and comprises a microscopy, a laser source, an acousto-optic modulator (AOM), several lenses, and some reflecting mirrors. The laser source in this study is Q-switch pulsed and frequency-doubled Nd:YAG laser (130kHz, 532nm). Therefore, the laser source is able to emit a beam with a specific wavelength, a high repetition rate, and a narrow width of the pulse duration. The operation of the AOM is similar to a shutter, which is able to allow the propagation of the laser beam for a given period, also known as exposure time. After passing the AOM, the width of the beam is enlarged and controlled by several lenses before the beam enters the objective lens inside the microscopy. The purpose of some mirrors is to produce a uniform beam through decreasing the dimension of the optical system.

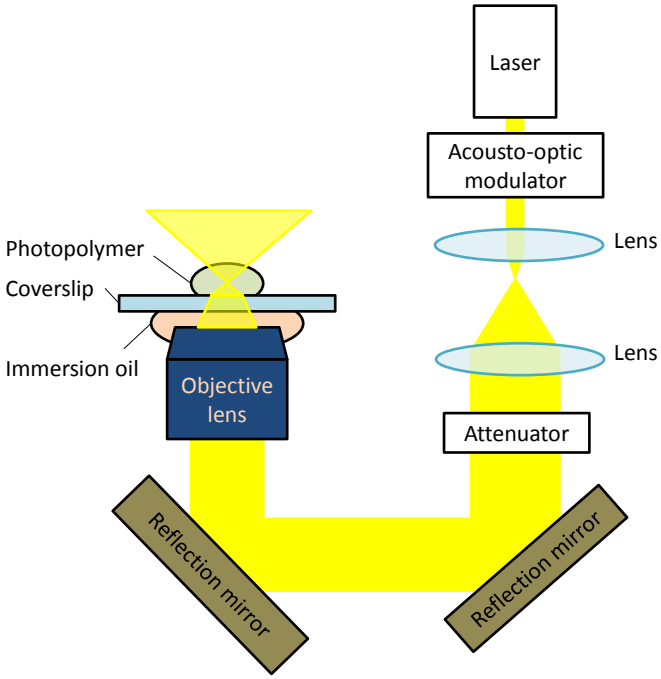

Fig.2-6.Schematic diagram of TPP optical system [78].

The reason of enlarging the beam width is to generate a high intensity at the focal point. The spot size of the focused beam depends on the working numerical aperture (NA) of the objective lens. The numerical aperture can be defined by:

$$NA = n\sin\theta \tag{1.18}$$

where θ is the half-angle of the beam divergence, and n is the refractive index of the medium. Using a lens with large NA can generally produce a large half-angle and induce a high intensity. However, if the beam width is smaller than the radius of the lens, the working NA of the lens will not be the maximum value and the intensity at the focal point will be low. In order to achieve a good focusing ability, the width of the incident beam to the lens must be enlarged. Furthermore, Equation (1.18) is under a hypothesis that the incident beam should be a collimating and uniform beam [79]. Since most beams have Gaussian-like profiles, the intensity around the propagating axis of the incident beam is almost uniform. As the width of the incident beam is large enough, the aperture of the objective lens will block the non-uniform part so that the entering beam can be regarded as a collimated beam. Such mechanism is shown in Fig.2-7. After passing the objective lens, the focused beam goes through immersion oil between the objective lens and a glass coverslip, and then enters the photopolymer. Because the refractive index of the air is 1.0, the NA of the lens cannot be larger than 0.95 when the focused beam goes into air directly [80], therefore, an oil medium with high refractive index should be applied between coverslip and objective in order to get large working NA of the objectives.

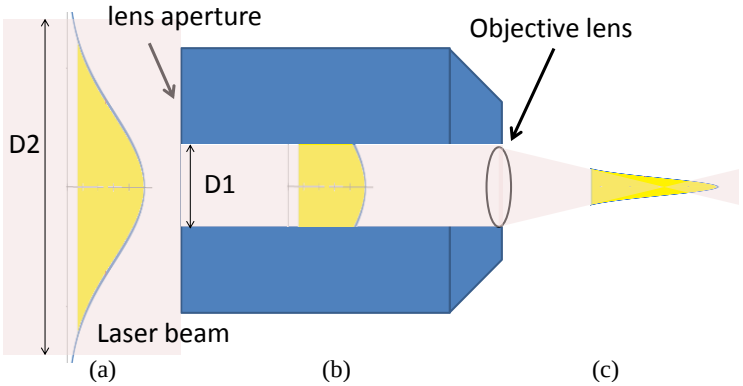

Fig.2-7. Propagation of a laser beam passing through an objective lens: (a) enlarged and collimated beam whose intensity is a Gaussian distribution; (b) uniform beam cut by the lens aperture; (c) focused beam with a high peak intensity [78].

2.3.3 Diffractive optical elements

The diffractive optical elements (DOEs) also known as diffractive beam splitter is a single element that divides an input beams into N output beams. Each output beam retains the same optical characteristics as the input beam, such as size, polarization and phase. The principle of this operation is based on the wave nature of the light. Designing the diffractive pattern for a beam splitter follows the same principle as a diffraction grating, with a repetitive pattern etched on the surface of a substrate. The depth of the etching pattern is roughly on the order of the wavelength of light in the application, with an adjustment factor related to the substrate's index of refraction.

The etching pattern is composed of periods, which is identical sub-pattern units that repeat cyclically. The width d of the period is related to the separation angle θ between output beams according to the grating equation:

$$d \sin \theta_m = m\lambda \tag{1.19}$$

Here, m represents the order of the diffractive beam, with the zero order output simply being the undiffracted continuation of the input beam. While the grating equation determines the direction of the output beams, it does not determine the distribution of light intensity among those beams. The power distribution is defined by the etching profile within the unit period, which can involve many etching transitions of varying duty cycles. Although, a number of strategies into various aspects of same intensity distribution exist, no perfect way can be drawn up to prevent the high intensity accumulated in the central, which is known as zero order effect. Such phenomenon will be discussed in the later chapter.

Chapter 3 Experimental setup

3.1 Fatigue testing of Ni-Ti rotary instruments

Cyclic fatigue testing in artificial canals was carried out by ProTaper F2 (DentsplyMaillefer, Ballaigues, Switzerland) with an effective length of 21mm.In order to simulate the situation of Ni-Ti rotary instruments curved in the root canal, the Pruett curvature definition has been applied. The experiment was done by 400 rpm in rotational speed. Base on this definition, we developed a fatigue testing machine as shown in Fig.3-1. In this study, four different combination of curvature radius (R) and curvature angle (A) had been applied to simulate the severity of curvature in root canal. Four combinations of R and A had been applied in this study: R7.5A40, R10A60, R7.5A60 and R5A60. Previous studies showed that the canal opening width (W) has great impact on strain [81]. Therefore, in this study, we strictly controlled the width (W) as the diameter of rotary instruments when it enters the canal. In other words, it makes the center of outer arc and the center of inner cylinder located on the same line, and the distance between centers is same as the opening width (see Fig.3-2).

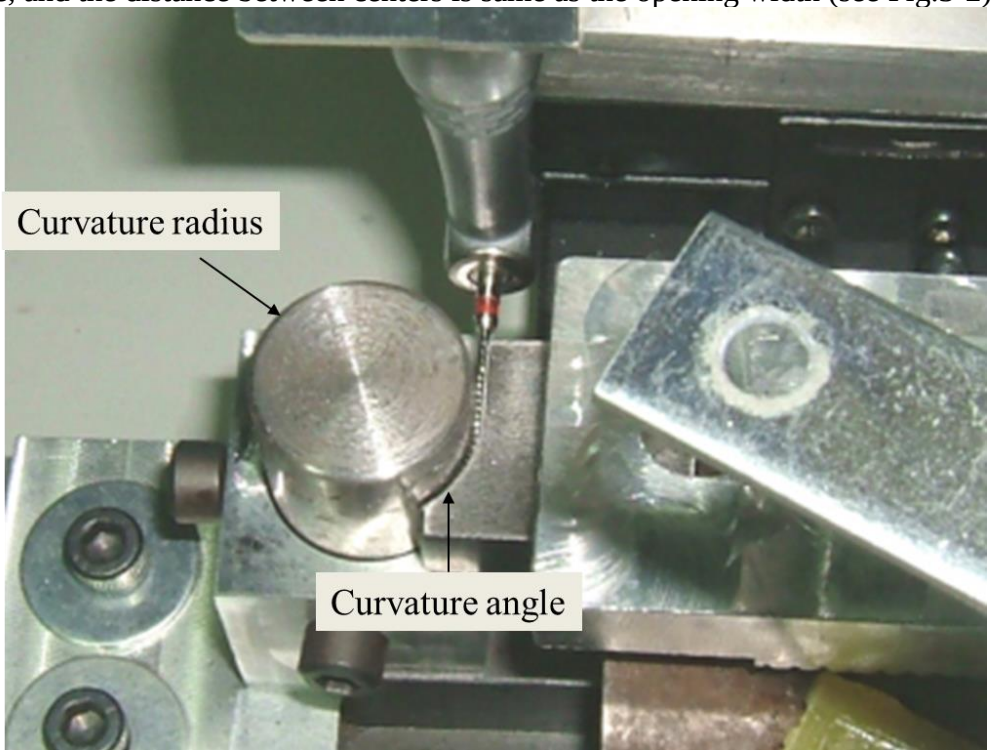

Fig.3-1.Fatigue testing machine.

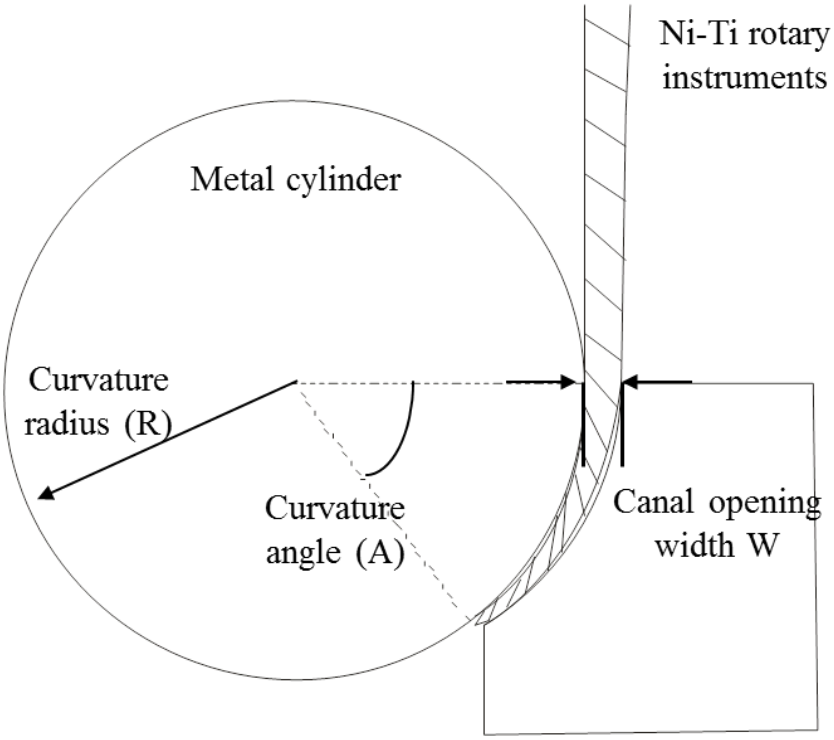

Fig.3-2.Schematic view of root canal simulation [81].

As mentioned in Chapter 1, Ni-Ti rotary instrument belongs to LCF. Traditionally, for a LCF issue, strain is often used as an indicator than stress. Although there will be no permanent deformation when the strain of the file is under 8%, there still exists the phenomenon that the strain increases however the stress is almost the same in the phase transition region between 2.8% to 5.6%[82]. If fatigue failure occurred in this strain region, stress-based approach cannot reflect the true severity of curvature. Another reason for applying the strain as an indicator is that we are testing fatigue properties by bending rather than by controlling the loads applied to the endodontic file.

3.2 Cutting efficiency evaluation

3.2.1 Cutting machine

The cutting efficiency evaluation was carried out by ProTaper F2 (DentsplyMaillefer, Ballaigues, Switzerland) with an effective length of 21mm. The main purpose of root canal therapy is to remove the diseased tissue or nerves from the canal by cutting [83]. Compared with the traditional stainless steel endodontic file, Ni-Ti files cutting efficiency is relatively low due to its low hardness [84]. As a result, several studies by various processes to improve the surface hardness had been proposed, such as surface nitriding[85], electrolytic polishing [86] and physical vapor deposition [87]. The testing machine we used is shown as Fig.3-3 to Fig.3-4. It composed of handpiece, X-Y stage, rotation stage, washer and applied force mechanism. The applied force mechanism is shown as Fig.3-4, which is made up of metal sliding block, screw and spring. The spring length is 35mm and its spring constant is 1N/mm. A M5 screw in 45mm length is threaded through the spring, supporting the spring to against bending when compression force applied. Furthermore, to prevent the file with the phenomenon of sliding up and down in the cutting process, a width of 2mm dent as shown in Fig.3-5 had been machined on the surface of sliding block to ensure the rotation of file is stable. By replacing the washer to adjust the length of compressed spring, the applied force can be determined.

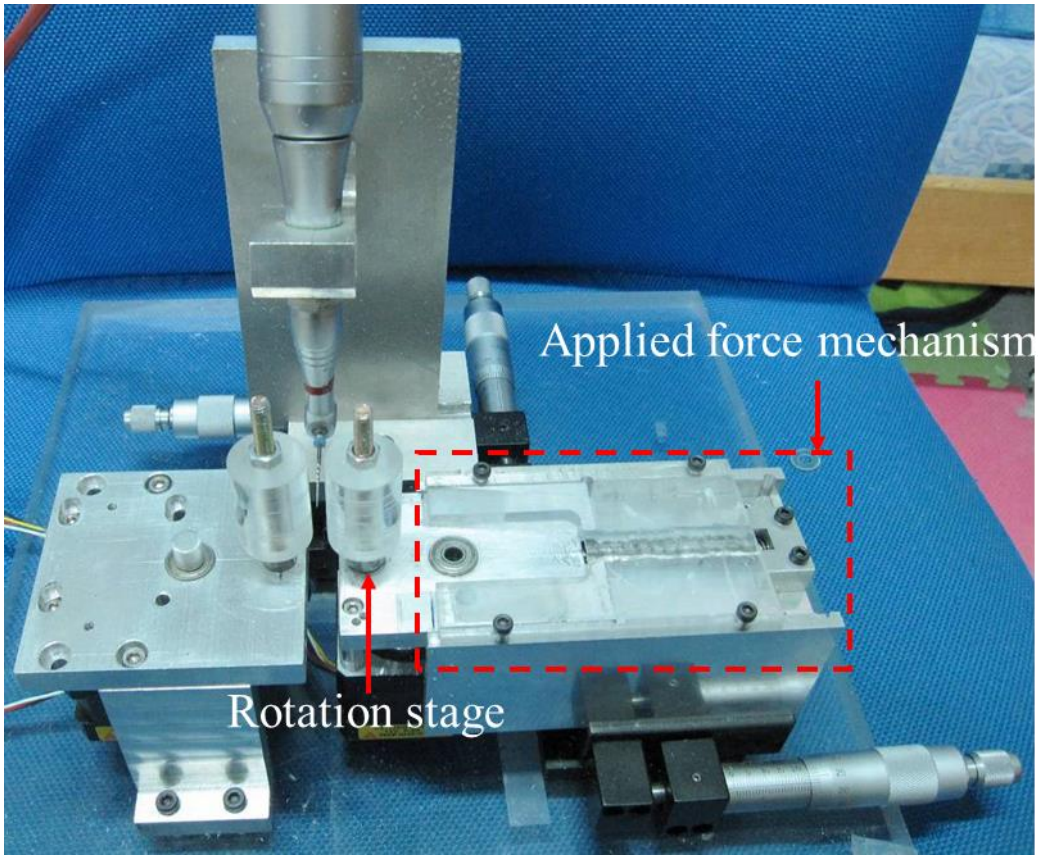

Fig.3-3.Cutting efficiency testing machine [88].

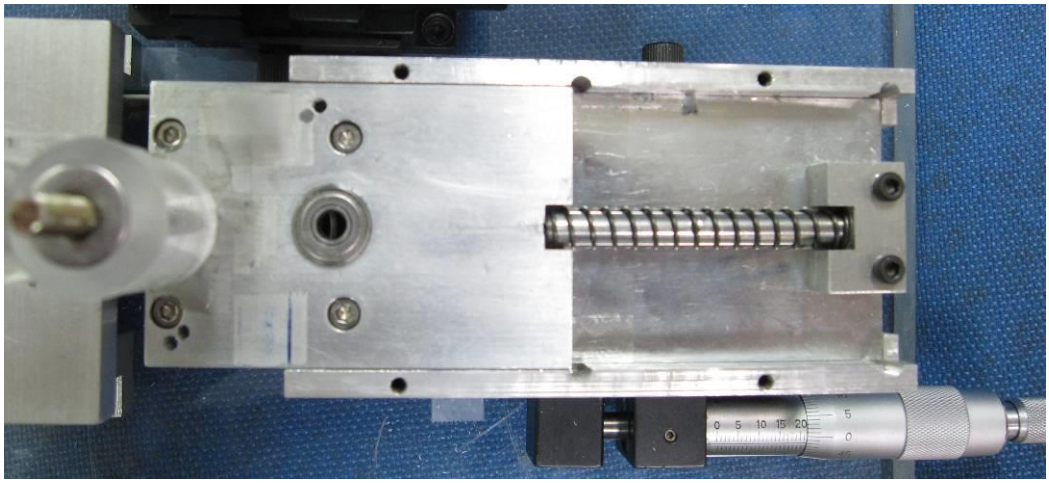
Fig.3-4. Applied force mechanism [88].

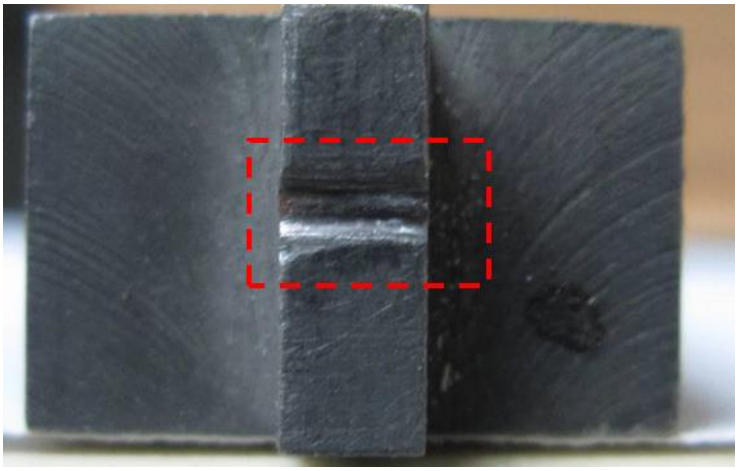

Fig.3-5.Side view of metal sliding block with around 2mm dent to improve cutting stability[88].

3.2.2 Cutting mode

Several materials had been used in literatures for efficiency measurement, such as different kinds of resin or animal bones. In this study, acrylic cylinder as shown in Fig.3-6 is used as the material of testing since it's cheap and easily to get. Its dimension is 20mm in diameter, 30mm in height and 5mm in diameter of the central hole. The position relationship between the acrylic cylinder and the file is shown in Fig.3-7. When the rotary instruments obtained the lateral force from spring, both of two acrylic cylinders will be cut, while the left one rotating clockwise and the right one rotating counterclockwise. Contact surface continuous updating so that the condition of cutting process can be seen as a consistent process, making the cutting mode closer to the actual situation. After the process is done, one can easily measure the loss of mass and finding the cutting efficiency by dividing the operation time.

In this study, the cutting efficiency was done by the operating instruments for 40 seconds to get the enough cut chips for evaluation. Efficiency can then be derived by 1.5 times the amount cut during this time.

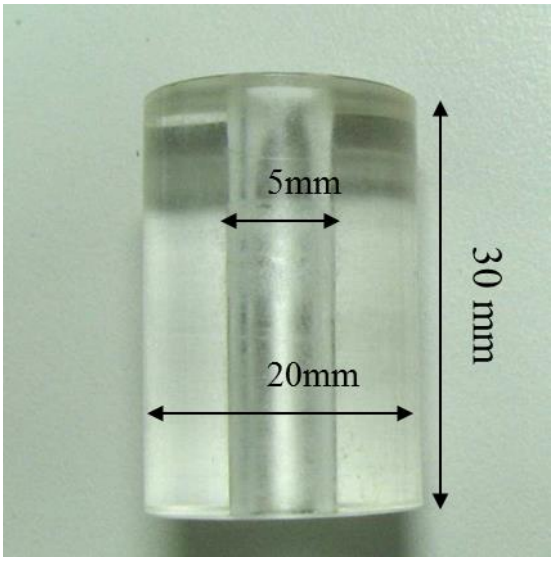

Fig.3-6.Acrylic cylinder for cutting efficiency testing.

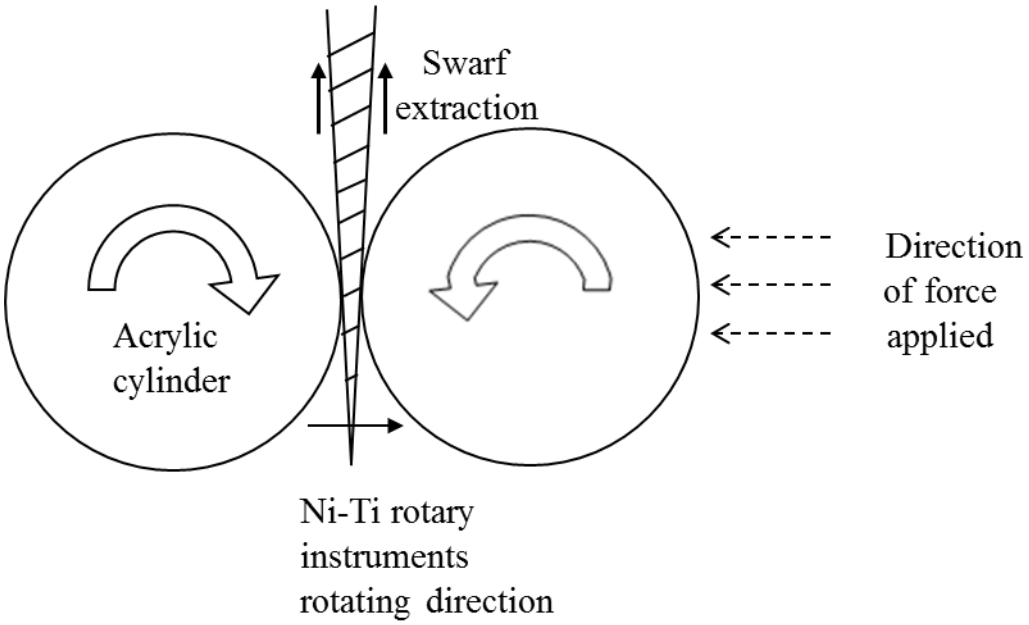

Fig.3-7.Schematic view of cutting efficiency test.

3.3 Heat treatments

3.3.1 Background of heat treatment in Ni-Ti rotary instrument

Ni-Ti alloy's shape memory effect and super-elastic properties are closely related to the heat treatment during manufacturing process. Although the manufacturing process is a business secret, but in general, such process is first to cast Ni-Ti alloy into ingots in a vacuum environment, then after a series of heat treatments, forging, rolling and pulling will be applied in the end to have a needle shape. To have a good shape memory effect and super-elasticity, usually it requires $450°C$ and $550°C$ [4],40]. Previous researches showed that the additional heat treatment will affect the mechanical properties of Ni-Ti instruments. The annealing process is usually accompanied by decreased hardness, which may cause the decreases in cutting efficiency [89]. However, there were also studies indicating that annealed Ni-Ti alloy will have better super-elasticity [90],91]. Moreover, recent studies showed that Ni-Ti alloy will produce complex multi-stage phase transformation under specific aging/heat treatments.

Zinelis*et al*. applied different temperature of heat treatment to discuss the fatigue life. He found the sample with optimal fatigue life is under $430°C$ heat treatment [92]. Sadrnezhaad*et al*. mentioned that when the temperature of heat treatment up to $600°C$, it will makes Ni-Ti alloy recrystallization, and the hardness will decrease. Furthermore, he proposed four reasons that cause the hardness decrease[82]:

1. R-phase(rhombohedral) structure type

2. Martensite structure type

3. Crystal structure rearrangement (recrystallization)

4. Crystal structure transformation between order and disorder.

Huang et al. applied Differential Scanning Calorimetry (DSC) to detect phase transformation and found different annealing temperature will makes Ni-Ti phase

transformation temperature change. The strength of Ni-Ti alloy will decrease when annealing temperature increase [93].

The total heat treatment parameters is: HT400; HT600; HT400+HT600; CT. In this study, heat treatments were done by four steps: (1) fast heating (10°C/min); (2) slow heating (5°C/min); (3) temperature holding (15mins); (4) furnace cooing to room temperature. For example, HT400 means the goal temperature is 400°C, including fast heating before 350°C.The temperature-time data in HT are shown in Fig.3-8Temperature curve of HT400.andFig.3-9.

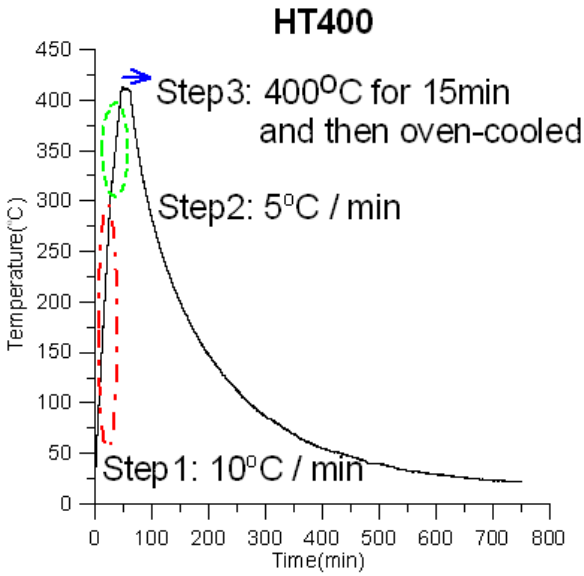

Fig.3-8Temperature curve of HT400.

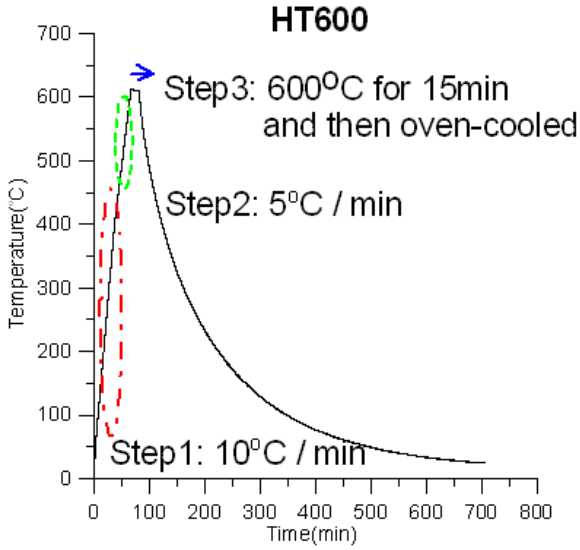

Fig.3-9Temperature curve of HT600.

3.3.2 Cryogenic treatment

Cryogenic treatment uses liquid nitrogen as a refrigerant, cooling the temperature of work piece down to $-196°C$, then hold the temperature for some time before it rises back to room temperature. The temperature control graph is shown in Fig.3-10, which can be divided by three stages: stage1 is−0.2°C/min; stage2 for 30hrs; stage3 is 0.2°C/min. It is also found that by applying cryogenic treatment on the work piece, the fatigue limit resistance improved in

AISI4340 steel [94], the durability increased about 90% to 200% in HSS W18, W9 and W6. In general, cryogenic treatment can affect the material in the following:

1. Making retained austenite transfers into martensite completely.

2. Eliminating the residual stress in the material.

3. Improving durability.

4. Making material structure more uniform.

Although a number of investigations into various effects of cryogenic treatment had been proposed, however, they mainly focused on the steel, and the investigations in Ni-Ti material is still lacking. Nevertheless, based on the concept of cryogenic treatment, it is expected that one can get better cutting efficiency after the treatment. In this study, we applied this technique to the sample which is after heat treatment, trying to extend the fatigue life without compromising with cutting efficiency.

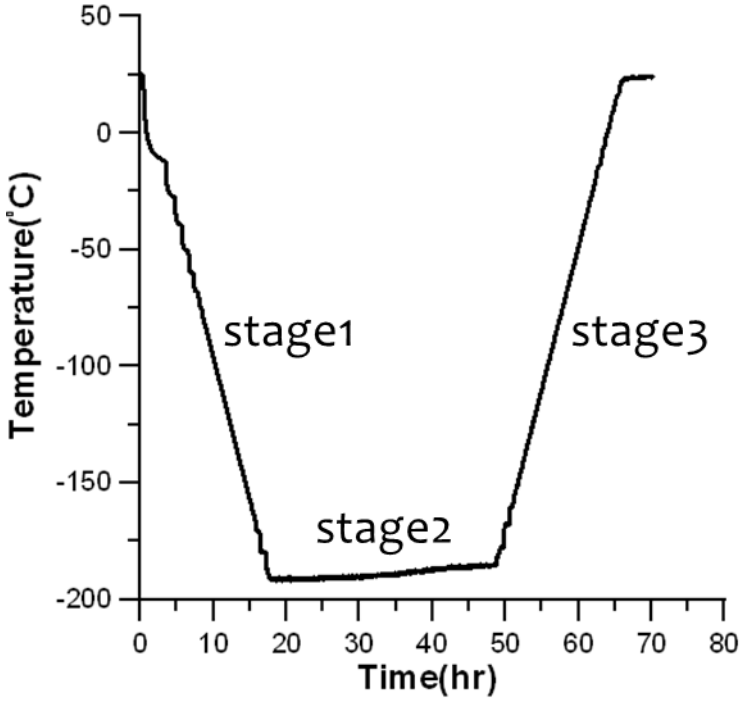

Fig.3-10.Temperature graph of cryogenic treatment: stage1 is−0.2^{o}C/min; stage2 for 30hrs;

stage3 is 0.2^{o}C/min.

3.3.3 Differential Scanning Calorimetry (DSC)

Differential Scanning Calorimetry is a thermoanalytical technique in which the difference in the amount of heat required to increase the temperature of a sample and reference is measured as a function of temperature. The basic principle underlying this technique for phase transition detection in a certain material is that when the sample undergoes a physical transformation, more or less heat will need to flow to it than the reference to maintain both at the same temperature. Whether less or more heat must flow to the sample depends on whether the process is exothermic or endothermic. For example, as a solid sample melts to a liquid, it

will requires more heat flowing to the sample to increase its temperature at the same rate as the reference. This is due to the absorption of heat by the sample as it undergoes the endothermic phase transition from solid to liquid. Likewise, as the sample undergoes exothermic processes such as crystallization, less heat is required to raise the sample temperature. By observing the difference in heat flow between the sample and reference, differential scanning calorimeters are able to measure the amount of heat absorbed or leased during such transitions.

In the current study, the DSC we used is provided by Instrumentation Center of National Taiwan University, and the model is TA Instrument 5100.

3.4 Reciprocating movement in rotary instruments

Reciprocating movement is a method to balance the force applied on rotary instruments in clinical therapy, so that instruments can get better performance in both cutting efficiency and fatigue lives. In 2008, Yared first proposed the effect of reciprocating movement on cutting. The single cycle of reciprocating movement is to rotate the file counterclockwise by 144 degrees, then clockwise by 72 degrees. Therefore, one cycle of movement will generates 72 degrees increment in counterclockwise direction.After 5 cycles of movement, the rotary instrument is recognized as one complete cuttingcycle ($72\times5=360$)[95]. In 2010, De-Deus employed this concept on fatigue testing of ProTaper F2. The results showed that the rotary instruments have longer fatigue life cycles compared with tradition method under same operation speed 400 rpm [96]. However, his experimental parameters design has 2 defects:

1. Reciprocating movement is achieved under variable motion since the step motor is continuously moving back and forth; it needs time for accelerating and decelerating.
2. Both the actual rotation cycles and the reciprocating movement cycles is an improper way to evaluate the fatigue lives on a common basis. Therefore, an equivalent fatigue life definition is needed.

3.4.1 Definition of equivalent fatigue life in reciprocating movement

So far, the operation speed 400 rpm is most welcomed by dentists in clinical therapy. However the unit rpm becomes meaningless for describing reciprocating movement. The reason is because when the experiments in designed to rotate back and forth in a small angle, rotary instruments is actually governed by pure acceleration/deceleration rather than constant speed. Moreover, even the angle is set as 45 degrees; the actual rotation speed doesn't have any significant difference between 350 rpm and 450 rpm. In this study, we controlled the normal operation cycles per minute same as the reciprocating movement cycles per minute. The cycles per minute is set as 400 in this study. Therefore, the equation of equivalent cycles can be computed as:

$$\left(\text{Cycles of reciprocating movement in } \theta \text{ angle}\right)\times\frac{2\theta}{360}=\text{Equivalent cycles} \qquad (2.1)$$

For example, if the reciprocating movement in 45 degree undergoes 10000 cycles, it equivalents to 2500 cycles in normal operation.

3.4.2 The selection of increment angle

The main purpose of rotary instruments is to remove the diseased tissues in the curved root canals. Therefore, we need an increment angle for each reciprocating movement cycles in order to have the function of cutting. Furthermore, since the canal will be cut away by the first cycle of reciprocating movement, the second cycle of such movement will do nothing if we don't give rotary instruments the fresh cutting surface. To have a good idea on increment angle selection, we may need to discuss the stress distribution first.

In general, the maximum tension stress appeared at the certain point of rotary instruments when normal operation applied. This is coincides with the SEM photos of fracture surface. However, if we applied the concept of increment angle into reciprocating movements, we may able to make the maximum tension stress uniformly distributed on the surface. By dividing one rotation cycle into 360 phases and analyzing the frequency of maximum tension stress appears in each phase, we can plot the profile of stress distribution in different increment angle [97]. Fig.3-11 and Fig.3-12 shows the appearance times of maximum tension stress at different phase for increment angle 7 and 27. Obviously, compared with increment angle 27, the increment angle 7 has better performance on the concept of uniform stress distribution. In the current work, we defined the increment angle α as: every 10 cycles of reciprocating movement in θ range, we move back $\theta - \alpha$ before next 10 cycles of reciprocating movement.

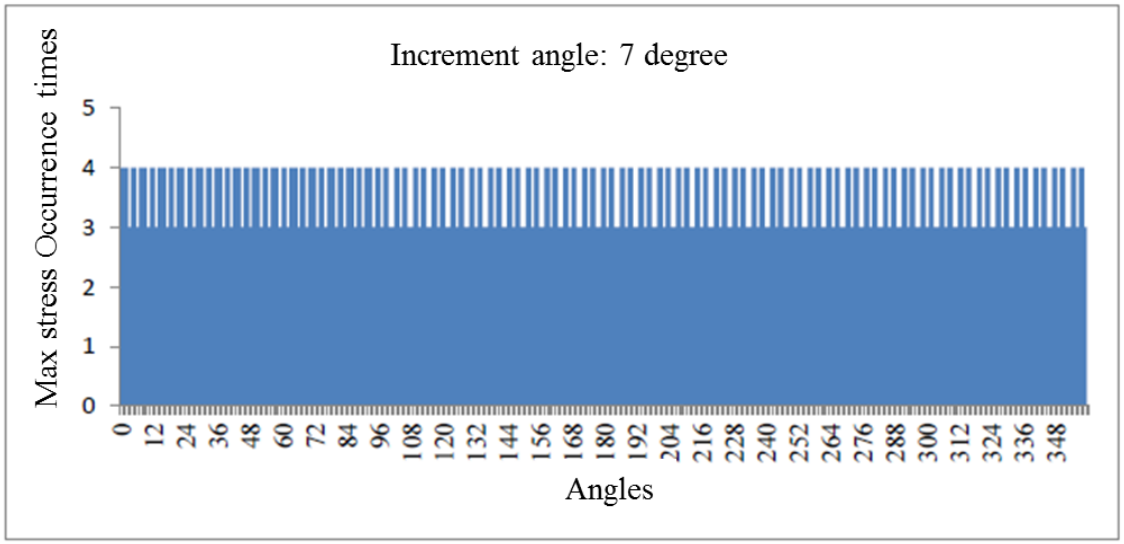

Fig.3-11. Maximum stress appearance times in different angle with increment angle of 7 degree[97].

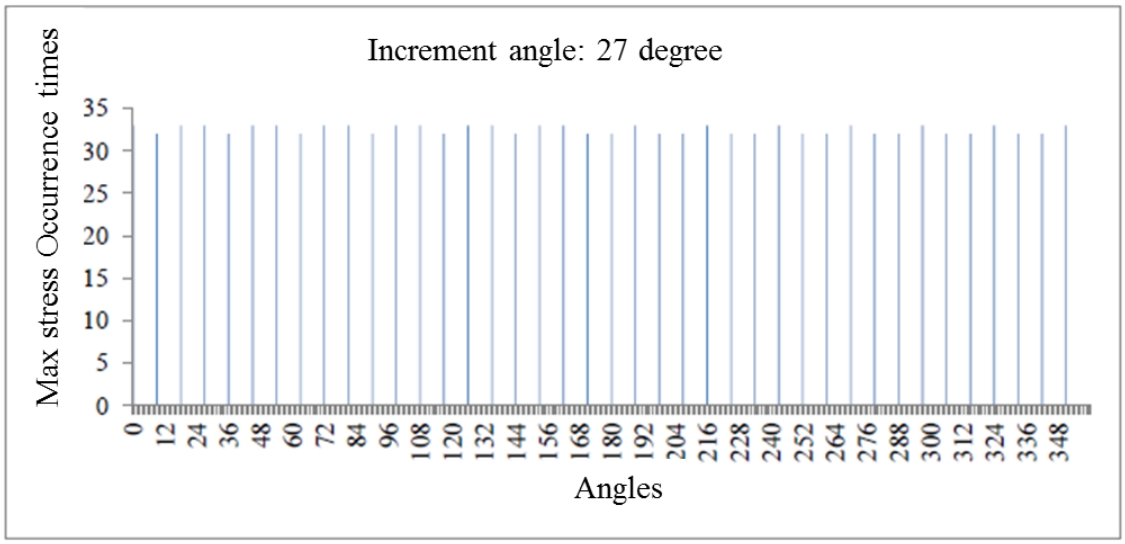

Fig.3-12. Maximum stress appearance times in different angle with increment angle of 27 degree[97].

3.4.3 Cutting efficiency experimental process

To have a good idea of cutting efficiency in reciprocating movement, we must avoid the condition that the chip is too small to measure precisely. Therefore, unlike the parameters used in fatigue test ($\theta = 45°$, $\alpha = 7°$), here we use ($\theta = 45°$, $\alpha = 31°$) as our cutting parameters. In general, the more chips cut away by the Ni-Ti needles means the better cutting efficiency we have. However, the needle has certain tapper in exterior; this makes different position of the needle may have different cutting performance. The total effective cutting region length of the needle is 16mm defined 2mm from the tip. To simplify the problem, we divided the residual length as four regions shown in Fig.3-13: position1 (2 to 4.5mm), position2 (4.5 to 7mm), position3 (7 to 9.5mm), position4 (9.5 to 12mm).

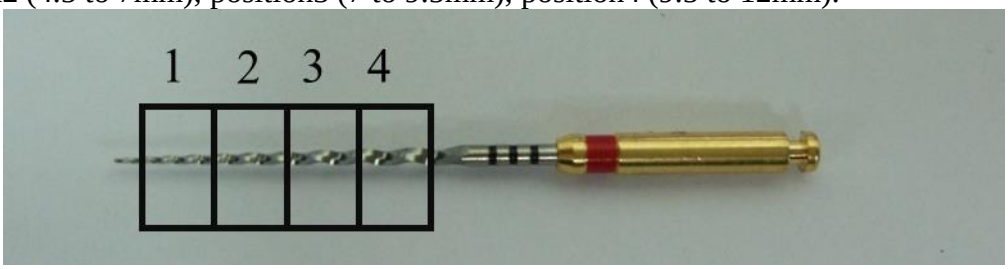

Fig.3-13.ProTaper F2 cutting position definition.

3.4.4 The cutting experimental process

First, we applied ultrasonic cleaner and dishwashing liquid to clean off the residual dusts and oil from acrylic cylinder, then measuring its weight before cutting experiment. After the measurement, the acrylic cylinder was placed on the rotating seat and locked to prevent sliding. The endodontic file was clamped by the step motor and positioned at the height/feed we want. After finishing all the procedures above, we applied 10N force on the endodontic file to ensure the two acrylic cylinders stay close to each other.

In clinical therapy, one endodontic file usually operated no more than 10 seconds. Therefore, the effect of chips affect the cutting efficiency is limited. However, in our experiment, in order to increase the cutting amount, we set the total non-stop cutting time as

40 seconds, resulting in the serious problem in excluding chips. For this problem, we applied the air spray to remove the chips in the whole process.

After cutting, two acrylic cylinders were put into ultrasonic cleaner again to remove residual dusts. By measuring the weight difference, we can get the cutting efficiency as follows:

$$\frac{\left[\left(\mathrm{BW}_{\text{left cylinder}} + \mathrm{BW}_{\text{right cylinder}}\right) - \left(\mathrm{AW}_{\text{left cylinder}} + \mathrm{AW}_{\text{right cylinder}}\right)\right]}{40\,\mathrm{sec}} \times \frac{3}{2} = {}^{mg}\!/_{\min} \quad (2.2)$$

Each position was done by five times and each time was done by three cycles not only to increase the cutting amount but also to check the wearing phenomenon. The detail experimental parameters is listed in Table 3-1.

Table 3-1.Parameters of cutting experiment.

Applied force	10N
Diameter of cylinder	20mm
Cutting time/cycle	40sec
Cutting times/position	5times
θ	45°
α	31°

3.5 Fatigue and cutting testing parameters

Four combinations of radius Rand angular extents of insertion θ are R7.5θ40, R10θ60, R7.5θ60 and R5θ60. The specimens were video-recorded during testing, thus the exact time of fracture could then be accurately determined through playing back the video. The instruments were operated by a DC servo motor (CS60-150C5AE, CSIM Inc., Taipei, Taiwan) driven by a servo driver (CSBL900, CSIM Inc., Taipei, Taiwan). The driver was controlled by a motor controller (PCI-7390. National Instrument, Austin, TX, USA) through a program written in Labview (National Instrument, Austin, TX, USA).

In the current work, both continuous rotation (CR) and progressive reciprocating (PR) were examined under four curvature conditions: R7.5θ40, R10θ60, R7.5θ60 and R5θ60 with four heat treatments: HT400, HT600, CT and HT400+HT600,which means two HTs combined together and were finished in order of precedence. For each condition, five instruments were tested. A progressive reciprocating (PR) was designed in a three-number code ±45°/10rc/+7°, meaning a stationary reciprocation of ±45° with an angular increment of +7° on completion of 10 reciprocating cycles. The average rotation speeds in progressive reciprocating were set to be equivalent to 400 rpm in the continuous rotation (CR). The number of reciprocating cycle per minute was confirmed by stroboscope (PK-DS-112, Pokai technology, Taipei, Taiwan). We quantified fatigue life in progressive reciprocating motion by the total angular distance traveled before fracture, measured in terms of equivalent revolutions.

Both fatigue and cutting efficiency testing parameters are listed in Fig. 3-14. It is worth mentioning that cutting efficiency test was done by an angular increment of 31° for the purpose of enlarging the amount of the cut chips to have better accuracy.

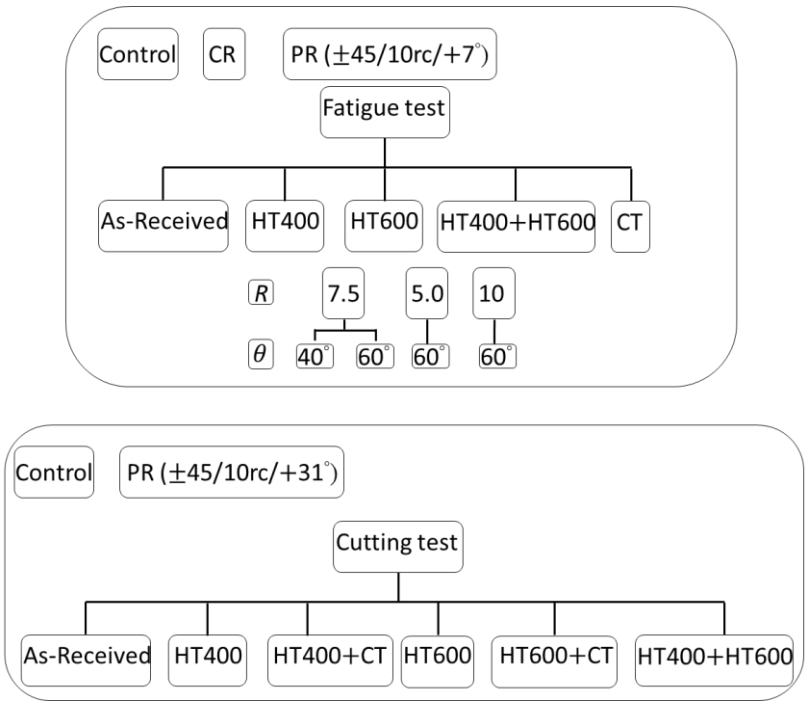

Fig. 3-14. Fatigue and cutting efficiency testing parameters employed in this thesis: CR: continuous rotating motion at 400rpm; PR: progressive reciprocating motion at an equivalent seed of 400rpm in CR.

Statistical significance of fatigue life under different heat treatments was checked for using one way ANOVA and Bonferroni post hoc test at $p<0.05$ with a statistical analysis software (SPSS 20, IBM, NewYork, NY, USA)

3.6 Fatigue failure monitoring system

In clinical therapy, the most effective way to prevent unexpected fracture is nothing else but to develop a monitoring system. Warning of an imminent fracture during clinical use will be a great help to avoid medical and legal complications. A monitoring system employing Fiber Bragg Grating (FBG) has been attempted. The reason of using FBG is its small size which is very promising in integrating with the handpiece of the endodontic equipment. When cracking developed in a rotary instrument, we expect the natural vibration frequency of the instrument changes. If we pick up the stress wave transmitted through the structure components of the rotary instruments, we may be able to detect the occurrence of a crack.

In the current work, we found that we can successfully locate the operation period in the time domain by picking up and analyzing the sound wave using FBG. Furthermore, by employing Fast Fourier Transform (FFT) on the signal, we can reveal the energy variation and the frequency shifting phenomenon in the specific section of the frequency domain. For some characteristic frequencies, it was found that with this information, the fatigue failure of the rotary instruments can be closely monitored to avoid unexpected fracture. The experimental setup will be introduced in this section.

3.6.1 FBG wavelength interrogation system

In this study, we use the intensity modulation principle to generate the corresponding power variation of output light to FBG wavelength shift [98]. By comparison, intensity modulation schemes are economical and simple. An edge filter such as a commercial optical tunable filter (OTF) can be used as to modulate the intensity of reflective light from an FBG. The power of the output light from the edge filter will change as the FBG wavelength shifts. Instead of OTFs, FBGs itself can also be as tunable edge filter and it is even more sensitive than a commercial OTF. As shown in Fig.3-15, the FBG wavelength interrogation system we used consists of an Erbium-Doped Fiber Amplifier (EDFA), creating a steep slope filtered spectrum to modulate the intensity of reflective light content from an FBG. In this system, the reflected light from the FBG filter will be back into the ring to produce a lasing output. This high intensity light is then coupled to the sensor FBG to complete the modulation. The resulting output is converted into voltage signal by the photo detector (PD) for record and analysis.

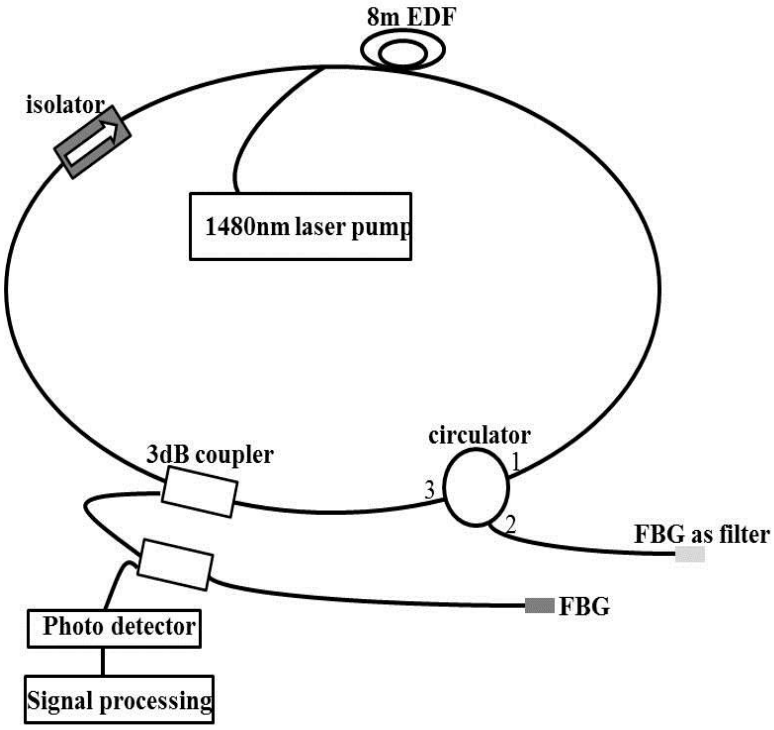

Fig.3-15.Laser ring scheme.

3.6.2 Testing parameters for monitoring system

Two types of commonly used rotary instruments have been explored in this section: ProTaper F2 and Endowave #25 with 21mm length. They are operated at the common clinical therapy in continuous rotating motion at 400rpm. Experimental set up is same as Fig.3-1, with R=10mm and A=60°, was used to simulate the curved root canal. This geometry has been chosen because finite element analysis [81] showed that it imposes a relatively low strain on the file. The strategy is that if we can successfully monitor the sound wave at relatively low strain, we expect that more seriously strained conditions could be also handled. Through the tests, high resolution video camera was used to monitored and record the specimen condition.

3.6.3 Signal processing

The corresponding power variation monitored by the PD was recorded by LabView8.6 software with a 22000Hz sample rate. When the file was not in operation, the pick-up signal contains a high frequency component of roughly 5000Hz and above that reflects the background noise of the system (the related results will be introduced detail in Chapter 4). A software low pass filter with cutoff frequency of 10000Hz was used to remove the background noise before proceeding with FFT analysis. FFT was carried out incrementally, each time on a cluster of 100000 data (corresponding to 4.54 seconds) to get the characteristic frequencies at each instance. The transformed spectrum suggests four potentially informative frequency sections: 20 to 40Hz, 950 to 1000Hz, 1450 to 1500Hz and 1950 to 2000Hz. The frequency with peak value in each of these sections was recorded as the dominant frequency. For instance, if the energy at 21.8Hz has the highest value from 20Hz to 40Hz, we called it the dominant frequency in this frequency section. Through this process, we can monitor the frequency shift and energy variation of the dominant frequency with time for each of four sections.

3.6.4 Fractographic examination

Fatigue failure of metallic materials as mentioned in Section1.2.5, can be divided into three stages: crack initiation, crack propagation and final fracture. The exact crack initiation time is difficult to measure during the fatigue process. However, fractographic study using a SEM can reveal the fatigue striations, each of which corresponds to the crack advance during one loading cycle [99]. Fig.3-16 shows a typical ProTaper F2 fracture surface. A line leading from the crack initiation to the final rupture zone was chosen on each fracture sample's surface we tested. It was separated into two equal sections. The average fatigue striations density was measured in each section. The number of cycles and hence the duration of crack propagation can be estimated from the extent of crack growth distance and the average striation density. This information will be correlated with the signal from the FBG sensors. The data discussions will then introduced in Chapter 4.

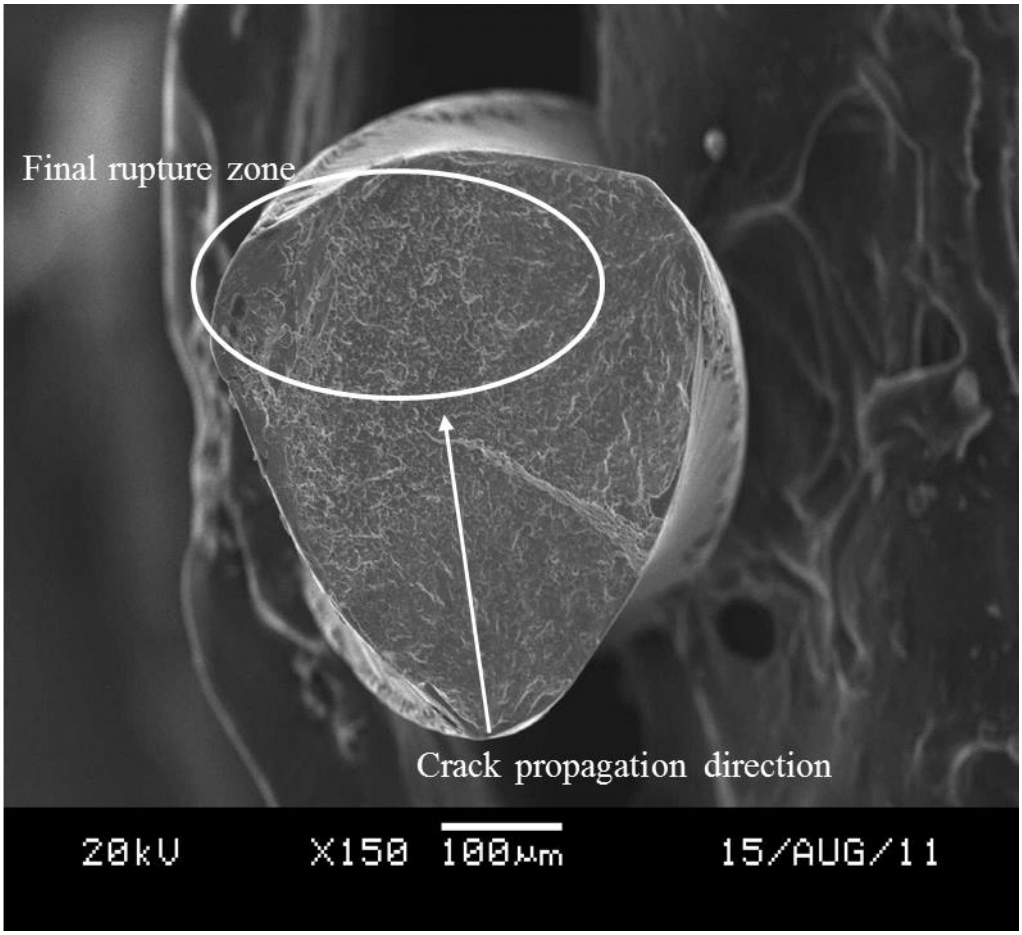

Fig.3-16.Typical Protaper F2 fracture surface.

3.7 The experimental setups and materials of TPP system

3.7.1 The general layout of TPP fabrication system

The general layout of TPP fabrication has been shown in the previous section. The low-cost, doubled frequency Nd:YAG 532nm green laser had been applied. The laser intensity is controlled when passing through the attenuator and the laser beam is expanded by telescope for adjusting the beam size as same as the when beam enters the microscope. A dichroic mirror is used to reflect the laser into the resin for fabrication.

3.7.2 The hardware setups of TPP

There are two setups for different applications in this thesis. For all setups, the resin is dropped on the coverslip with 170nm thickness and fixed on the computer-controlled stage mounted on an inverted microscope. In large structure applications, we use big power laser 1W. The system details shown in Fig.3-17 has travel range $120\times110mm^2$ and 22nm in resolution by applying ASI MS-2000 XY motor-stage, which is mounted on Axiovert 200M Zeiss motorized microscope with 50nm in resolution.

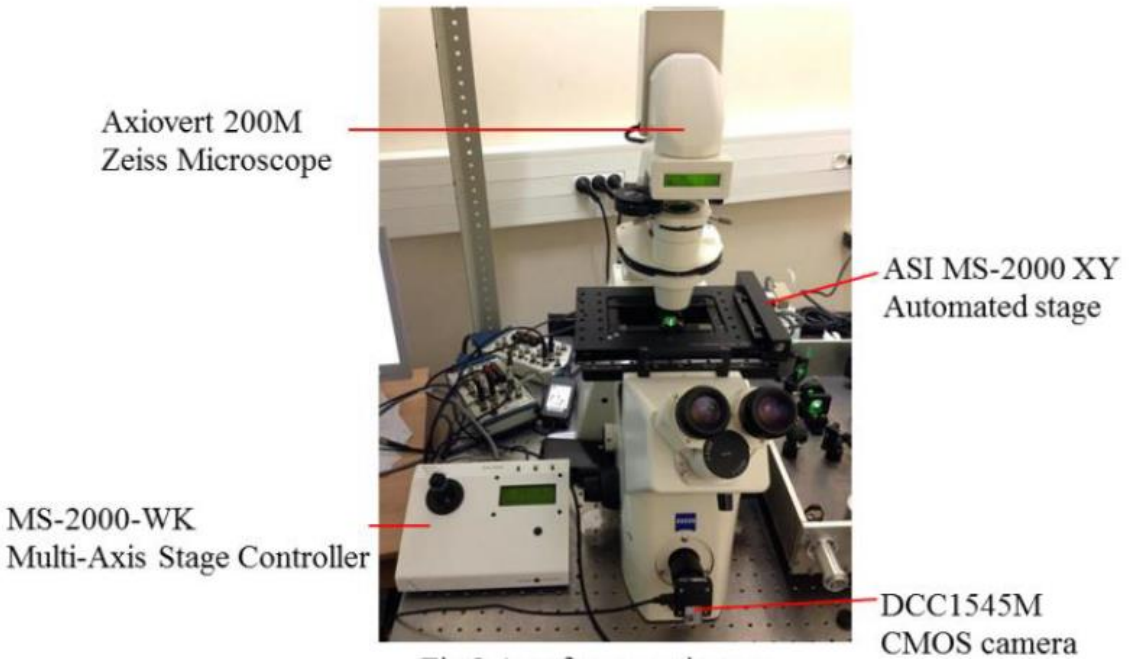

Fig.3-17.Experimental setup with XY motor stage.

For massive parallel beams fabrication in TPP, we employed diffractive optical elements (DOEs) for splitting a collimated beam into several beams. These beams are characterized by an equal intensity and equal angle to one another theoretically. The purpose of this is to realize the mass production at the same time. The system setup is shown in Fig.3-18.and the pattern of laser after the DOEs is shown in Fig.3-19. The distance between each laser point can be interpreted as the effective working distance of massive parallel beams fabrication, and is governed by the distance of gratings on the DOEs. For different DOEs, the working distance is listed in Table 3-2.

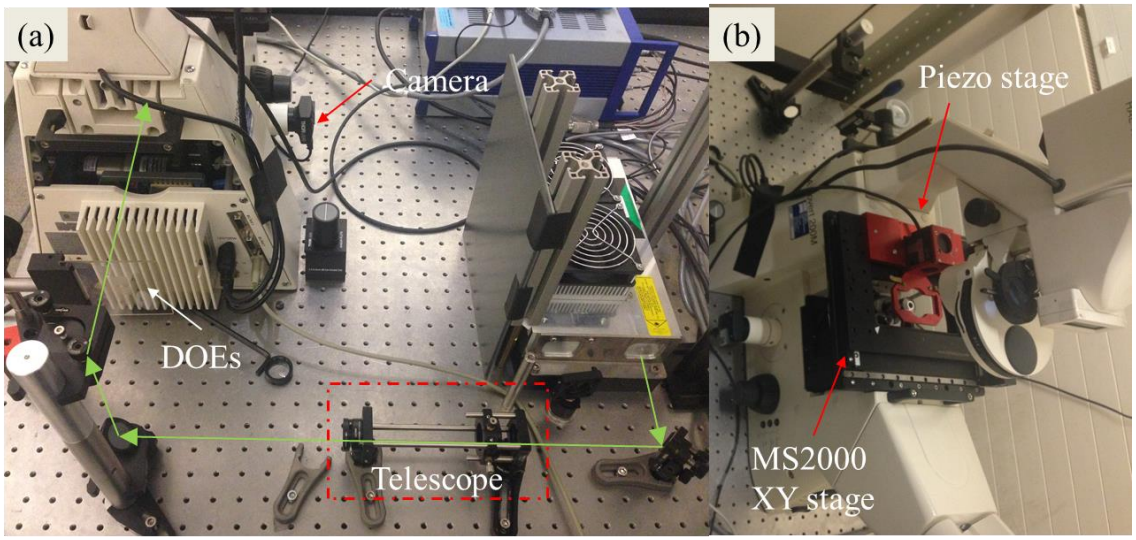

Fig.3-18. Parallel beams fabrication setup: (a) back view, the green arrow indicates the laser path; (b) front view.

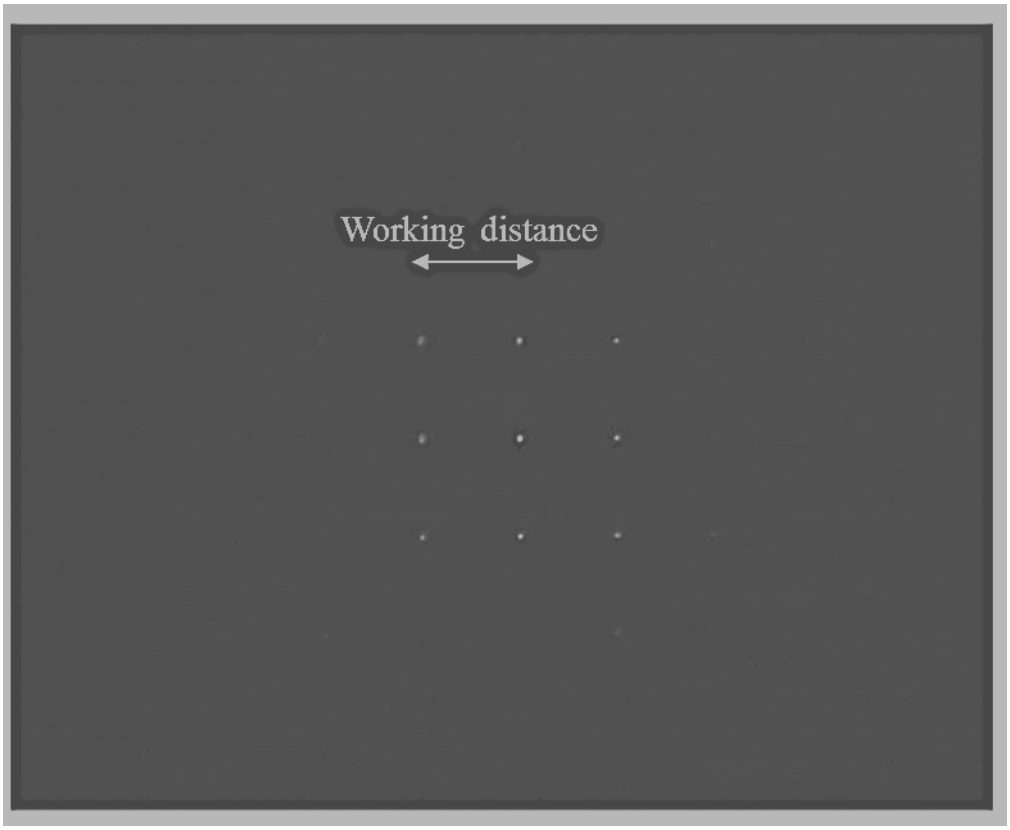

Fig.3-19. The pattern of laser beams after DOEs.

Table 3-2.Working distance in different DOEs.

Types of DOEs/separation angle	Workind distance (μm)
3×3/0.166°	17.16
3×3/0.233°	31.2
47×47/0.446°	0.72
47×47/0.669°	1.01
25×25/0.233°	0.49

3.7.3 The materials of TPP micro fabrication

Two kinds of commercial resin: Photomer 3015 and Ormocomp are used in this thesis for micro-fabrication. The two-photon photon-initiator molecule for Photomer is N,N,N',N'-Tetrakis(4-methosypheny1)benzidine and that for Ormocomp is 1,3,5-Tris(2-(9-ethylcabazyl-3)ethylene)benzene. The photon-initiator molecules can effectively enable the initiation of the polymerization with laser light within the visible wavelength range (500 to 650nm) [100]. Here, we choose 532 nm Nd:YAG as our laser source.

The processes of preparing Photomer and Ormocomp are as follows. For Photomer, the processes are:

(1). Put photo-initiator (3mg) and dichloromethane (CH_2CL_2, 1ml) in a small flask.

(2). Add the solution from first step into Photomer (900mg).

(3). Stir the solution well by using the ultrasonic bath for 1 to 2 hours.

(4). Open the vial to evaporate for one day.

For Ormocer, the processes are:

(1). Dissolve photo-initiator (2mg) in dichloromethane (CH_2CL_2, 1ml) in a small flask.

(2). Add the solution from first step into Ormocer (1g).

(3). Protect the solution from light and stir it well by using the ultrasonic bath for 1 to 2 hours.

(4). Open the vial to evaporate for one day.

3.7.4 The TPP fabrication procedures

The standard fabrication process in TPP is first to construct the structure by CAD, then sliced it into points data to piezo, The overall processes of TPP fabrication is as follows:

(1). Prepare the data of the laser scanning trajectories, each data point represents a voxel position.

(2). Fabricate the products, the laser focal spot follows the trajectories for polymerizing resin.

(3). Immerse the substrate into solvent to remove the unpolymerized resin and remove the solvent by critical point dryer.

(4). Coat the surface of substrate and take SEM photos.

The fabrication system was developed by Nation Taiwan University CADLAB [101]. For preparing the data of laser scanning trajectories, the slicing parameters can be designed by users as shown in Fig.3-20. Such parameters include voxel size, voxel overlap ratio, layer thickness, number of extra offset layer, shell gap, slicing sequence, display condition and the face hatching for slicing. The main function of this software is to slice the CAD model and planning the laser scanning paths. The slicing method is shown in Fig.3-21.

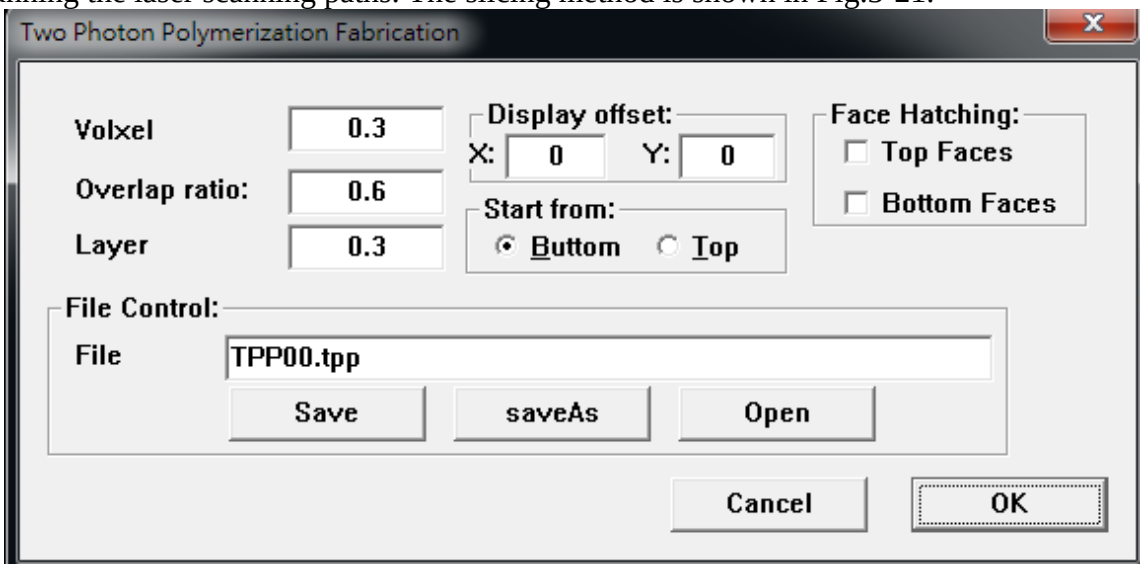

Fig.3-20.User interface of TPP parameters.

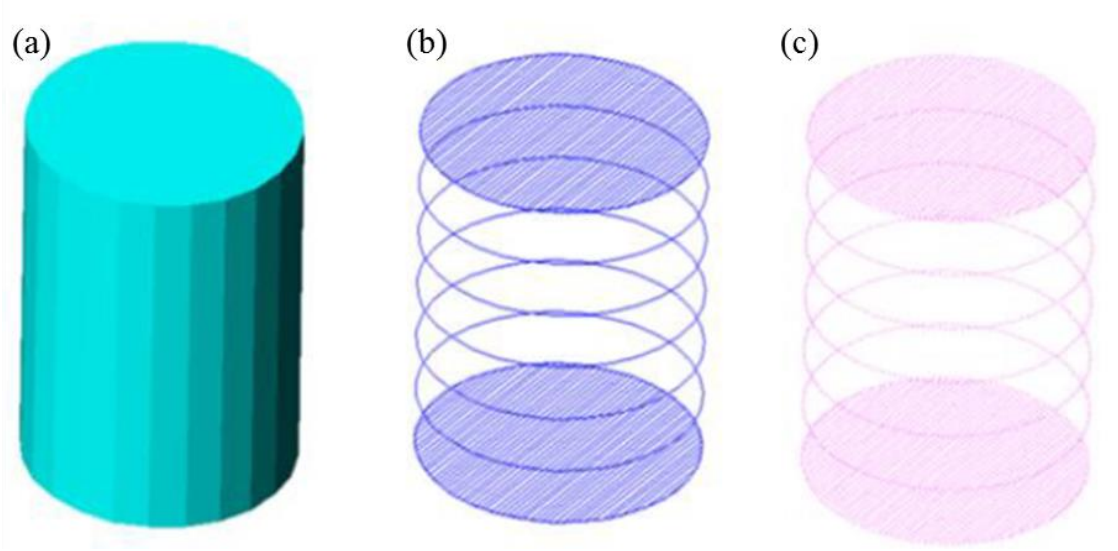

Fig.3-21. Planning and laser scanning process of a solid model: (a) CAD model, (b) slicing contours, (c) scanning paths.

Before fabrication, the tilt correction is applied by using rotation matrix for rotating the horizontal plane into inclined substrate [102]. The interface of the main fabrication working parameters includes the laser power, delay time between paths and the exposure time.

The commercial AutoCAD software was built-in AutoLISPprogram. It is used for exporting the data file for planning the layer manufacturing trajectories with laser scanning paths. The ObjectARX is a programming environment which provides object-oriented C++ application programming interface (API) for customized use and extend AutoCAD. In visual studio C++ 2005 with inputting the export data, the positioning of the stage and laser is controlled.

Chapter 4 Study of rotary instruments

In this chapter, we discuss Ni-Ti rotary instruments in terms of fatigue lives and cutting efficiency, investigating the optimal parameters for clinical therapy. Furthermore, the results of real-time fatigue crack monitoring systems will also be displayed.

4.1 The effect of heat treatment

As mentioned in Section 3.3.3, we use DSC to investigate the phase transformation temperature changes in different heat treatments. Fig.4-1 shows the original ProTaper F2 (As-Received) DSC result, Fig.4-2 is the result after cryogenic treatment (CT), and Fig.4-3 to Fig.4-4 is the result after HT400, HT600 respectively.

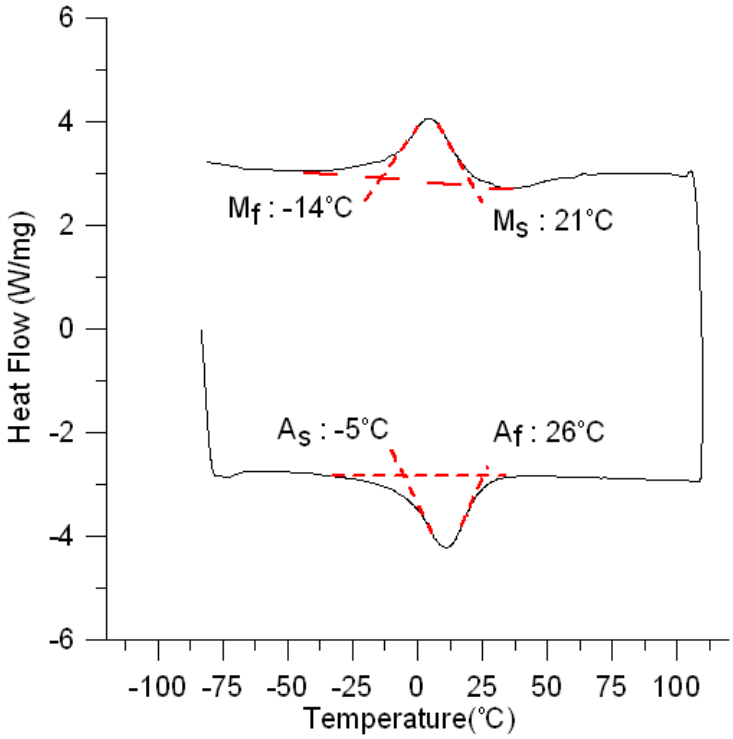

Fig.4-1. DSC result of original ProTaper F2 (As-Received)[103].

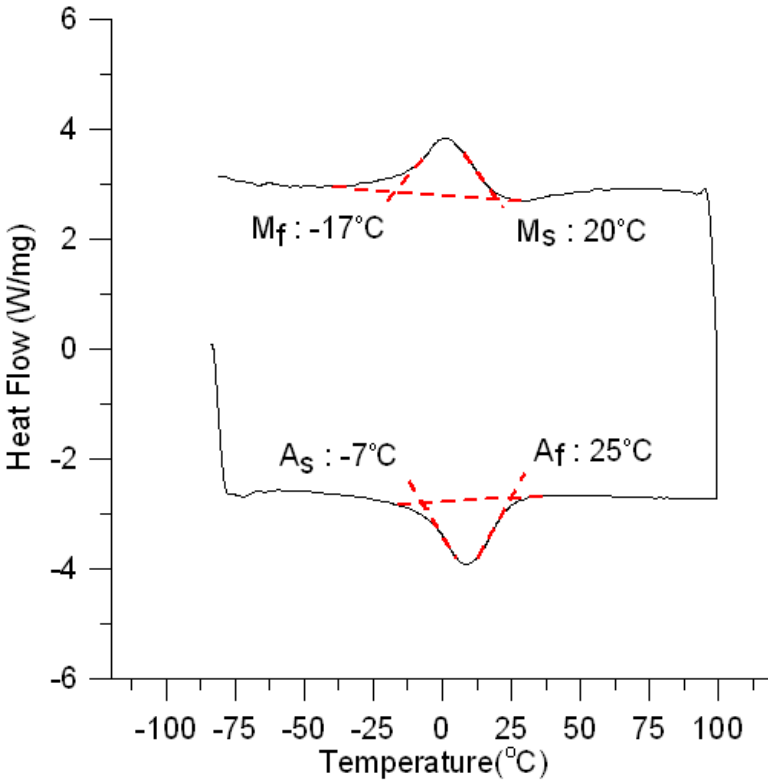

Fig.4-2. DSC result after cryogenic treatment (CT)[103].

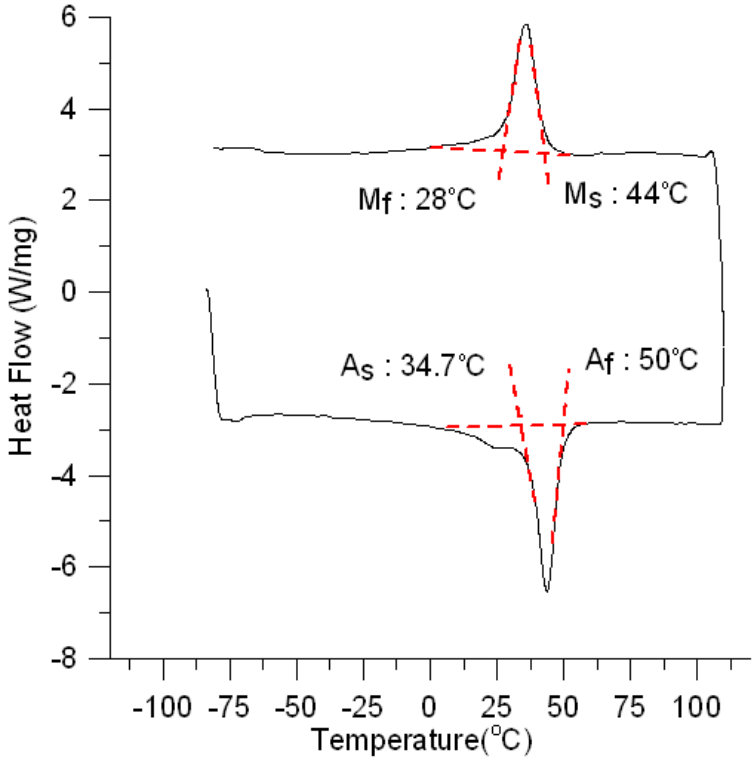

Fig.4-3. DSC result after HT400[103].

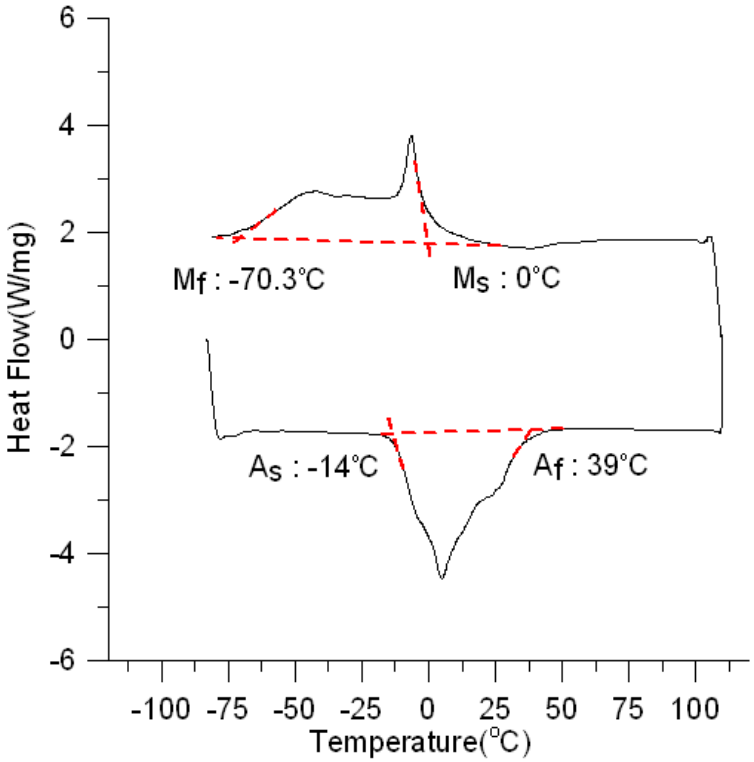

Fig.4-4. DSC result after HT600[103].

From above figures, the DSC result of CT compared with As-Received one is almost the same; however, we found that the DSC curve has significant difference among As-Received, HT400 and HT600. For example, the phase transformation temperature of As-Received is: $M_s = 21°C$, $M_f = -14°C$, $A_s = -5°C$, $A_f = 26°C$, but the phase transformation temperature after HT400 is: $M_s = 44°C$, $M_f = 28°C$, $A_s = 35°C$, $A_f = 50°C$. All of them aremuch larger than the original file. As for the DSC result of HT600, two-phase coexistence range is the biggest. Moreover, by observing different DSC curves in different heat treatments, we can also found that in the room temperature $25°C$:

1. The phase structure is almost austenite in the file as received.

2. The phase structure is almost martensite in the file after HT400.

3. The phase structure is almost austenite when the file after HT600 is in the cooling cycle, while the two-phase structure appears in the heating cycle.

It is worth mentioning that the area of peaks and troughs represents the energy required to initiate phase transformation.Table 4-1 lists the enthalpy changes under different heat treatments. The results showed that the enthalpy change in As-Received and HT400 is almost the same (5.5 to 7.3 J/g); however, the enthalpy change is 16.6 to 19.1 J/g in HT600. Such difference may come from material recrystallization phenomenon. As Ni-Ti alloy undergoes cold working, a large number of dislocations and deformed structures appear, storing a lot of strain energy as an assistance force for phase changing process.

Table 4-1. DSC tests of enthalpy change in different heat treatments

HeatFlow (J/g)	As-received	As-received CT	HT400 15min	HT600 15min

1st.Heating cycle	5.533	5.337	7.359	19.17
1st.Cooling cycle	4.956	4.15	5.818	16.61
2nd.Heating cycle	5.789	5.421	6.883	17.88
2nd.Cooling cycle	4.558	4.058	5.493	16.23

4.2 Fatigue life in normal operation

To understand the effect of heat treatment on Ni-Ti rotary instruments, we applied four different parameters of heat treatment (HT400, HT600, HT400+HT600 and CT) and four different strains (3.18%, 3.44%, 3.8% and 4.25%) in ProTaper F2, working at 400 rpm.

Fig.4-5and Appendix 1shows the results of fatigue life in R7.5A40° ($\varepsilon = 3.18\%$). Data shows that the average life of HT400 has the longest life (3450.1 cycles) which is 2.43 times the life in As-Received file. The enhancement (%) arranged according to amount is HT400 (143%), HT400+HT600 (132%), HT600 (124%) and CT (35%).

Fig.4-5 and Appendix 2 shows the results of fatigue life in R10A60° ($\varepsilon = 3.44\%$). Data shows that the average life of HT400 has the longest life (1891.26 cycles) which is 2.22 times the life in As-Received file. The enhancement (%) arranged according to amount is HT400 (122%), HT600 (121%), HT400+HT600 (111%) and CT (27%). At this curvature-angle condition, the fatigue life in HT400 and HT600 is almost the same.

Fig.4-5 and Appendix 3shows the results of fatigue life in R7.5A60° ($\varepsilon = 3.8\%$).Data shows that the average life of HT600 has the longest life (3550.48 cycles) which is 5.13 times the life in As-Received file. The enhancement (%) arranged according to amount is HT600 (413%), HT400+HT600 (363%), HT400 (138%) and CT (12%).

Fig.4-5 and Appendix 4 shows the results of fatigue life in R5A60° ($\varepsilon = 4.25\%$). Data shows that the average life of HT400+HT600 has the longest life (2750.66 cycles) which is 4.54 times the life in As-Received file. The enhancement (%) arranged according to amount is HT400+HT600 (354%), HT600 (285%), HT400 (112%) and CT (10%).

In all cases, HT400 has around 112% to 143% enhancement of fatigue life. Deducing the reasons for such improvement is material phase structure. According to Fig.4-3, the phase structure at room temperature is almost martensite in the instruments after HT400 treatment; however, the phase structure in As-Received one is almost austenite at the same temperature. This implies that the martensite phase is good for fatigue resistance. Such evidence also coincides with previous scholars' result, indicating that the crack propagation speed in martensite is lower than in austenite [18].

In all cases, HT600 has around 121% to 413% enhancement of fatigue life. Deducing its reason is recrystallization. It is observed that Ni-Ti alloy has recrystallization phenomenon when experiencing $500\,^{\circ}C$ environment. The grain re-growth eliminates the residual stresses of endodontic files, decreasing the crack propagation speed, thus improving the fatigue life.

From above discussions, it is expected that by combing two mechanisms of improving fatigue life will have the longest life. HT400+HT600 also plays good performance, and has around 111% to 363% enhancement. Although it neitheras good as HT600 in R7.5A60° (413%) nor as good as HT400 in R10A60° (122%), it still has medium performance between two heat treatments.

As for CT treatment, it has around 10% to 35% enhancement compared with As-Received one. The enhancement percentage is not as large as other heat treatment. It is because that the function of CT is to transform the residual austenite into martensite phase; however, in the room temperature, As-Received file is almost in austenite phase. Therefore, the residual austenite is not too much to be transformed into martensite to improve fatigue life.

Regarding to the stress-induced martensite (SIM) issue as mentionedin Section 1.2.1, SIM happens only in ε ranging from 1% to 4%. It implies that in the three strain cases (3.18%, 3.44% and 3.8%), Ni-Ti instruments exists different contents of SIM. The more strain

we applies, the more SIM we get. Therefore, SIM contents in R7.5A40° (3.18%) is the smallest, and the contents in R7.5A60° (3.8%) is the biggest. However, no matter what heat treatments we applied on the Ni-Ti instruments, the fatigue life in all three strain conditions arranged according to amount is always: R7.5A40° (3.18%) >R10A60° (3.44%) >R7.5A60° (3.8%).Obviously, although SIM contents get larger when strain increases, martensite phase induced by stress still can't effectively improve the fatigue life of Ni-Ti rotary instruments. Therefore, the crack propagation speed is dominant by strain-induced stress field. The lower strain we applies, the more fatigue life we get.

From all the discussions above, we can plot the S-N curve as shown in Fig.4-6. Generally speaking, the fatigue life arranged according to amount is: HT400+HT600 ≈ HT600 > HT400 > CT > As-Received.

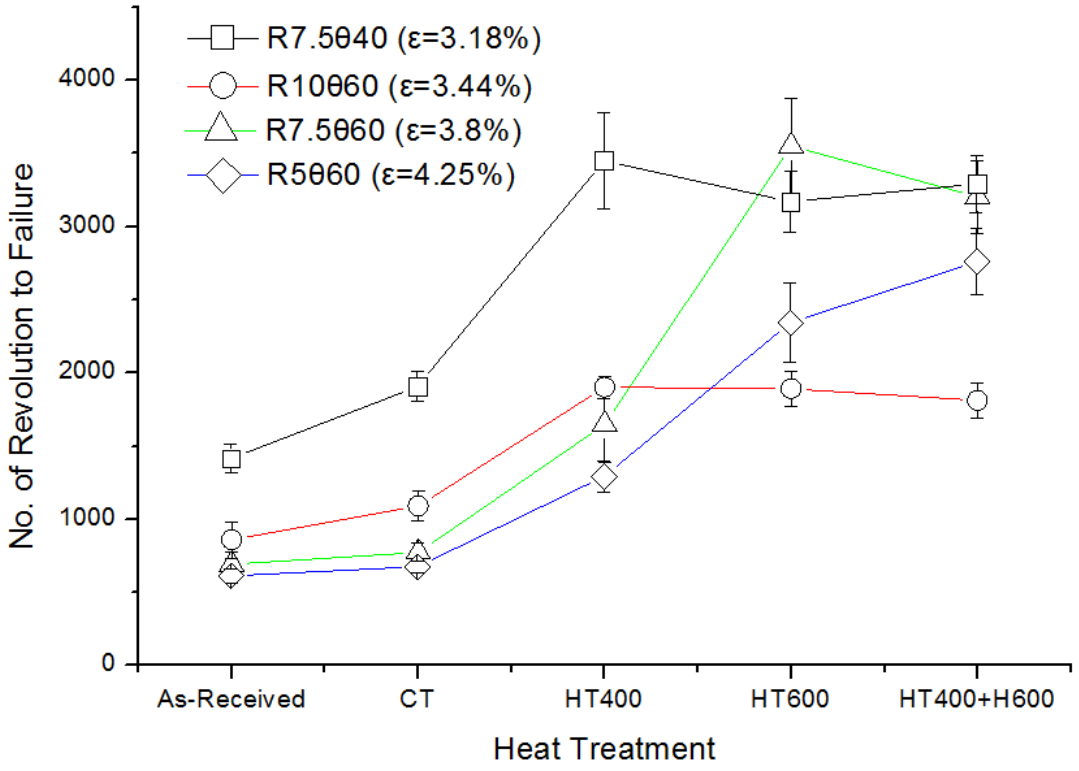

Fig.4-5 Fatigue life in different heat treatment under continuous rotation.

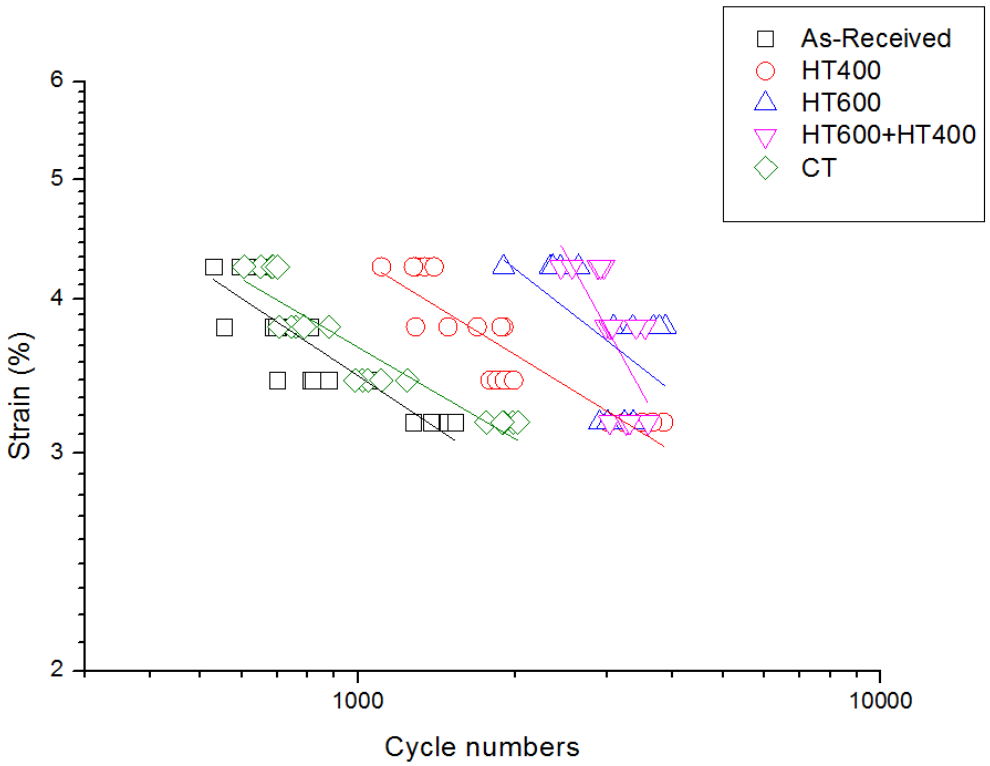

Fig.4-6ProTaper F2 S-N curve.

4.3 Fatigue life in reciprocating movement

In Chapter 3, we proposed a new method to balance the maximum stress distribution in the file. The effect of this method had been discussed by Huang [97], but he mainly focus on the file without heat treatments. He concluded that with the help of reciprocating movement $\theta = 45°$ and increment angle $\alpha = 7°$, one can get the best fatigue life performance on the As-Received files. Here, we apply this criterion to discuss the fatigue life and heat treatment in a new perspective.

Fig.4-7 and Appendix 5 shows the results of fatigue life in R7.5A40° ($\varepsilon = 3.18\%$). Data shows that the average life of HT600 has the longest life (30846.2 cycles) which is 6.42 times the life in As-Received file. The enhancement (%) arranged according to amount is HT600 (542%), HT400+HT600 (431%), HT400 (154%) and CT (59%).

Fig.4-8 and Appendix 6 shows the results of fatigue life in R10A60° ($\varepsilon = 3.44\%$). Data shows that the average life of HT600 has the longest life (25726.6 cycles) which is 6.9 times the life in As-Received file. The enhancement (%) arranged according to amount is HT600 (590%), HT400+HT600 (516%), HT400 (34%) and CT (20%).

Fig.4-9 and Appendix 7 shows the results of fatigue life in R7.5A60° ($\varepsilon = 3.8\%$). Data shows that the average life of HT400+HT600 has the longest life (26646.4 cycles) which is 12.09 times the life in As-Received file. The enhancement (%) arranged according to amount is HT400+HT600 (1109%), HT600 (1031%), HT400 (141%) and CT (9%).

Fig.4-10 and Appendix 8 shows the results of fatigue life in R7.5A60° ($\varepsilon = 4.25\%$). Data shows that the average life of HT400+HT600 has the longest life (18592.8 cycles) which is 7.41 times the life in As-Received file. The enhancement (%) arranged according to amount is HT400+HT600 (641%), HT600 (604%), HT400 (123%) and CT (26%).

From above discussions, the enhancement of different heat treatment working at reciprocating movement $\theta = 45°$ and increment angle $\alpha = 7°$ can be roughly understood as

HT600 ≈HT400+HT600> HT400 > CT > As-Received, which is coincides with the normal rotation fatigue test. The S-N curve is plotted in Fig.4-12. Furthermore, one can easily find the significant difference between normal operation and reciprocating movement. For example, in R7.5A40°, the effect of reciprocating movement can be even up to 872% in HT600 condition (seeFig.4-13).

Traditional rotationusually has only one crack initiation point as shown in Fig.4-14; however if we applied the reciprocating movement on the rotary instruments, we may have several crack initiation points on the fracture surface (see Fig.4-15). By measuring the striation numbers form SEM photos of fracture surface (see Fig.4-16 to Fig.4-17), we found the striation numbers is almost the same as fatigue life in the traditional rotation case; however, a huge difference between striation numbers and fatigue life in the file with reciprocating movement. Table 4-2 shows these comparisons. From this result, we can understand the reciprocating method as a way to prolong the time for initiating a crack since we lower down the maximum stress and make it uniformly distributed on the surface.

It can be expected that if we can combine reciprocating method and right heat treatment, the fatigue life can have extremely good performance; however, one cannot sell the cow and drink the milk, some parameters with excellent fatigue life performance may have bad cutting efficiency. In clinical therapy, cutting efficiency is also an important parameter. After all, Ni-Ti rotary instrument is designed to cut away the diseased tissue in the canal. Therefore, the cutting efficiency related discussions we then be introduced in the next section.

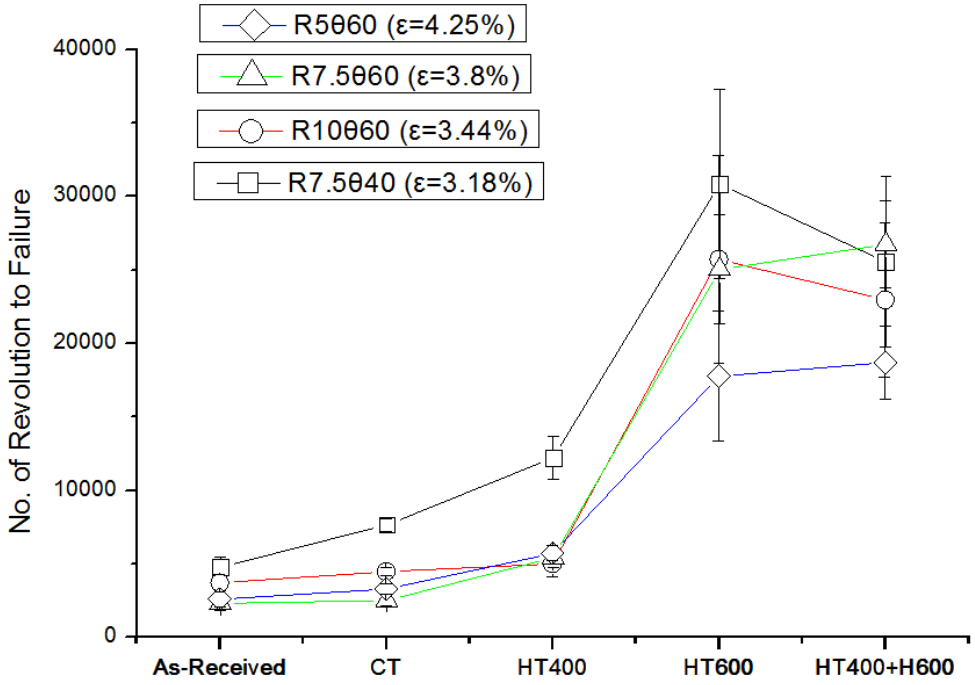

Fig.4-11Fatigue life in different heat treatment under progressive reciprocating motion.

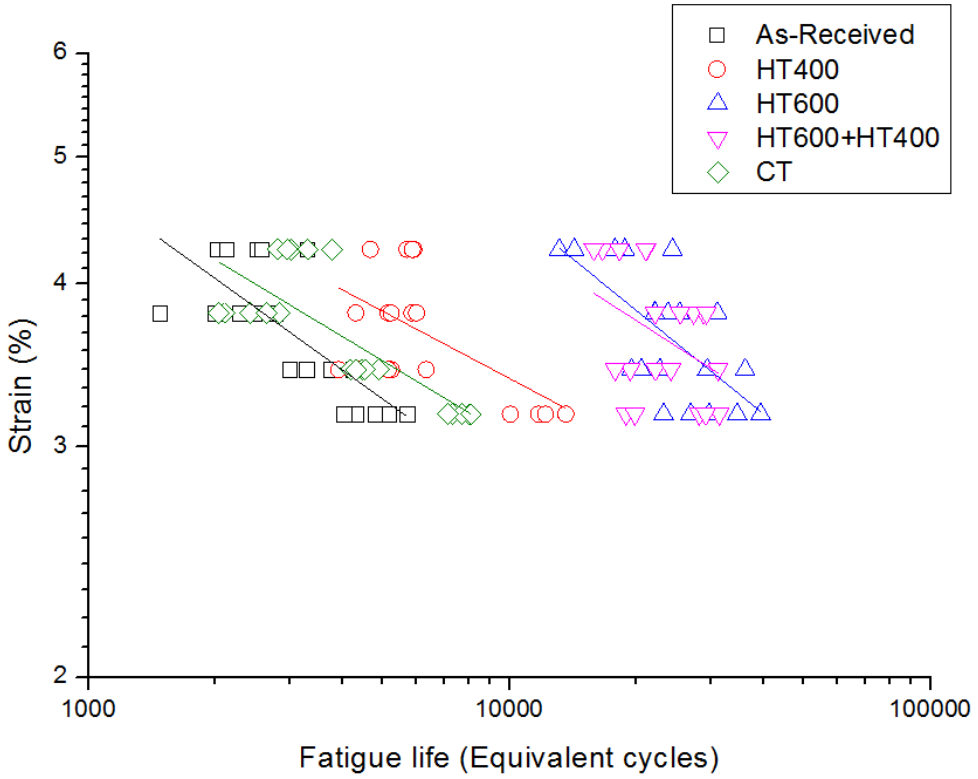

Fig.4-12.ProTaper F2 S-N curve under reciprocating method ($\theta = 45°$, $\alpha = 7°$).

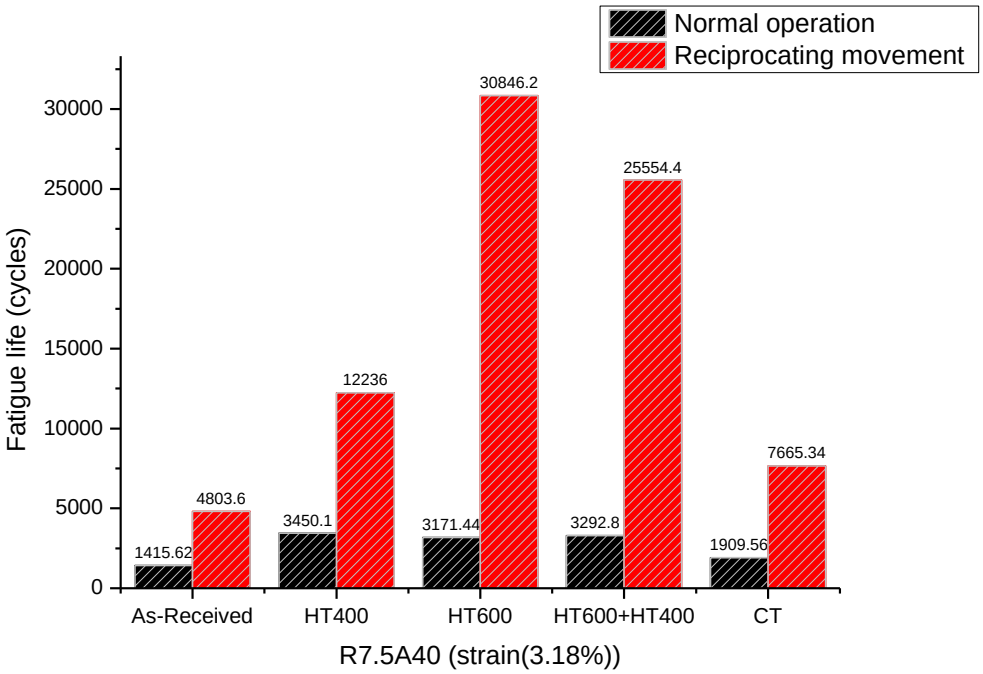

Fig.4-13.Comparison between normal operation and reciprocating movement at R7.5A40°.

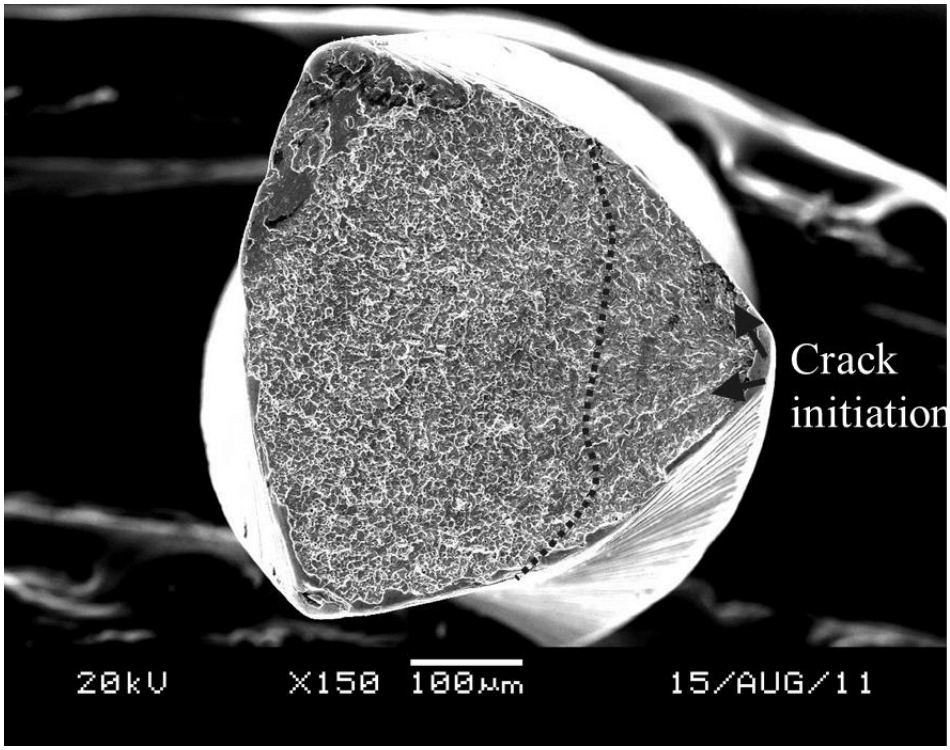

Fig.4-14. SEM photo of R7.5A40° (As-Received) normal rotation fracture surface.

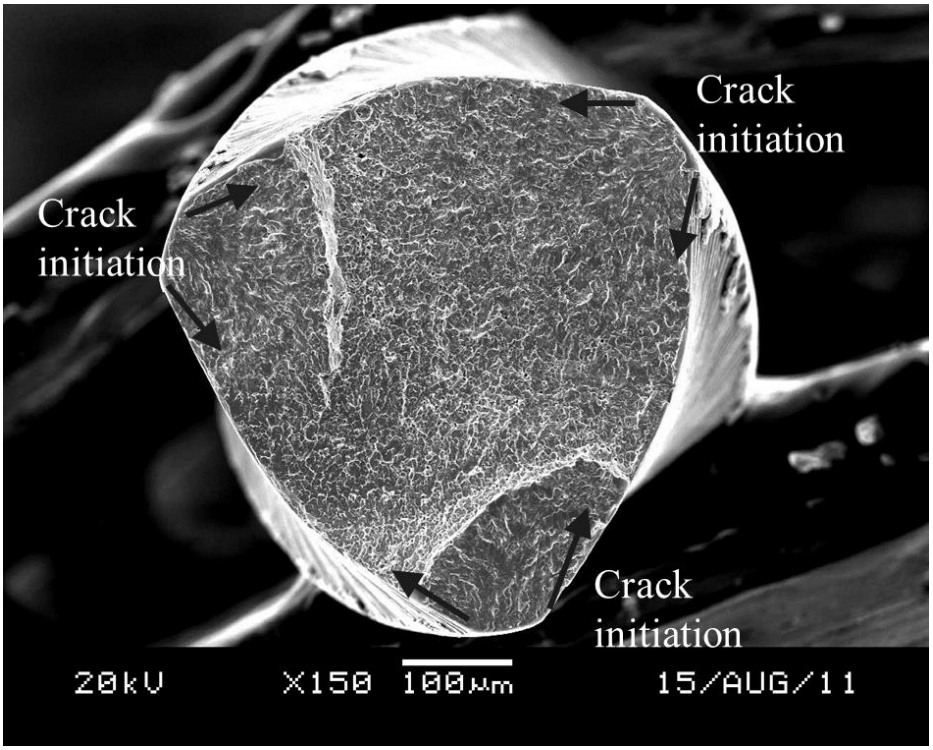

Fig.4-15. SEM photo of R7.5A40°(As-Received) reciprocating movement fracture surface.

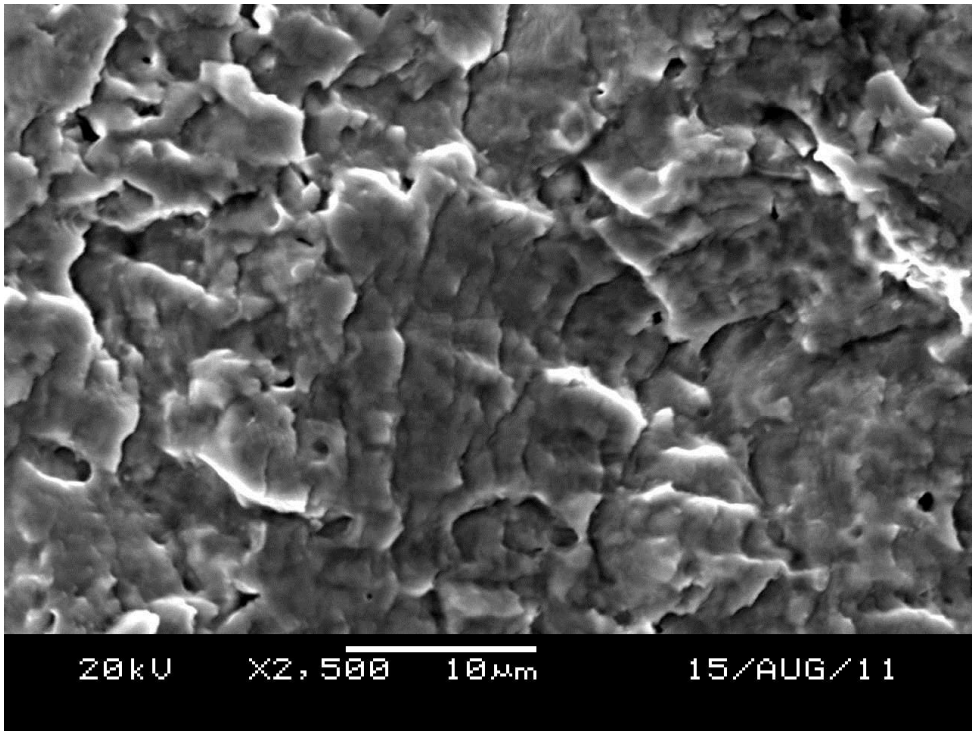

Fig.4-16. Striations in R7.5A40°(As-Received) normal rotation fracture surface.

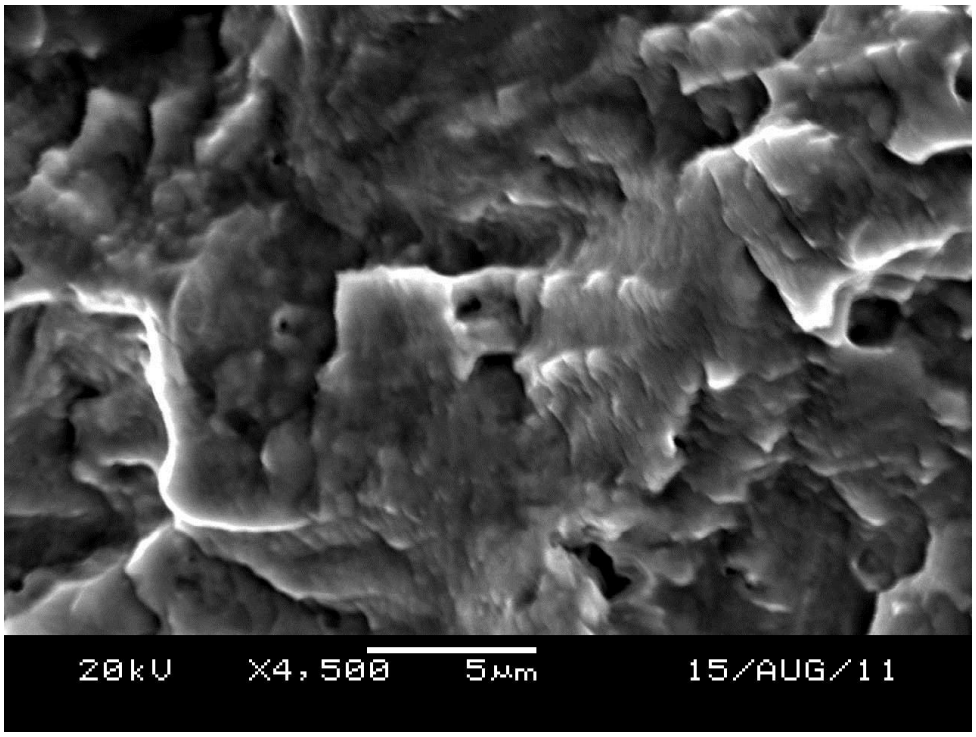

Fig.4-17. Striations in R7.5A40° (As-Received) reciprocating movement fracture surface.

Table 4-2.Comparison between striations and fatigue life in two kinds of rotation.

R7.5A40° (As-Received)	Normal rotation	Reciprocating method ($\theta = 45°$, $\alpha = 7°$)
Striation numbers	544	1032

Fatigue life	1401	5161
Difference	857	4129

4.4 ANOVA analysis for fatigue testing data

To identify whether progressive reciprocating motion (PR) improve the fatigue better than those in continuous rotating motion (CR), one way ANOVA has been applied for checking the significance (See appendix 10). Moreover, since there were four HT parameters in our test, Bonferroni post hoc tests at $p<0.05$ was also employed to understand the impact difference between HTs under same strain condition. One thing worth to mention is to check the homogeneity of variance first before comparing different group of HTs (see appendix 9). If the HT groups belong to non-homogeneity, the post hoc test Games-Howell at $p<0.05$ should be applied, the other cases can defined by post hoc test Bonferroni at $p<0.05$.

All conditions showed a statistically significant difference between CR and PR with $p<0.001$. It can be interpreted as the fact that we reduced the strain amplitude thus improving the fatigue life. HT increased fatigue life in CR motion by ~10% (in CT under R50θ60) to 413% (in HT600 under R7.50θ60) over that in the CR. All HTs were found statistically significant longer lives than the file as received ($p<0.001$) except CT. CT only prolongs fatigue life when instruments subjected to small strain ε=3.18% ($p<0.05$). Under small strain conditions (ε=3.18% and 3.44%), fatigue life enhancement of HT400is larger than those in HT600. When larger strain conditions (ε=3.8% and 4.25%) is applied, situation is the opposite. The life under HT400+HT600 lay between that for the HT400 and HT600 except for the largest strain ε=4.25%.

For PR motion, all HTs in small strain ε=3.18% were found significantly longer lives than as received file ($p<0.001$). CT follows the pattern in CR motion. The life under HT400+HT600 lay between that for the HT400 and HT600 when subjected to relatively low strains (ε=3.18% and 3.44%). The larger strains (ε=3.8% and 4.25%) help the life in HT400+HT600 even higher than in HT600 under same condition ($p<0.05$).

4.5 Cutting efficiency in reciprocating movement

As mentioned in Section 4.3, the fatigue life performance arranged according to amount is: HT600 ≈HT400+HT600> HT400 > CT > As-Received. Therefore, we selected six combinations as our interesting parameters of cutting efficiency: As-Received, HT400, HT600, HT400+CT, HT600+CT and HT400+HT600. Fig.4-18 shows the cutting efficiency results under various heat treatments in different positions. The detail data is listed in Table 4-3 to Table 4-8.

For the endodontic file As-Received, the average one minute cutting amount in different positions is: 0.615mg in position1, 1.02mg in position2, 1.47mg in position3 and 2.295mg in position4. The above data shows that cutting amount is gradually increases from position1 to position4. At position 4, the amount is even 3 times as position1. By observing cutting amount in different cycles (from No.1 to No.5) in Table 4-3, we can find that the wearing problem is not serious in this condition.

For the endodontic file with HT400 treatment, the average one minute cutting amount in different positions is: 0.585mg in position1, 0.945mg in position2, 1.38mg in position3 and 2.19mg in position4. The above data shows that cutting amount is gradually increases from position1 to position4. By comparing above data with the file As-Received in different positions, we find all of them more or less smaller than the As-Received condition: -4.8% in position1, -7.4% in position2, -6.1% in position3 and -4.6% in position4. These may correlated with the fact that HT400 is almost martensite phase in the room temperature.

However, we keep conservative attitude about this data, since it's still relatively small compared with HT600 condition we will soon introduced.

For the endodontic file with HT600 treatment, the average one minute cutting amount in different positions is: 0.435mg in position1, 0.72mg in position2, 1.065mg in position3 and 1.635mg in position4. The above data shows that cutting amount is gradually increases from position1 to position4. By comparing above data with the file As-Received in different positions, we find all of them significantly smaller than the As-Received condition: -29.2% in position1, -29.4% in position2, -27.6% in position3 and -28.8% in position4. This phenomenon can be explained by the hardness change due to recrystallization. Since the effect of recrystallization is to decrease the number of dislocations in the material, thus decreasing the material hardness.

For the endodontic file with HT400+CT treatment, the average one minute cutting amount in different positions is: 0.585mg in position1, 0.975mg in position2, 1.425mg in position3 and 2.25mg in position4. By comparing above data with the HT400 file in different positions, we find all of them slightly larger than the HT400 condition: +0% in position1, +3.2% in position2, +3.3% in position3 and +2.7% in position4. Although, the effect of HT400 decreases the cutting efficiency around 4%, we can still use CT treatment to compensate back around 3%. Furthermore, the phase structure in HT400 is already in martensite. At this moment, if we assume the total amount of transformable martensite is limited, even we use CT, whose function is to make the residual austenite transformed into martensite, the martensite growth amount is also limited. Therefore, the effect of CT on HT400 is small.

For the endodontic file with HT600+CT treatment, the average one minute cutting amount in different positions is: 0.465mg in position1, 0.765mg in position2, 1.26mg in position3 and 2.04mg in position4. By comparing above data with the HT600 file in different positions, we find all of them significantly larger than the HT600 condition: +6.9% in position1, +9% in position2, +18.3% in position3 and +24.8% in position4. This huge difference may be related to the fact that CT is used for improving durability as we mentioned in Section 3.3.2.

As for the parameter HT400+HT600, the average cutting amount is coincides with our expectation, the amount is generally higher than HT600 but lower than HT400. The one minute cutting amount in different positions is: 0.42mg in position1, 0.69mg in position2, 1.065mg in position3 and 1.59mg in position4.

4.5.1 ANOVA analysis for cutting efficiency results

The cutting efficiency in all positions were put into both post hoc Bonferroni and Games-Howell test, the results is shown in appendix 12. The significant difference can be seen from each positions ($p<0.01$) in both post hoc tests. It implies that to evaluate accurate cutting efficiency, the most important thing is to identify the cutting region first.

For the effect of HT compared with the file as received (see appendix 13) HT600+CT showed a clear statistically significant difference with as received one ($p<0.001$); however, the situation is the opposite in HT400 and HT400+CT. This may be interpreted as the fact that the purpose of HT400 is to transform the residual austenite to martenite. If the instrument is operated at the temperature, which contents is almost austenite (see DSC test of as received and HT400), the residual austenite can be transformed into martensite is very limited, thus the cutting efficiency won't decrease too much. The same logic of DSC results can be applied in HT600 and HT600+CT. In HT600, two phases co-exist when instrument is operated at room temperature. The more martensite phase is produced, the lower cutting efficiency can be found. The pattern of HT effect fits in all positions.

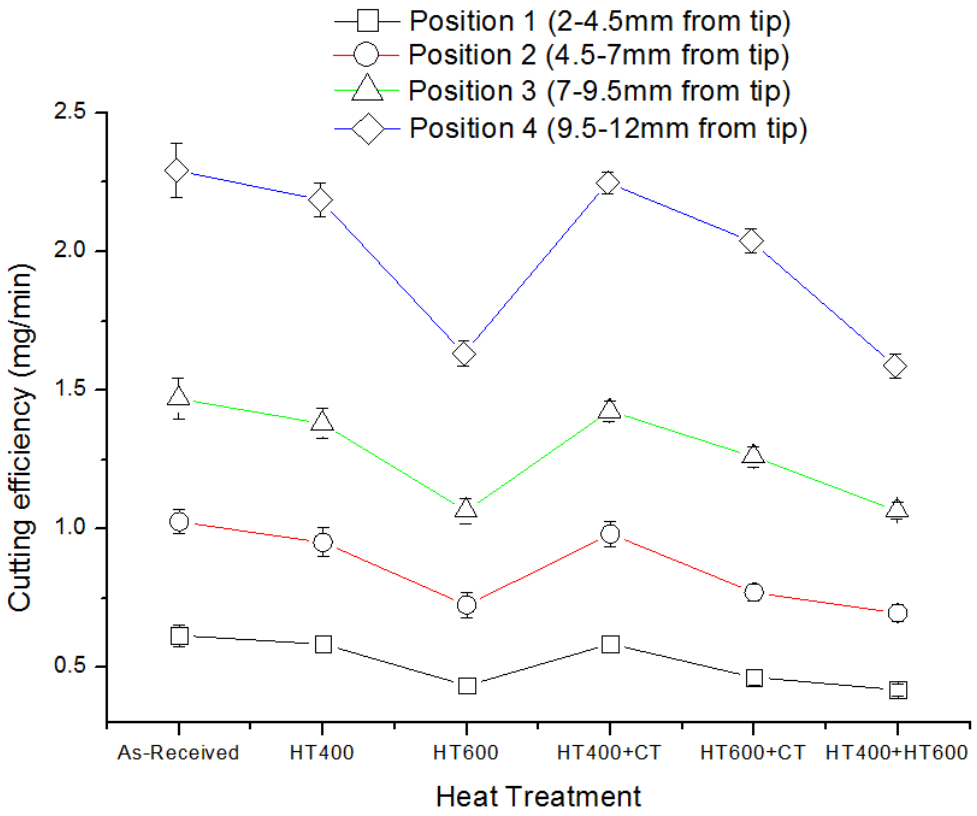

Fig.4-18.Cutting efficiency with different heat treatments in different position.

Table 4-3.As-Received cutting amount in 40 seconds at different positions.

As-Received	No.1 AV of 3 cycles(mg)	No.2 AV of 3 cycles(mg)	No.3 AV of 3 cycles(mg)	No.4 AV of 3 cycles(mg)	No.5 AV of 3 cycles(mg)	AV (mg)
Position.1-Left	0.19	0.21	0.21	0.20	0.22	0.21
Position.1-Right	0.20	0.23	0.20	0.20	0.21	0.21
Position.2-Left	0.32	0.34	0.36	0.34	0.36	0.34
Position.2-Right	0.33	0.32	0.35	0.33	0.33	0.33
Position.3-Left	0.49	0.47	0.50	0.53	0.52	0.50
Position.3-Right	0.42	0.50	0.45	0.51	0.50	0.48
Position.4-Left	0.75	0.81	0.83	0.75	0.77	0.78
Position.4-Right	0.79	0.75	0.72	0.72	0.76	0.75

Table 4-4. HT400 cutting amount in 40 seconds at different positions.

HT400	No.1 AV of 3 cycles(mg)	No.2 AV of 3 cycles(mg)	No.3 AV of 3 cycles(mg)	No.4 AV of 3 cycles(mg)	No.5 AV of 3 cycles(mg)	AV (mg)
Position.1-Left	0.18	0.20	0.20	0.19	0.21	0.20
Position.1-Right	0.20	0.19	0.19	0.18	0.19	0.19
Position.2-Left	0.30	0.30	0.33	0.32	0.30	0.31
Position.2-Right	0.31	0.29	0.32	0.31	0.35	0.32
Position.3-Left	0.45	0.51	0.47	0.43	0.48	0.47
Position.3-Right	0.43	0.46	0.45	0.41	0.49	0.45
Position.4-Left	0.72	0.76	0.74	0.73	0.73	0.74
Position.4-Right	0.71	0.75	0.74	0.72	0.71	0.73

Table 4-5. HT600 cutting amount in 40 seconds at different positions.

HT600	No.1 AV of 3 cycles(mg)	No.2 AV of 3 cycles(mg)	No.3 AV of 3 cycles(mg)	No.4 AV of 3 cycles(mg)	No.5 AV of 3 cycles(mg)	AV (mg)
Position.1-Left	0.13	0.16	0.15	0.15	0.15	0.15
Position.1-Right	0.14	0.15	0.14	0.13	0.14	0.14
Position.2-Left	0.23	0.23	0.25	0.24	0.26	0.24
Position.2-Right	0.23	0.21	0.22	0.24	0.26	0.23
Position.3-Left	0.35	0.37	0.36	0.35	0.38	0.36
Position.3-Right	0.35	0.36	0.34	0.33	0.37	0.35
Position.4-Left	0.55	0.55	0.52	0.55	0.57	0.55
Position.4-Right	0.54	0.55	0.53	0.54	0.54	0.54

Table 4-6. HT400+CT cutting amount in 40 seconds at different positions.

HT400+CT	No.1 AV of 3 cycles(mg)	No.2 AV of 3 cycles(mg)	No.3 AV of 3 cycles(mg)	No.4 AV of 3 cycles(mg)	No.5 AV of 3 cycles(mg)	AV (mg)
Position.1-Left	0.19	0.19	0.19	0.19	0.21	0.19
Position.1-Right	0.19	0.20	0.20	0.18	0.20	0.19
Position.2-Left	0.32	0.31	0.34	0.32	0.34	0.32
Position.2-Right	0.31	0.31	0.34	0.32	0.33	0.32
Position.3-Left	0.46	0.50	0.48	0.45	0.50	0.48
Position.3-Right	0.46	0.50	0.49	0.44	0.49	0.47
Position.4-Left	0.77	0.75	0.75	0.74	0.74	0.75
Position.4-Right	0.76	0.75	0.76	0.74	0.74	0.75

Table 4-7. HT600+CT cutting amount in 40 seconds at different positions.

HT600+CT	No.1 AV of 3 cycles(mg)	No.2 AV of 3 cycles(mg)	No.3 AV of 3 cycles(mg)	No.4 AV of 3 cycles(mg)	No.5 AV of 3 cycles(mg)	AV (mg)
Position.1-Left	0.17	0.15	0.16	0.15	0.15	0.16
Position.1-Right	0.16	0.15	0.15	0.14	0.15	0.15
Position.2-Left	0.28	0.25	0.25	0.25	0.26	0.26
Position.2-Right	0.28	0.25	0.25	0.25	0.24	0.25
Position.3-Left	0.42	0.43	0.41	0.40	0.44	0.42
Position.3-Right	0.42	0.43	0.43	0.40	0.42	0.42
Position.4-Left	0.66	0.68	0.70	0.67	0.69	0.68
Position.4-Right	0.68	0.68	0.69	0.66	0.68	0.68

Table 4-8. HT400+HT600 cutting amount in 40 seconds at different positions.

HT400+HT600	No.1 AV of 3 cycles(mg)	No.2 AV of 3 cycles(mg)	No.3 AV of 3 cycles(mg)	No.4 AV of 3 cycles(mg)	No.5 AV of 3 cycles(mg)	AV (mg)
Position.1-Left	0.12	0.15	0.16	0.15	0.15	0.14
Position.1-Right	0.13	0.14	0.13	0.16	0.14	0.14
Position.2-Left	0.23	0.23	0.22	0.26	0.25	0.24
Position.2-Right	0.23	0.21	0.22	0.25	0.23	0.23
Position.3-Left	0.35	0.37	0.35	0.36	0.37	0.36
Position.3-Right	0.35	0.36	0.35	0.36	0.34	0.35
Position.4-Left	0.54	0.52	0.53	0.55	0.53	0.53
Position.4-Right	0.53	0.51	0.53	0.55	0.52	0.53

4.6 Optimal parameters for clinical therapy

One way ANOVA and post hoc Berforonni(for homogeneous variance) and Games-Howell (for nonhomogeneous variance) test at p=0.05 with a statistical analysis software (SPSS 20, IBM, NY, USA) has been used to check for the significance of fatigue life difference under different heat treatments. The related results are shown in Appendix 9-11.

As discussed in Section 4.2 to Section 4.5, we can derive the S-N formula from Chapter 2 andFig.4-12. For ProTaper F2 in traditional rotation:

$$\varepsilon N^{0.282} = 0.244 \quad \text{(As-Received)} \tag{3.1}$$

$$\varepsilon N^{0.260} = 0.261 \quad \text{(HT400)} \tag{3.2}$$

$$\varepsilon N^{0.331} = 0.524 \quad \text{(HT600)} \tag{3.3}$$

$$\varepsilon N^{0.385} = 0.870 \quad \text{(HT600+HT400)} \tag{3.4}$$

$$\varepsilon N^{0.247} = 0.202 \quad \text{(CT)} \tag{3.5}$$

For ProTaper F2 in reciprocating movement:

$$\varepsilon N^{0.232} = 0.235 \quad \text{(As-Received)} \tag{3.6}$$

$$\varepsilon N^{0.171} = 0.163 \quad \text{(HT400)} \tag{3.7}$$

$$\varepsilon N^{0.262} = 0.510 \quad \text{(HT600)} \tag{3.8}$$

$$\varepsilon N^{0.207} = 0.293 \quad \text{(HT600+HT400)} \tag{3.9}$$

$$\varepsilon N^{0.194} = 0.183 \quad \text{(CT)} \tag{3.10}$$

From above equations, we concluded that the fatigue life arranged according to amount is roughly: HT400+HT600 ≈ HT600 > HT400 > CT > As-Received, where HT600 is better than HT400+HT600 when reciprocating movement applied and HT400+HT600 is better than HT600 when traditional rotation applied. However, in most cases, HT600 and HT400+HT600have the worst cutting efficiency.

In clinical therapy, time is money. How to quickly remove the diseased tissue from the canal without taking the risk of fatigue is the most important issue. Therefore, the optimal parameter should be based on the cutting efficiency perspective. Fig.4-19 shows the effect of heat treatment on cutting efficiency with reciprocating movement. Obviously, HT400+CT has the best selection in cutting efficiency perspective. Furthermore, as discussed in Section 4.3, HT400 has 34% to 154% and CT has 9% to 59% enhancement of fatigue life in reciprocating movement. It is expected that with these two heat treatments, we can have the good mechanical properties to avoid the unexpected fracture in clinical therapy.

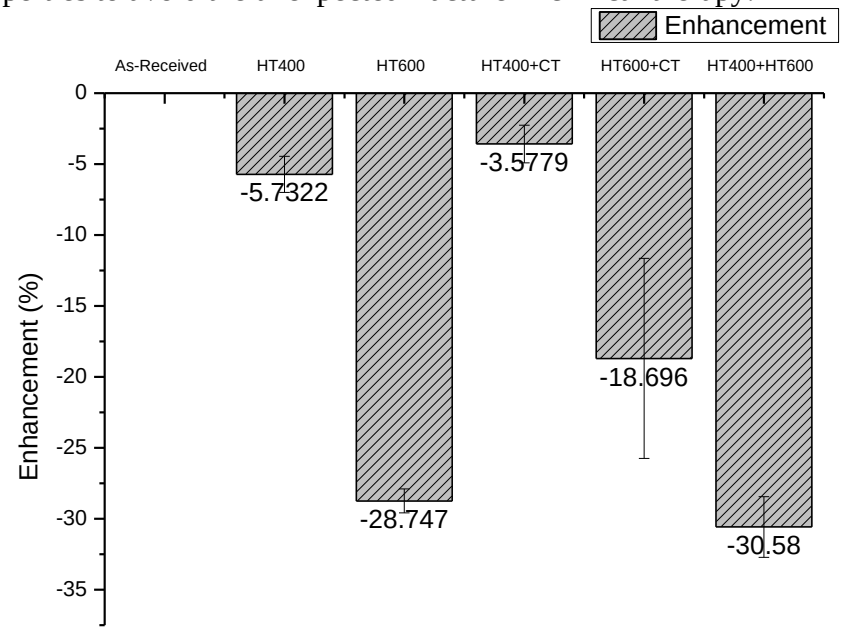

Fig.4-19.Effect of heat treatment on cutting efficiency with reciprocating movement.

4.7 Fatigue crack monitoring system

Fiber optic sensors, particularly FBGs have become increasingly popular in the last decade due to their wide dynamic range, immunity to electromagnetic interference and their multiplexing capability. FBG sensors, inscribed on an optic fiber of 125 μm in diameter, can be made as short as 2 to 5 mm in length and have been used recently in localized strain measurements. An example is in the sensing polymeric composite fatigue damage that was not accessible to conventional strain gauges [104].

Despite the success of FBGs in strain sensing and structural health monitoring, there are few reports on their applications in clinical endodontic use. It is not practical to attach the FBG on

the rotary instrument itself. The closet to the instrument one can get to is the handpiece. However, when an FBG fiber is bonded to the handpiece, the strain waves from the rotating Ni-Ti instrument can only be monitored indirectly. Therefore, during experimental fatigue test, enhancing the sensitivity of the system is our first priority and the system setup has been showed in Section 3.6.

4.7.1 Ability to detect rotary operation

Fig.4-20 shows the waveform picked up by the FBG with time elapsed. The instrument has not started rotating during first part (up to about 11.046 sec) of the waveform. The received signal mainly consists of high frequency noises. As rotation started, the intensity of the received signal increased and a low frequency component become dominating. Judging from the waveform signal changes in the time domain clearly leads one to differentiate whether the instrument is operating or not. This result inspired us to analyze the events during operation time by Fast Fourier Transform (FFT).

In real time monitoring, the corresponding power variation was recorded by LabView with 22,000Hz sample rate. The pick-up signals were preliminarily tested at no operation time to confirm that the high frequency noise caused by environment is roughly above 5,000Hz. Thus we used a low pass filter to cut the frequency greater than 11,000Hz and proceed with FFT analysis in increment of every 100,000 data to get the characteristic frequencies at each. There're four potentially informative frequency sections will be discussed in Section 4.7.3.

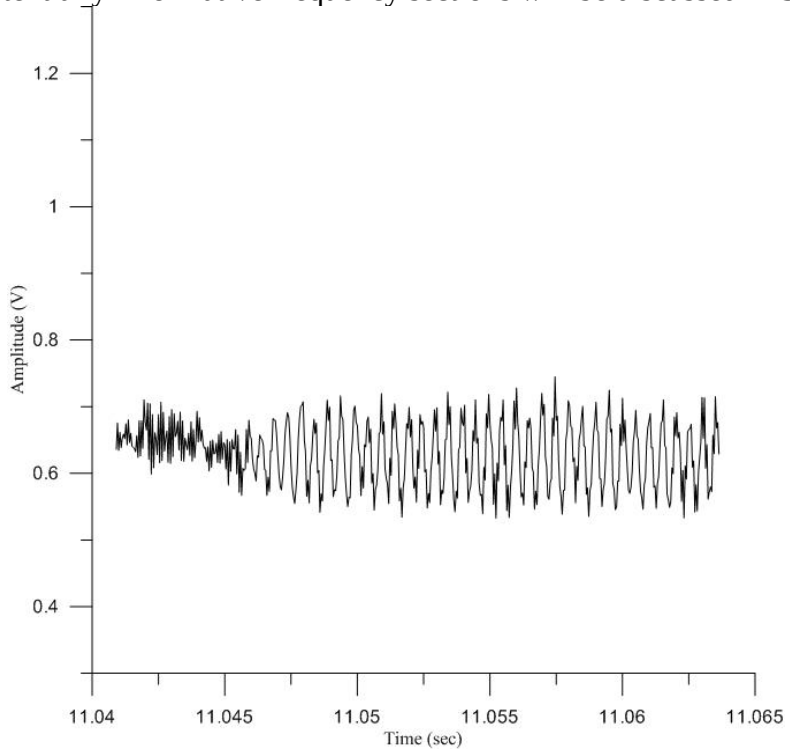

Fig.4-20.Typical difference between noise and normal operation time.

4.7.2 Comparison of FBG set-up direction

In the beginning, the sensors are set up in two mutually perpendicular directions, sticking to the metal jig by cyanoacrylate cement as shown in Fig.4-21. Fig.4-22shows the representative FFT signals captured by the FBG in the vertical and horizontal directions during the middle of the instrument life cycle. The noise in the vertical FBG signal is greater than horizontal one and the measured strain wave signal is also weaker. This phenomenon may be attributed to

the propagation direction of the stress wave in the jig. It implies that choosing the correct direction to acquire the stress wave signal is important for increasing our monitoring accuracy. Therefore, in the following, only the FBG along the horizontal direction has been employed.

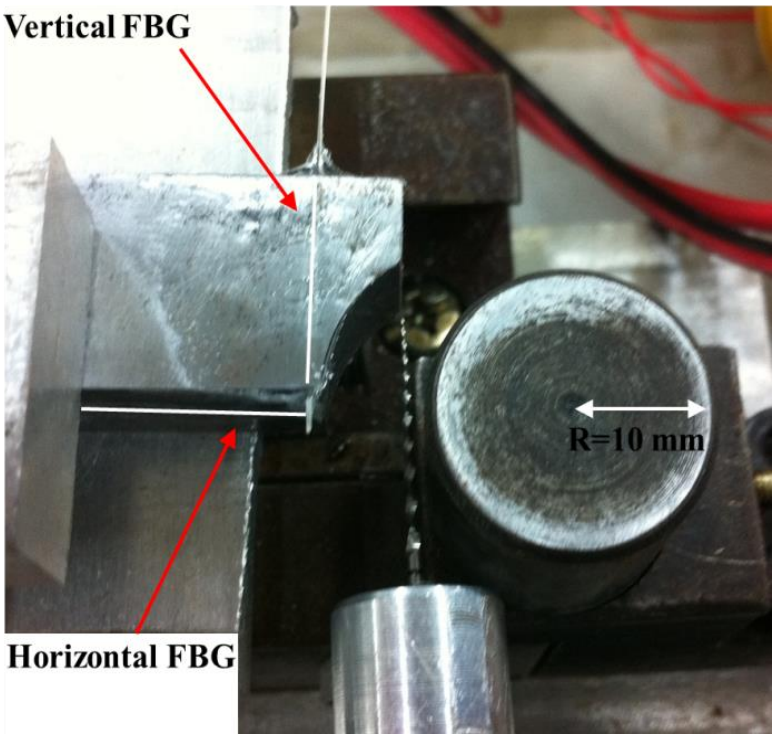

Fig.4-21.Two mutually perpendicular FBGs.

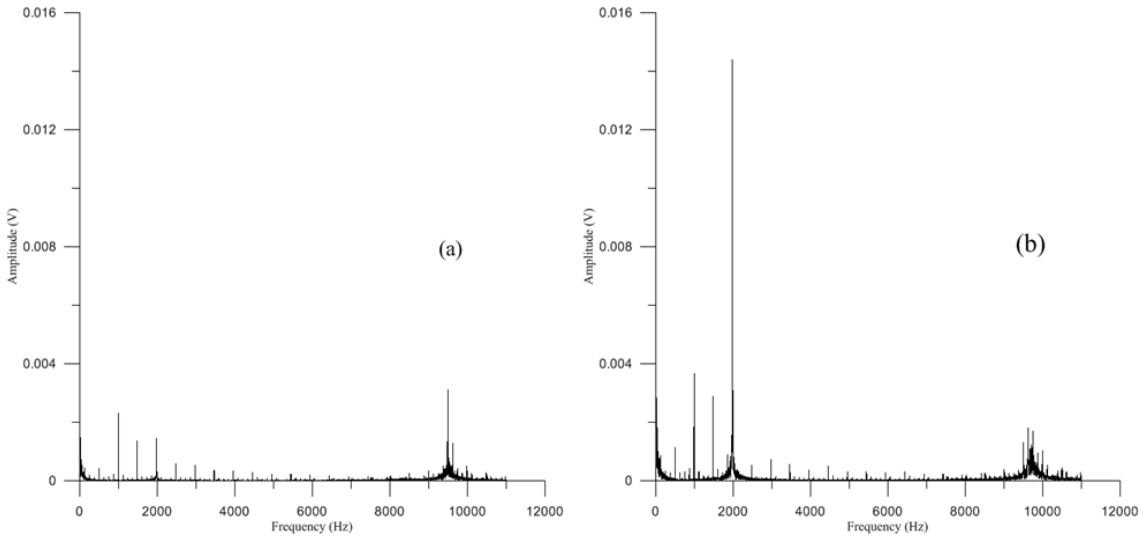

Fig.4-22.Characteristic FFT result detected by vertical (a) and horizontal (b) FBG sensor respectively.

4.7.3 Characteristic frequency analysis

Table 4-9 compares frequency shift and energy variation the four different sections: 20 to 40 Hz, 950 to 1000 Hz, 1450 to 1500 Hz and 1950 to 2000 Hz. The dominant frequency is defined by the intensity peak value in each of these sections. For instance, if the energy at 21.8Hz has the highest value from 20 to 40Hz region, we called it the dominant frequency in this section. Through this process, we can monitor the frequency shift and intensity variation

of the dominant frequency with time. The frequency variation in the 20 to 40 Hz section is the biggest and the second one is 1950 to 2000 Hz section. In fact, the Ni-Ti instrument rotating at 400 rpm has 3 blades and so will generate 3 strains bursts per revolution. This may account for the 20 Hz component. Variation of the frequency and intensity with time for a typical file are shown in Fig.4-23 to Fig.4-24. Fig.4-23 shows that in the 20 to 40Hz region, the frequency will fluctuate at first and then becomes stabilized at 20 Hz. Then at some point of time before fracture, the frequency will shifts towards the 40 Hz again. This may be attributed to the fact that as a crack appears and develops, the tip of the file may engage in an out-of-plane whipping action, changing the number of contact instances with the canal wall. This is reflected as a change in intensity and a shift in frequencies of the original signals, giving rise to the measured patterns.

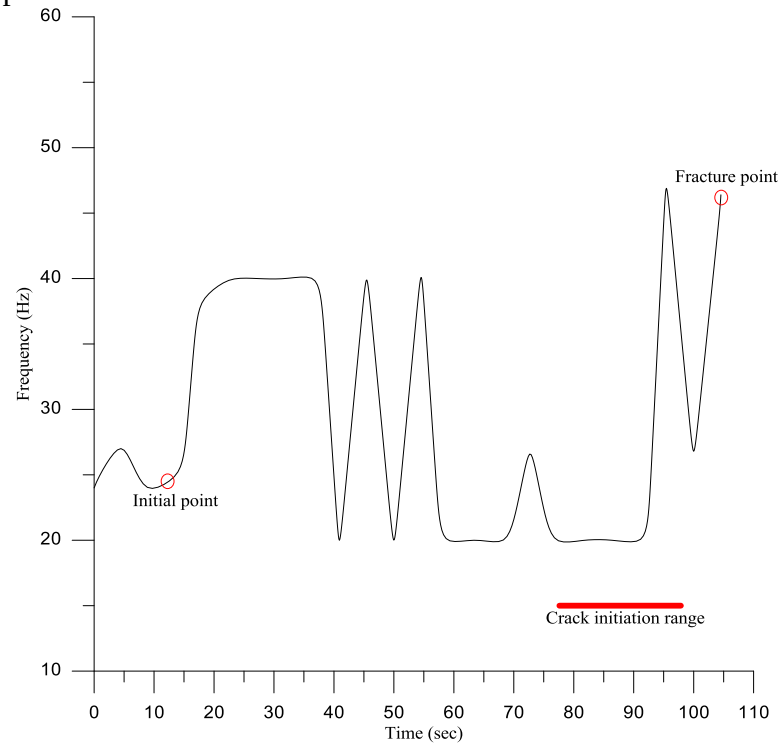

Fig.4-23.Typical ProTaper F2 frequency shifting phenomenon in 20 to 40 Hz section by time.

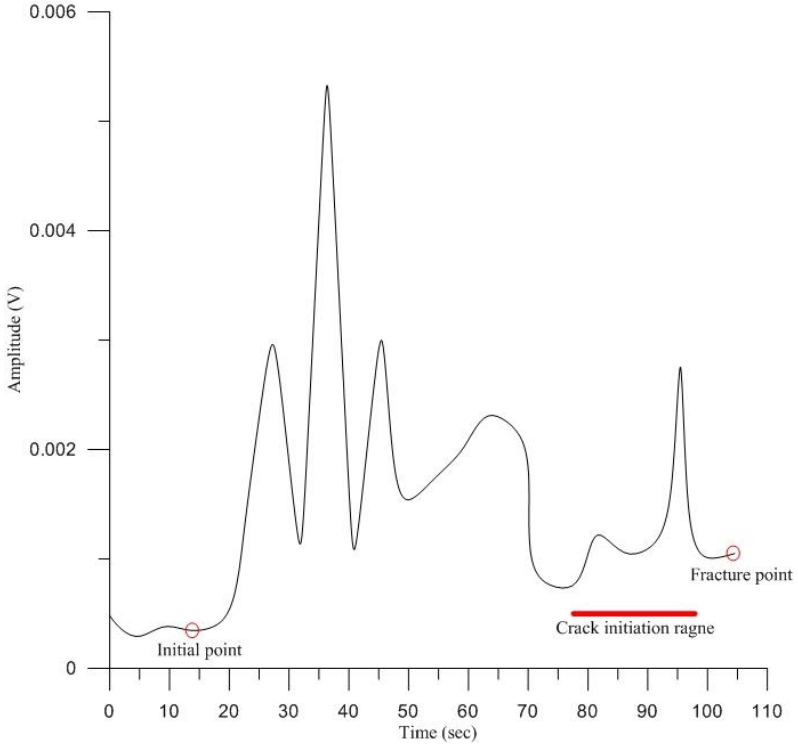

Fig.4-24.Typical ProTaper F2 energy variation phenomenon in 20 to 40 Hz section by time.

The intensity of the 20 to 40 Hz section increased at first. It fluctuated up and down and finally settled to a more or less stable value. This may be interpreted as the result of initial cutting and grinding followed by a worn. Then a marked peak occurred in the last portion of fatigue life (see Fig.4-24). During this period, a peculiarly audible sound also arose that is different from the sound before.

The above typical development in the intensity and frequency shift pattern was observed in 12 out of 13 instruments tested. The other three characteristic frequency sections have also shown the same phenomenon. However, there are two subtle differences between the 20 to 40 Hz signal and the other three characteristic frequencies: first, the change in intensity and frequency shift is much less eminent, as is listed in Table 4-9; second, only 6 out of the 13 instruments tested exhibited the above pattern in the other three frequency sections. The pattern development is more haphazard in the remaining 7 instruments. Therefore, for clinical therapy, we concluded that the 20 to 40 Hz signal is the most suited for integrity monitoring.

Table 4-9. Difference between the four frequency sections.

Types of Ni-Ti rotary instruments	ProTaper F2		Endowav #25	
	Energy variation (V)	**Frequency shifting (Hz)**	**Energy variation (V)**	**Frequency shifting (Hz)**
20 Hz to 40 Hz	$\pm 11.28\times10^{-4}$	±9.9384	$\pm 22.03\times10^{-4}$	±3.1578
950 Hz to 1000 Hz	$\pm 3.88\times10^{-4}$	±0.1866	$\pm 8.79\times10^{-4}$	±0.1870
1450 Hz to 1500 Hz	$\pm 3.31\times10^{-4}$	±0.2901	$\pm 7.14\times10^{-4}$	±0.2923
1950 Hz to 2000 Hz	$\pm 2.55\times10^{-4}$	±0.3778	$\pm 18.03\times10^{-4}$	±1.2704

4.7.4 Fractographic examination

Although we cannot identify the crack initiation time, SEM fractographic analysis can provided an estimation of the possible range of the crack propagation period. As mentioned in Section 1.2.5, a typical fractograph can be divided into 2 regions: (i) crack propagation region characterized by striations and (ii) the final fracture characterized by ductile dimples. Fig.4-25.b shows a magnified view of the region of striations, each of which corresponds to one loading cycle. By noting the extent of the striation area and counting the average striation density, one can estimate the duration of crack propagation. The above exercise carried out on a number of instrument fracture surfaces indicated that crack propagation occupied somewhere between 9% to 30% of the total rotational life prior to fracture. It should be noted that the scatter in the percentage of crack propagation life is both an inherent characteristic of fatigue surface and also a result of uncertainty in striation spacing measurement. The latter stems from the fact that the fracture surface is full of up and downs, each localized on Fig.4-23 and Fig.4-24 as a red bar. It is clear that the specific peak mentioned above fell within the crack propagation period. The peaks may be attributed to a change in the operating status from stable to unstable as the cracked file may flip in the random manner, creating more contact and grinding events. Thus the transition from stable intensity and frequency to unstable transient may be used as an indicator that cracks has arisen in the instruments.

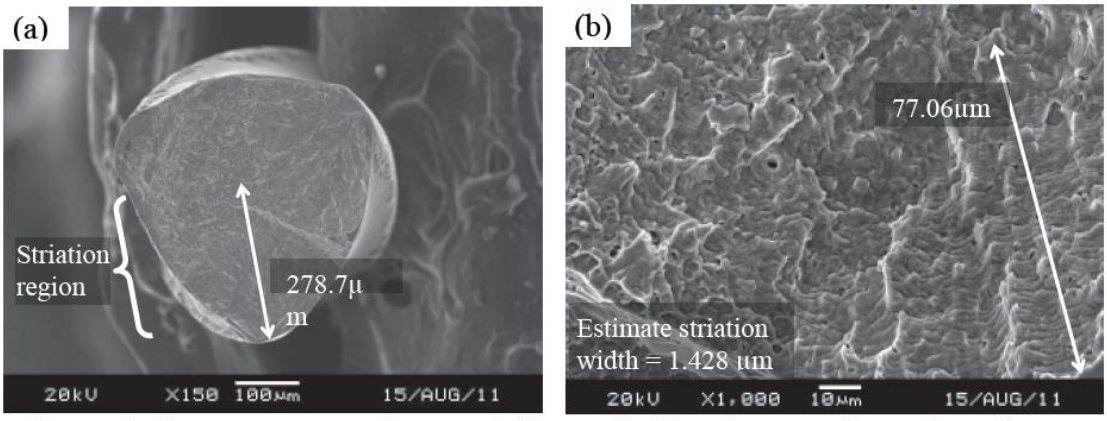

Fig.4-25. Typical ProTaper Fe SEM fractograph (a) overall; (b) crack propagation section with striations.

4.7.5 Criteria for clinical operation safety

For a real-time monitoring system, by only observing the intensity/frequency phenomenon is far from enough. In fact, the above patterns were all plotted after fatigue fracture happened. This inspired us to increase the time resolution of the data which is actually to increase the processing speed of FFT. Here, FFT was carried out incrementally, each time on a cluster of 22000 data (corresponding to 1.0 second) to plot more detail of the pattern at each instance. The criteria are using the 300% average of the first 3 seconds rotation data as a reference in intensity variation (plotted as a red horizontal line in the latter figures). For example, if we collected the initial 3 seconds data which has 3 corresponding energy variations (0.001 V, 0.002 V and 0.003 V), then, we use 0.006 V as a criterion reference in time domain. Fig.4-26 to Fig.4-29 shows the four ProTaper F2 files monitored by real-time system. The two vertical lines in each figures represents the starting time, fracture time respectively. In

these results, the 300% average of first 3 seconds data is obviously suitable for the warning criterion. The warning gives the dentists to have around 11 to 30 seconds reaction time, which is enough for stopping therapy. The time of alert peak is also coincides with the phenomenon of dominant frequency changes in frequency domain (marked as blue cross). We can see more or less that the dominant frequency changes from stable 20 Hz into several times higher frequencies in the region indicating the crack propagation Although, the fiber sensor is attached to the metal jig in the current experiment detecting signals indirectly, the signals still reveal some useful information can be seen as an indicator of the fracture warning. In clinical treatment, a logical place to install FBG sensors is on the handpiece that the dentists use to operate the rotary instrument. Therefore, more work has to be done to clarify whether a fiber sensor installed on a handpiece can give reliable instrument cracking indication.

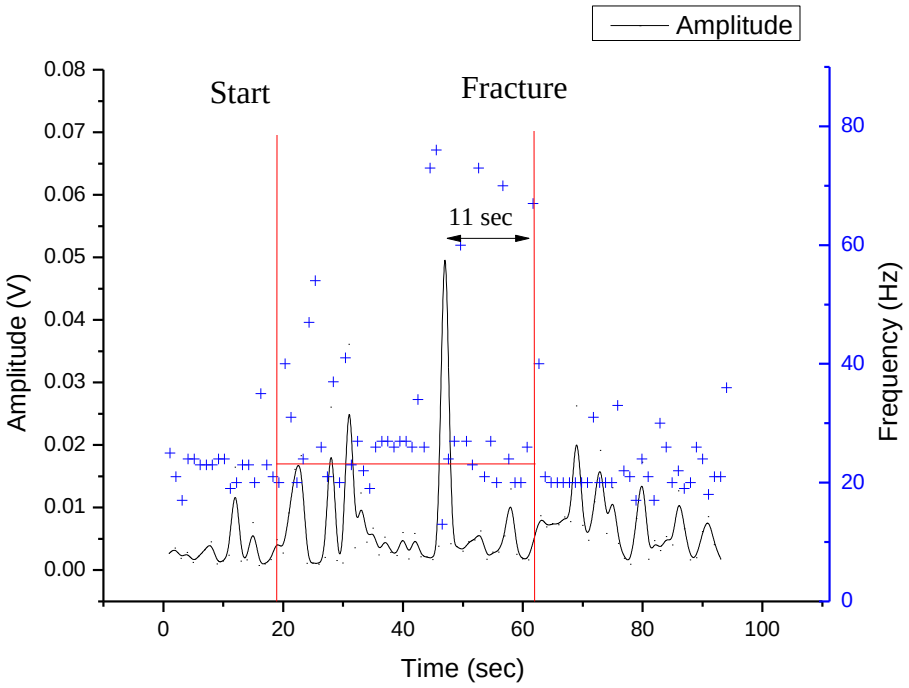

Fig.4-26. No.1 ProTaper F2 intensity and dominant frequency varies by time.

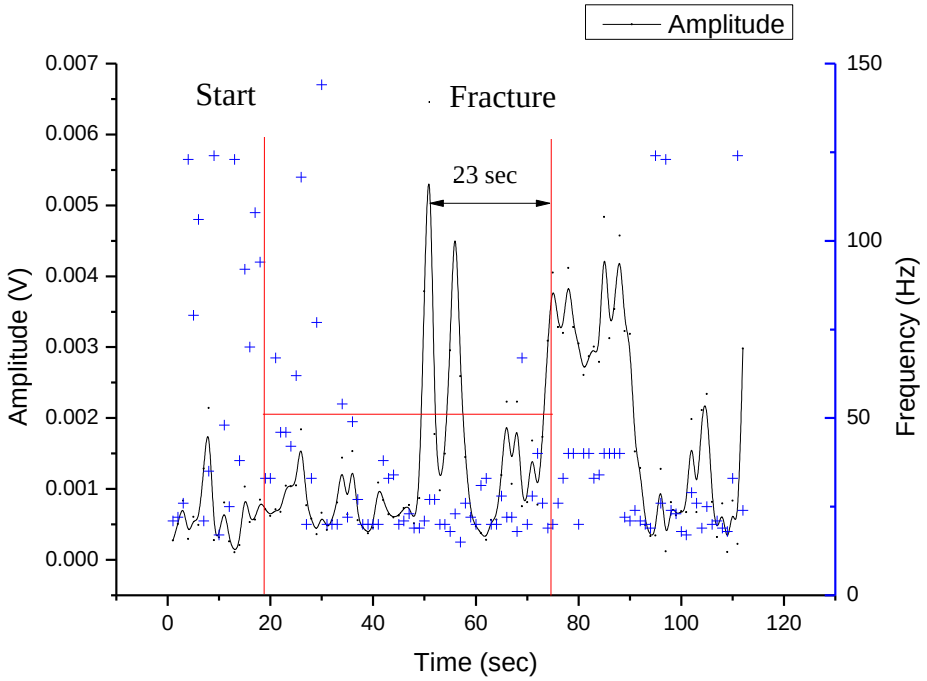

Fig.4-27. No.2 ProTaper F2 intensity and dominant frequency varies by time.

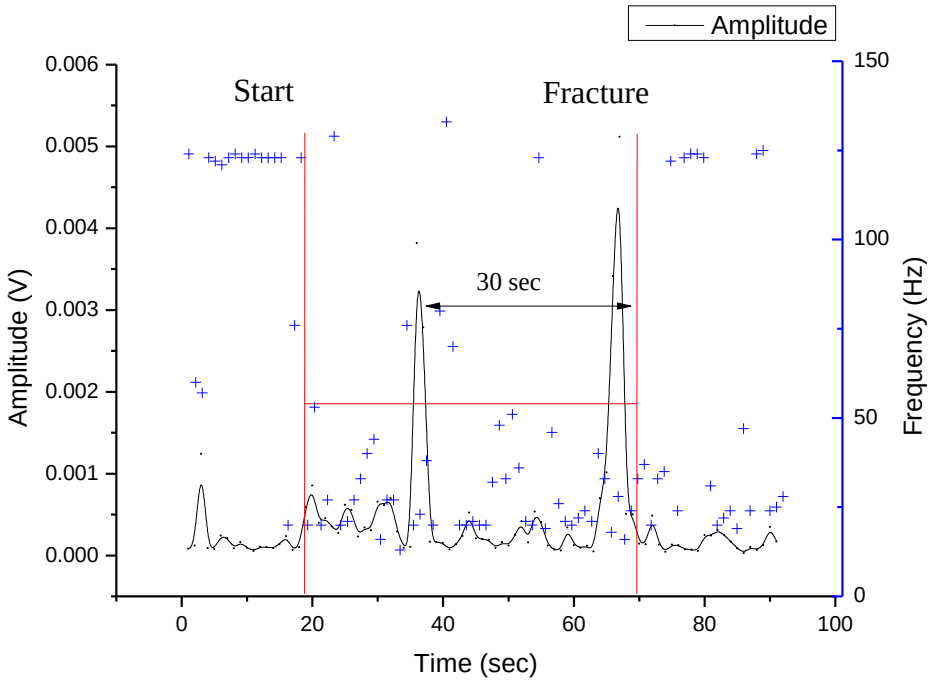

Fig.4-28. No.3 ProTaper F2 intensity and dominant frequency varies by time.

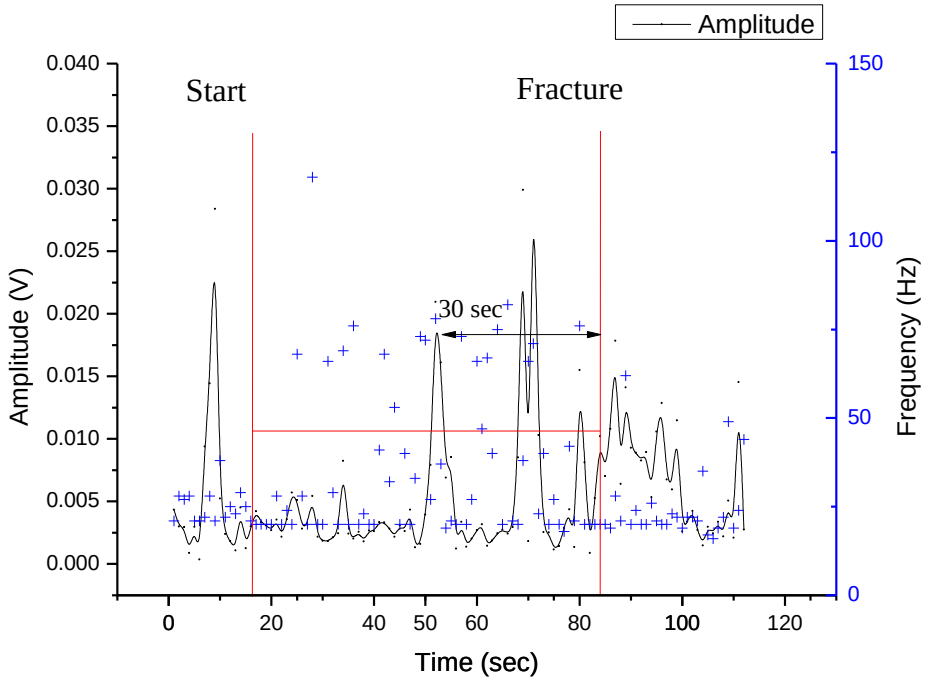

Fig.4-29. No.4 ProTaper F2 intensity and dominant frequency varies by time.

Chapter 5 Studies of large-fast TPP fabrication

In this chapter, we will discuss TPP fabrication in two parts. The first part describes the basic techniques needs to be solved in large-scale TPP manufacturing, including the simulation of voxel size, tilt correction, motor controlling, laser focusing, and laser compensation. The second part will displays the large structures we fabricated as well as to explore the feasibility of massive parallel beams fabrication and its results.

5.1 Large scale TPP fabrication problems

Unlike micron structures, as the fabrication range is becoming larger, the tilt correction and laser focusing is more serious. Thus it is necessary to solve the problem for enhancing the qualities of products.

5.1.1 Tilt correction and auto focusing problem

Tilt and collapse problem as well as laser focusing are the three main issues that affect the qualities of micron products as shown in Fig.5-1. Both lines were fabricated with 50ms exposure time. It is observed that bottom line is vaguer compared with the upper one. This is attributed to the fact that the substance is not horizontal and doesn't coincide with the fabrication plane. In addition, it is indicated that the upper line is fabricated so high above the substrate, resulting in some part of this line even collapsed. From the Fig.5-1, it is shown that the laser spot doesn't focus well on the substrate during whole fabrication process. Therefore, for correcting the fabrication plane and improving the precision of focus position, tile correction and autofocus should be applied.

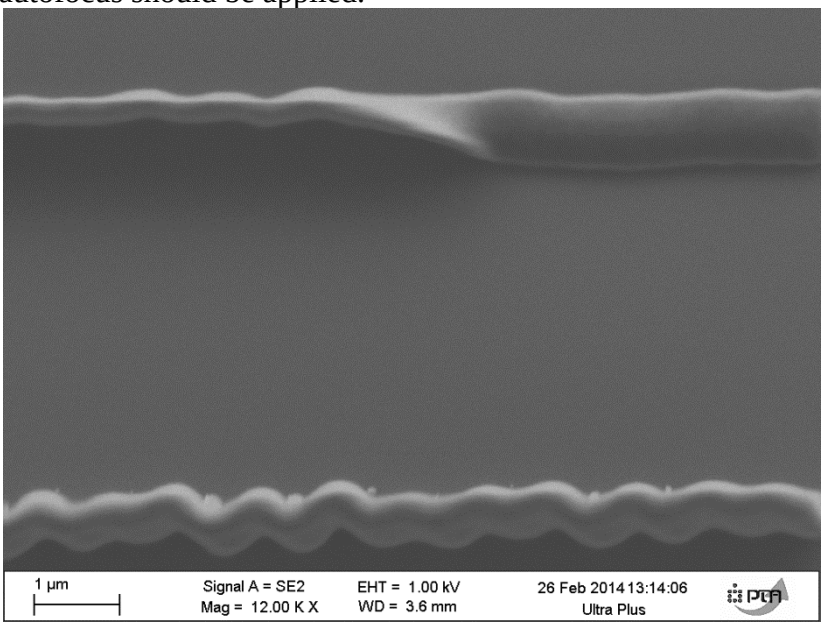

Fig.5-1. Tilt and collapse problem.

5.1.2 Autofocus

The main idea for getting the focus position is to analyze the captured C-MOS camera image, which is the reflection image of pixel from the interface between the coverslip and the resin. By comparing the pixel value with different z position until the maximum pixel value is

obtained, one can get the good laser focus. The method was developed in collaboration with Ya-Hsun Hsueh, who got her master degree at NTU in 2013.

In this study, a $200\times200\times200\mu m^3$ piezo stage mounted on the $120\times110mm^2$ ASI MS-2000 XY and a C-MOS camera are applied. The schematic setup is shown in Fig.5-2. The process of autofocus is shown in Fig.5-3. First capture the C-MOS camera image that is the laser reflection image and then analyzed pixel value of each pixel on the image. We use the average value of the four strongest pixels as the reference. For 8-bit gray scale image, the pixel value is corresponding to the brightness ranging from 0 to 255. It is taken to be from black to white and the values in between make up the different shades of gray.

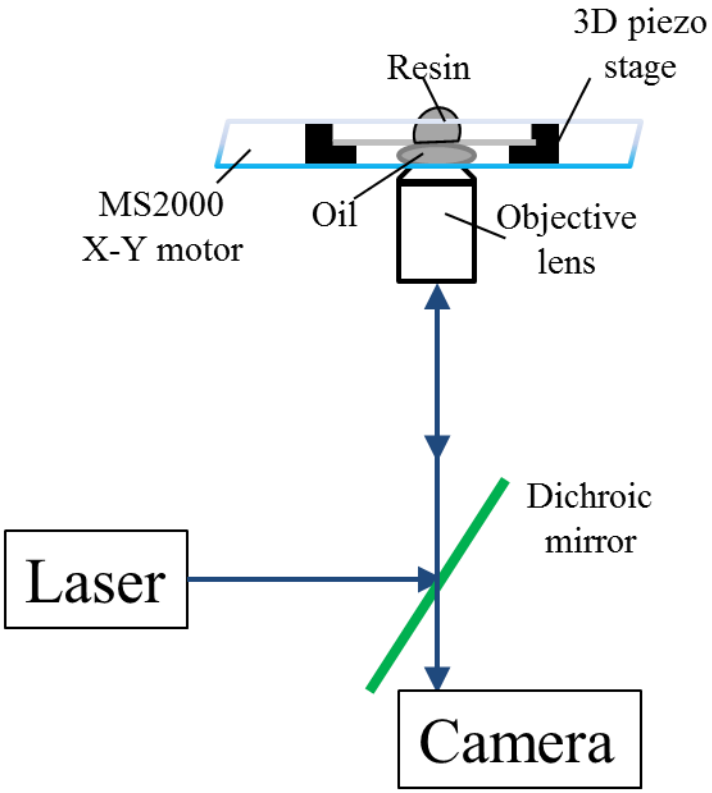

Fig.5-2.Schematic setup of autofocus.

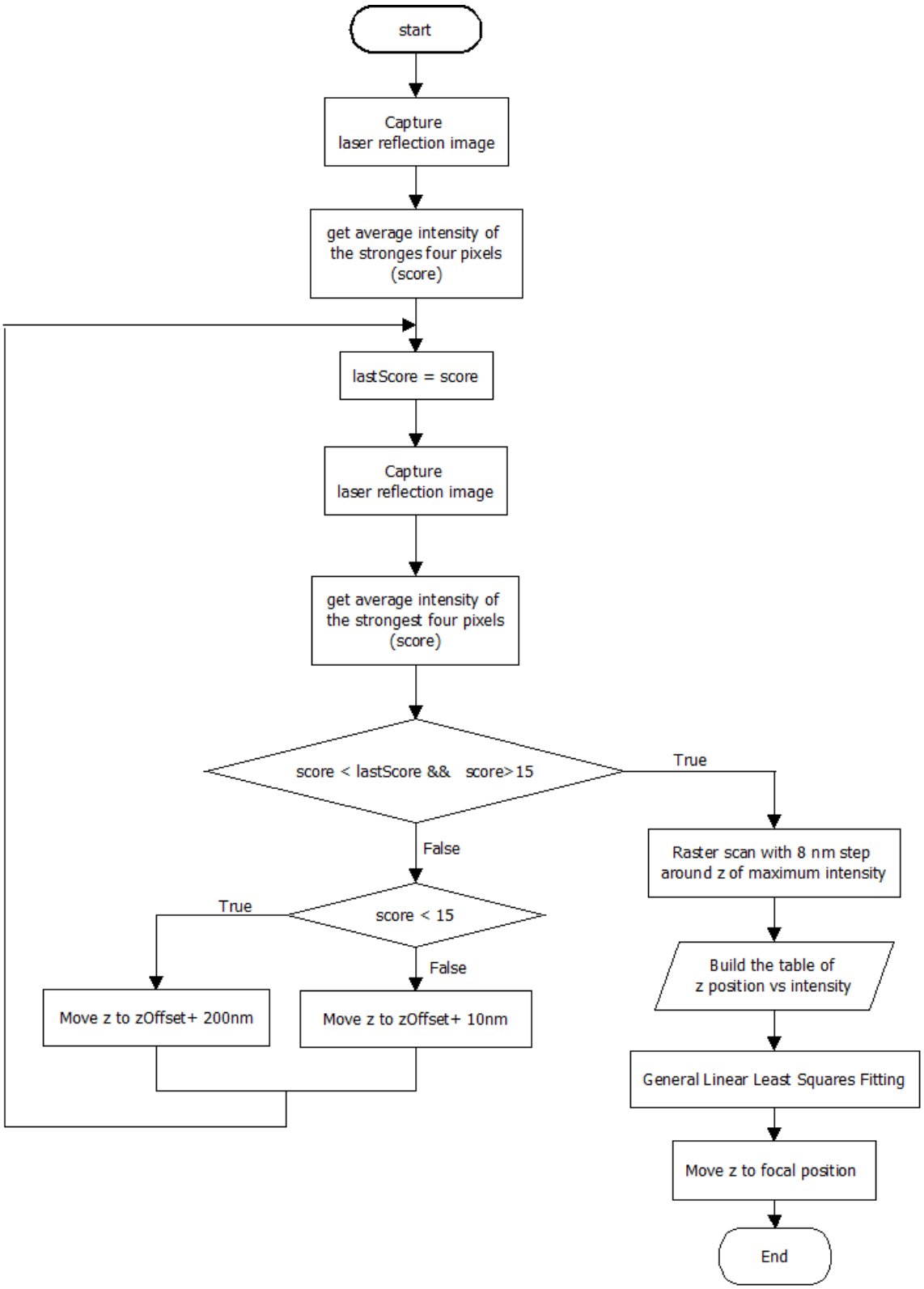

Fig.5-3.Flow chart of autofocus process.

Since the piezo stage can only move toward +z direction, the strategy for z scanning in order to find the strongest brightness is one-way scanning. Scanning starts from a specific offset z position which is manually set close to the real focus position in order to shorten the focusing time. To prevent polymerization in resin while focusing, the power we used for the focusing process is 0.175 mw, which is quite small compared with threshold voltage. After the scanning process starts, if the value is under 15 which is considered as background noise,

the z stage moves with the step 200 nm. Otherwise, if the value is over 15, which means we are getting closer to the focus position, the z stage moves with small step 10 nm. The loop will be ended until the maximum value obtained. The focal spot before and after applying focusing method is shown in Fig.5-4.

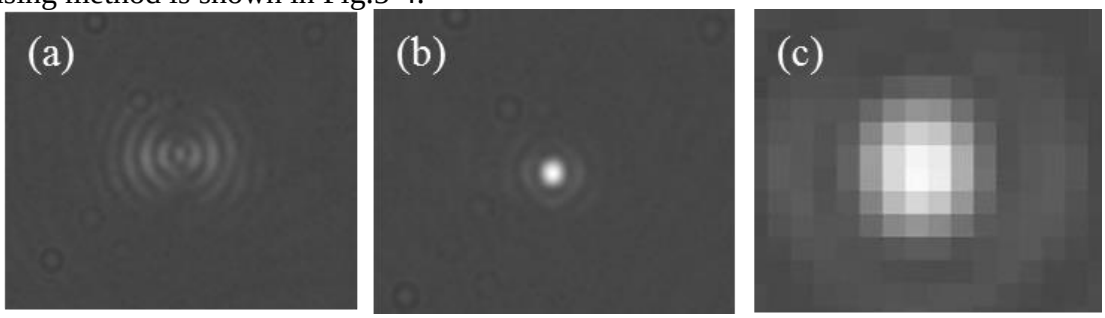

Fig.5-4. The focusing point: (a) before focusing at $z = 8\mu m$, (b) after focusing at $z = 9.22\mu m$, (c) Magnified focal spot.

5.1.3 Tilt correction

The substrate and the holder may not be perfect horizontal plane. The tilt correction is crucial for keeping the focal spot focusing properly on the coverslip during fabrication process. In general, the focused point in z is $200\mu m$ difference in 1 mm x-y plane square. This means we may face maximum $20\mu m$ difference in z while moving $100\mu m$ either in x or in y direction. It is sure that refocusing to the right position is needed. The strategy is to use three points on the coverslip as reference points to define the new coordinate system. The new coordinate system will then be taken into account in the CAD-based route design.

Unlike manual focusing, artificial error varies due to different operators and it is difficult to read the estimation value precisely. For improving the precision for focus measurement, it's better to apply autofocusing method at 3 points on the coverslip to have the basic idea of surface incline in the beginning.

The differences with and without using autofocus and tile correction can be observed from the grating as shown in Fig. 5-5.

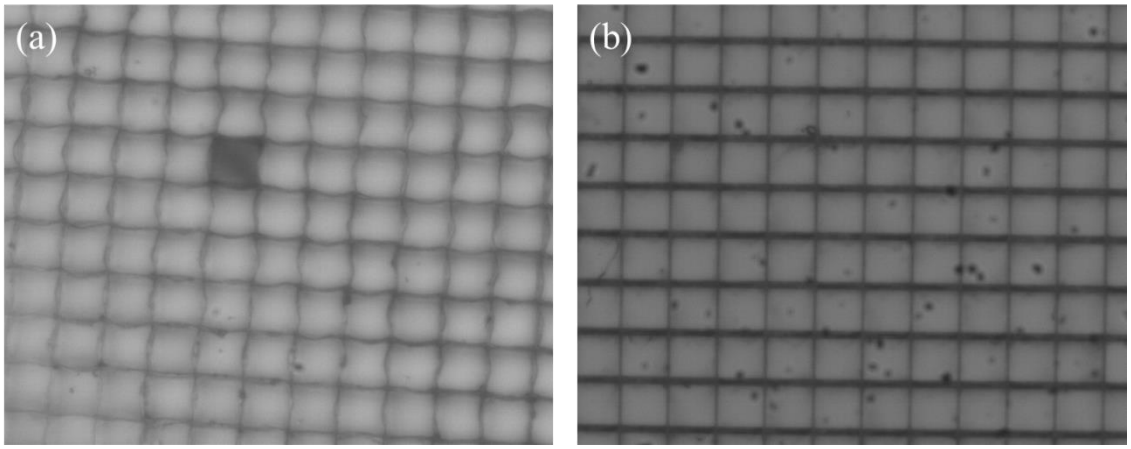

Fig.5-5. Grating with $3mm \times 3mm$ size and $150\mu m \times 150\mu m$ in each square: (a) without tilt correction and autofocusing, (b) with tilt correction and autofocusing.

5.1.4 Fabrication with motor stage for large step purpose

For achieving larger scale fabrication with size larger than 0.5 mm, it is very difficult to implement only with piezo stage. Commercial piezo stages are commonly with travel range less than $300\mu m$. Thus motor stage and high-resolution translation stage which is piezo motor-based direct drive is considered.

Unlike the high resolution products fabricated by piezo, the resolution of large structures manufactured by motor driven stages could be lower. For reducing the fabrication time in large scale structure, the strategy is to divide the fabrication contour into segments with basic geometry.

For two dimensional products, the key concept for fabrication is the moving time from one position to the next position should be the same for both x and y axes instead of the speed of both axes. The results of fabrication with same speed and same moving time for bith x and y axes are shown in Fig.5-6. It is fabricated in Photomer with Zeiss A-Plan objective of magnification 40, NA = 0.65. With the same moving time for both x and y axes in each segment, the velocity used is proportional to the distance in each axis. The experiments was done by assuming the acceleration and deceleration speed in both axes is same, For example, from point 1 to point 2, the motor is only moving in x axis for $1mm$ at velocity V_x. From point 2 to point 3, the motor should move $-0.5mm$, $+0.5\sqrt{3}mm$ in x, y axis respectively. To ensure the moving time is the same, V_y is then be adjusted as $\frac{1}{\sqrt{3}}V_x$ for the segment from point 2 to point 3. So far, the large biocompatible scaffold has been attempted by applying this concept and we will introduce it later.

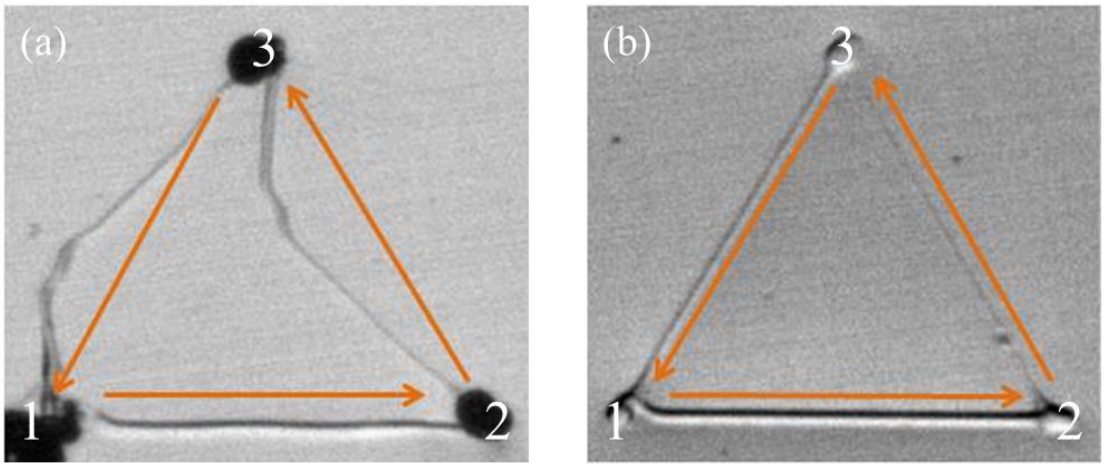

Fig.5-6.Fabrication of equilateral triangle with 1mm edge: (a) fabrication with same speed of x and y axes, (b) fabrication with same moving time of x and y axes.

5.1.5 Voxel simulation-linear and circular polarization

Voxels are the fundamental elements of TPP fabrication. The size and shape of the voxel is determined by the followings: Numerical Aperture (NA) of objective, fill factor of the Gaussian illumination beam (β_G), depth of focus and different polarization. Before starting the fabrication process, it is important to take into account which voxel size and shape is suitable for specific quality requirement. In this section, two kinds of resins had been investigated: Photomer with refractive index 1.538 and Ormocer with refractive index 1.496.

Fig.5-7 shows the simulation of Photomer in linear and circular polarization. The FWHMx and FWHMy is $0.260\mu m$ and $0.199\mu m$, thus the line width for fabrication x-dir line is smaller than for the y-dir one as shown in Fig.5-8. However, the FWHMx and FWHMy is the same ($0.226\mu m$) in circular polarization.

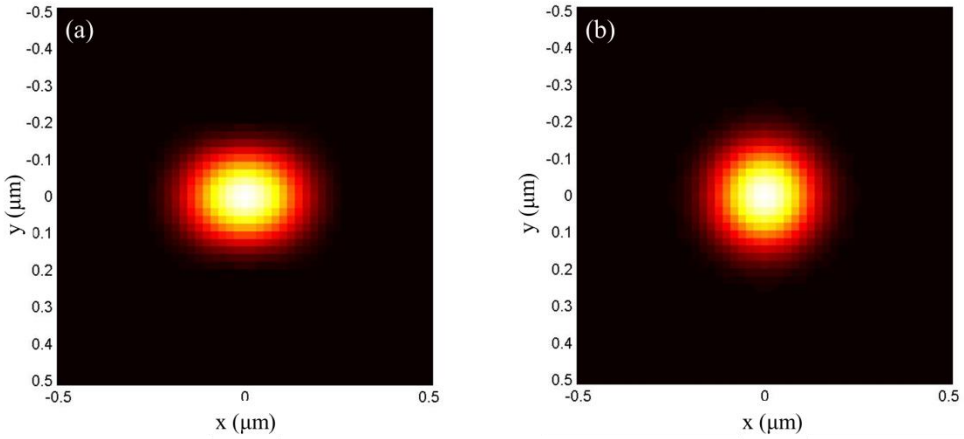

Fig.5-7. Simulation of focal spot by PSF software: (a) linear polarization, (b) circular polarization.

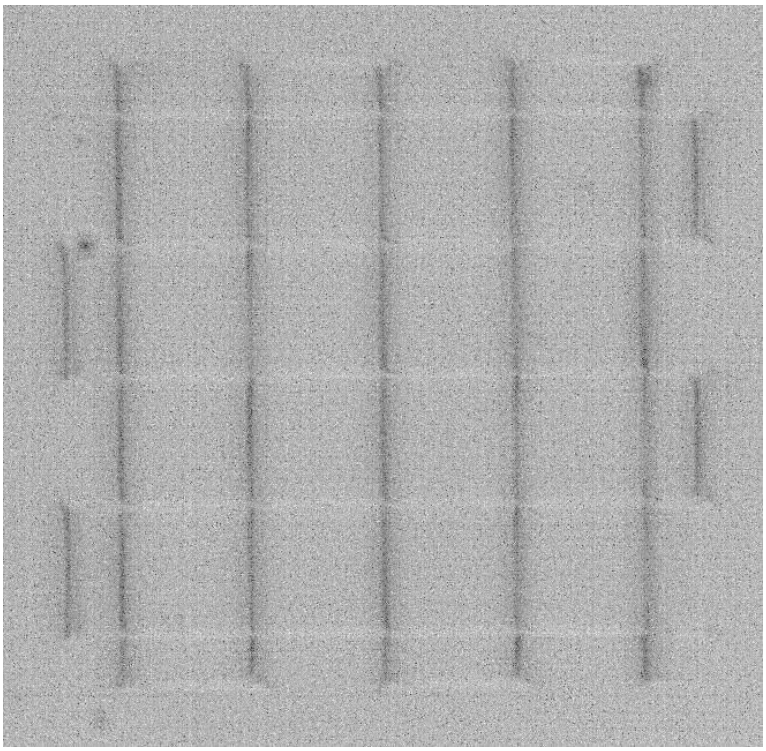

Fig.5-8. Gratings fabricated with linear polarization. (Photomer)

Therefore, with different functions and requirements of products, the polarization factor should be taken into account. In the case of fabricating gratings, the circular polarization is needed for achieving same width in x and y direction. This can be reached either by applying a half-wave plate to rotate the focal spot for 90 degree or a quarter-wave plate to change from linear to circular polarization.

5.1.6 Voxel simulation-influence of NA

In optics, Numerical aperture is commonly used to describe the acceptance cone of an objective and hence its light-gathering ability and resolution. Thus the different NA can have different voxel size at focal point. With $\beta_G = 0.9$, refractive index of ormocer 1.496, the FWHMxy andFWHMz at the focal point z = 0 μm in different NA is shown in Table 5-1.

Table 5-1.Ormocer voxel size with different NA simulated by PSF.

NA	FWHMxy (μm)	FWHMz (μm)	Intensity	ω_{0xy} (μm)	ω_{0z} (μm)
1.45	0.22	0.47	134.72	0.19	0.40
1.4	0.23	0.53	115.29	0.20	0.45
1.3	0.24	0.66	84.35	0.20	0.56
0.85	0.36	1.83	15.12	0.31	1.56
0.65	0.46	3.25	5.16	0.39	2.76
0.45	0.66	6.95	1.19	0.56	5.91
0.25	1.18	22.87	0.11	1.00	19.44
0.12	2.46	99.75	0.006	2.09	84.79

As for calculating the beam waist ω_{xy} and ω_z to obtain the voxel size, it is known that for FWHM the intensity is half of the maximum intensity can be computed as:

$$I = \frac{I_0}{2} \tag{4.1}$$

The distance along r axis at FWHM is given by:

$$2r = FWHM \tag{4.2}$$

By substituting Equation (4.1) and Equation (4.2) into Equation (1.15), the beam waist can be computed as:

$$\omega_0 = \sqrt{\frac{2}{\ln 2}}\frac{FWHM}{2} \approx 0.85 \times FWHM \tag{4.3}$$

The simulation shows that the FWHMxy and FWHMz changes dramatically with decreasing NA. The value changed in z is much larger than in x-y direction. Moreover, the intensity of the focal spot changes quickly while decreasing NA. The related graph is shown in Fig.5-9 to Fig.5-10.

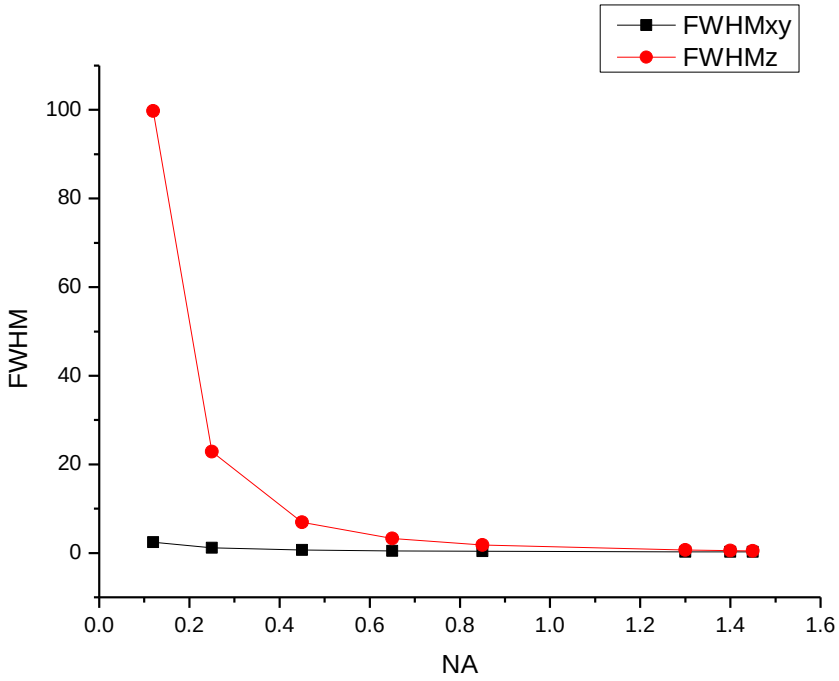

Fig.5-9.Ormocer FWHM value with different NA.

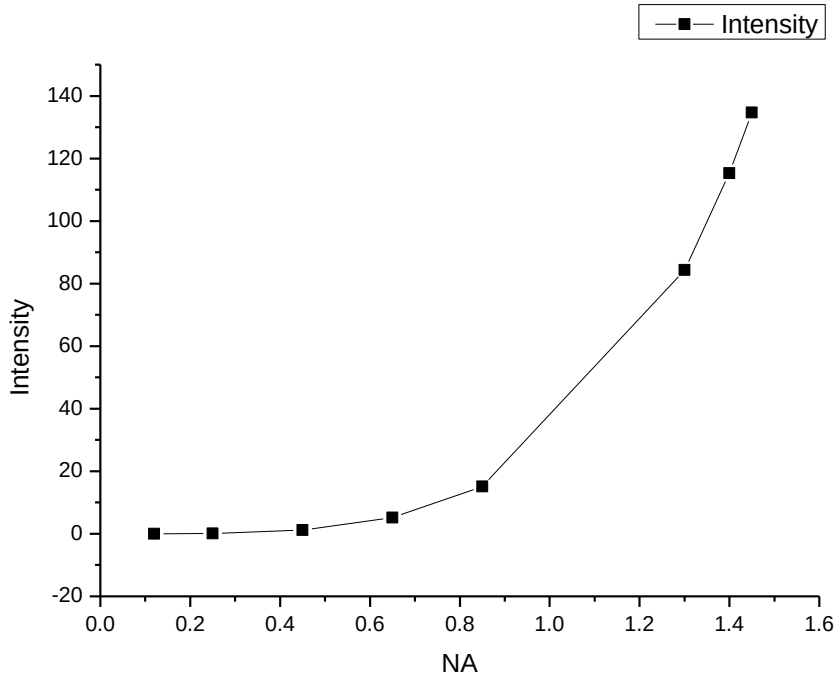

Fig.5-10.Ormocer focal intensity with different NA.

Therefore, for the purpose of shortening the fabrication time within acceptable surface roughness of the product, applying smaller NA objective with bigger voxel size is feasible. However, as the decrease of intensity with small NA, the threshold power increases rapidly. Hence the large power is needed for large-fast fabrication in TPP.

5.1.7 Voxel simulation-impact of focal depth

In large-scale fabrication of TPP, structure height over 200 μm is our goal. This inspired us to analyze the focal point change with different z depth. For ormocer with NA=1.4 objective, the results are shown in Fig.5-11 and Fig.5-12. The FWHMxy almost has no change; however, the FWHMx changed rapidly while increasing z position. The intensity is even 6 times smaller at z depth = 200 μm than at z depth = 0 μm. Therefore, if we are fabricating products with large height, the laser power should be increased during fabrication to compensate the intensity changes due to increasing z depth. Such phenomenon is indicated in Fig.5-13, which fabrication height of the scaffold is 50 μm instead of the designed height 68 μm. This is attributed to the laser power is not enough for polymerization at z higher than 50 μm.

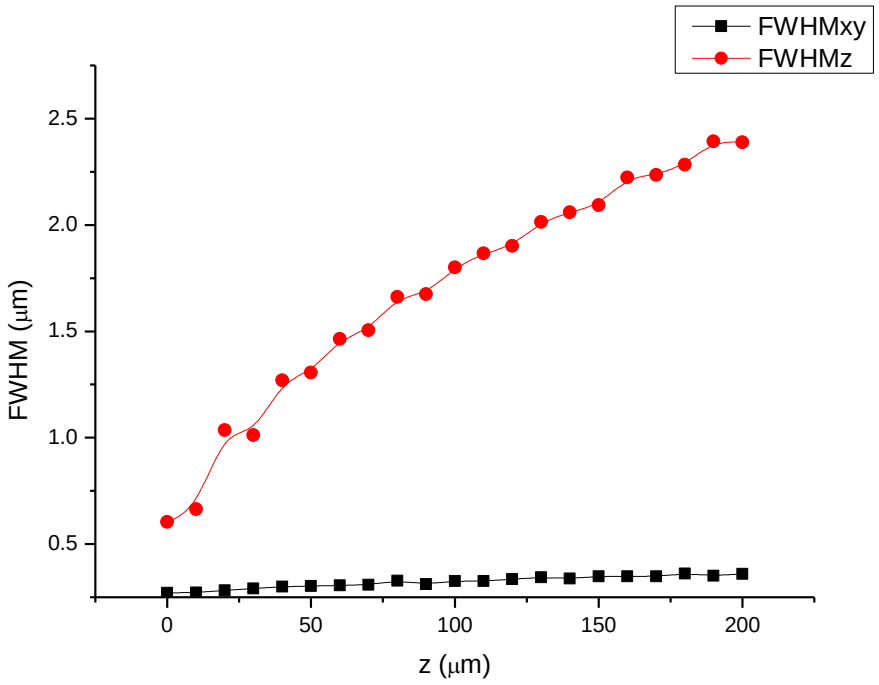

Fig.5-11.Ormocer FWHM changes with different z position.

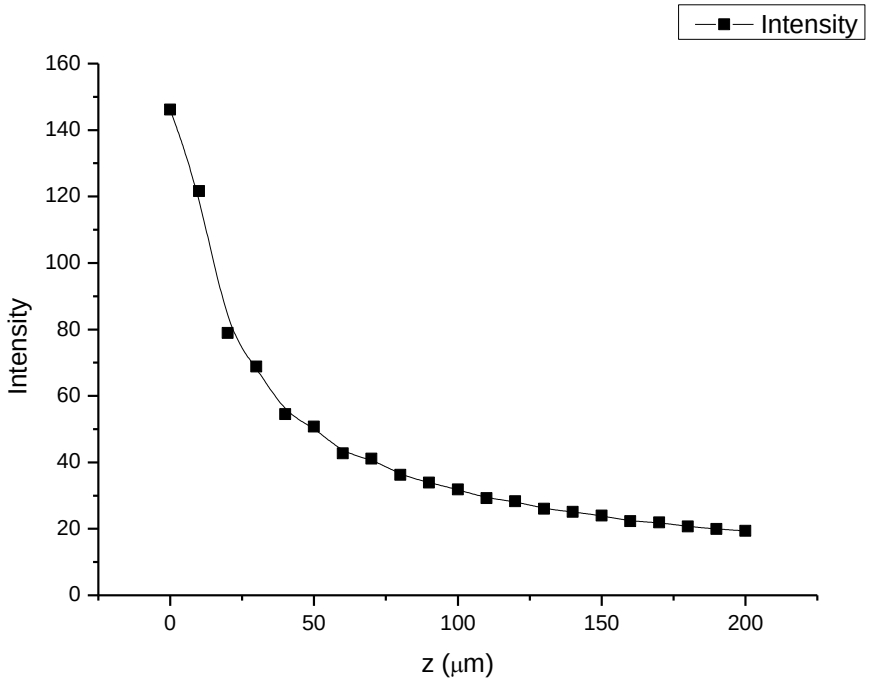

Fig.5-12.Ormocer intensity changes with different z position.

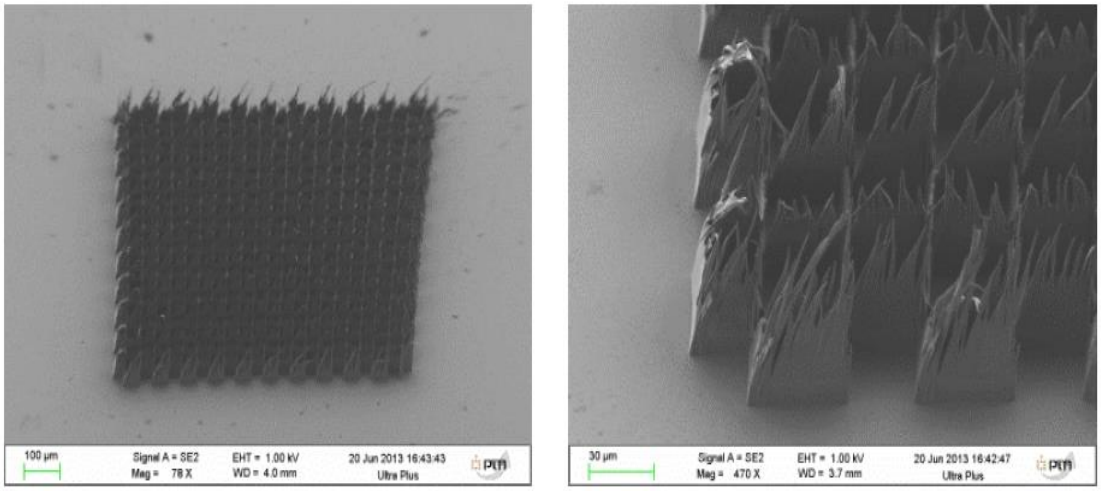

Fig.5-13. Scaffold fabricated without laser compensation at high z position: (left) the overall view $0.8mm \times 0.65mm \times 68\mu m$, (right) zoom-in view and the scaffold height is $50\ \mu m$.

5.1.8 Voxel simulation-laser compensation

The strategy for laser compensation is to adjust the power condition same as the z depth = $0\ \mu m$. By definition, the intensity and power formula is:

$$P = \int I \cdot dA \tag{4.4}$$

wheredA is a differential element of a closed surface that contain the source. In our case, dA is equals to the surface area of the voxel size, which is in the shape of ellipsoid. The Cartesian coordinate system shows the equation of an ellipsoid centered at the origin is:

$$\frac{x^2}{a^2}+\frac{y^2}{b^2}+\frac{z^2}{c^2}=1 \tag{4.5}$$

The a, b and c is corresponding to the points (a,0,0), (0,b,0) and (0,0,c) on the ellipsoid respectively. By defining $X=a\cos\theta$, $Y=b\sin\theta\cos\varphi$, $Z=c\sin\theta\sin\varphi$ in sphere coordinate, the surface integral can be compute as:

$$S=\int_0^{2\pi}\int_0^{\pi}\sqrt{U(\theta,\varphi)V(\theta,\varphi)-W^2(\theta,\varphi)}\,\mathrm{d}\theta\mathrm{d}\varphi \tag{4.6}$$

Where $U(\theta,\varphi)=\left[\left(\frac{\partial X}{\partial\theta}\right)^2+\left(\frac{\partial Y}{\partial\theta}\right)^2+\left(\frac{\partial Z}{\partial\theta}\right)^2\right]$, $V(\theta,\varphi)=\left[\left(\frac{\partial X}{\partial\varphi}\right)^2+\left(\frac{\partial Y}{\partial\varphi}\right)^2+\left(\frac{\partial Z}{\partial\varphi}\right)^2\right]$, and $W(\theta,\varphi)=\left[\frac{\partial X}{\partial\theta}\frac{\partial X}{\partial\varphi}+\frac{\partial Y}{\partial\theta}\frac{\partial Y}{\partial\varphi}+\frac{\partial Z}{\partial\theta}\frac{\partial Z}{\partial\varphi}\right]$.

Thus, the approximate value of S can be computed as:

$$S\approx 4\pi\left(\frac{a^pb^p+a^pc^p+b^pc^p}{3}\right)^{1/p} \tag{4.7}$$

Here $p\approx 1.6075$ yields a relative error of at most 1.061 %, which is acceptable for engineering use.

The reason for calculating the surface area of ellipsoid is because the voxel size is changing as z depth increasing. And if we want to calibrate the power, we need to handle the relation of power and intensity carefully. Table 5-2 shows the detail results in simulation of ormocer with NA=1.4.

Table 5-2.Ormocer simulation for laser compensation.

Zposition (μm)	Intensity	FWHMxy	FWHMz	Surface area	Power	Compensation rate
0	146.1128	0.27068	0.60355	0.31224	45.62282	1
10	121.6386	0.27141	0.66394	0.34081	41.45571	1.10052
20	78.9356	0.28232	1.0361	0.53556	42.27469	1.0792
30	68.8073	0.29088	1.0122	0.54081	37.21176	1.22603
40	54.4535	0.30046	1.2692	0.69307	37.74011	1.20887
50	50.7254	0.30226	1.3068	0.71711	36.37559	1.25422
60	42.726	0.30579	1.4642	0.80939	34.58188	1.31927
70	41.1111	0.30863	1.5049	0.83903	34.49338	1.32265
80	36.196	0.32697	1.6615	0.97991	35.46867	1.28629
90	33.9308	0.31208	1.675	0.94113	31.93344	1.42868
100	31.8726	0.32624	1.8	1.05633	33.66796	1.35508
110	29.1752	0.32549	1.8669	1.09179	31.85323	1.43228
120	28.2638	0.33498	1.9019	1.14503	32.36295	1.40972
130	26.0323	0.34325	2.0141	1.24133	32.3147	1.41183
140	25.112	0.33708	2.0592	1.24494	31.26293	1.45933
150	23.9522	0.34786	2.0926	1.30613	31.28473	1.45831
160	22.3146	0.34827	2.2234	1.38727	30.95627	1.47378
170	21.9211	0.34732	2.2354	1.39067	30.48502	1.49657
180	20.687	0.36146	2.2839	1.47936	30.6036	1.49077

190	19.9228	0.35132	2.393	1.50386	29.96118	1.52273
200	19.3772	0.36017	2.3894	1.54036	29.84778	1.52852

Here, the ellipsoid parameters a and b is assumed the same and it equals to 0.85FWHMxy. The ellipsoid parameter c is defined by 0.85FWHMz. Therefore, the surface area can be computed by Equation (4.7). Hence the power = SI can be determined. In TPP fabrication, the power used in the focal point at z=0 μm is recognized as the threshold power of the resin. After normalizing power at different z depth with the threshold, one can get the compensation rate as shown in Fig.5-14. The fitting curve of laser compensation is employed in the following fabrication and its formula is:

$$\text{Compensation Rate}=0.78z^{0.125} \quad (4.8)$$

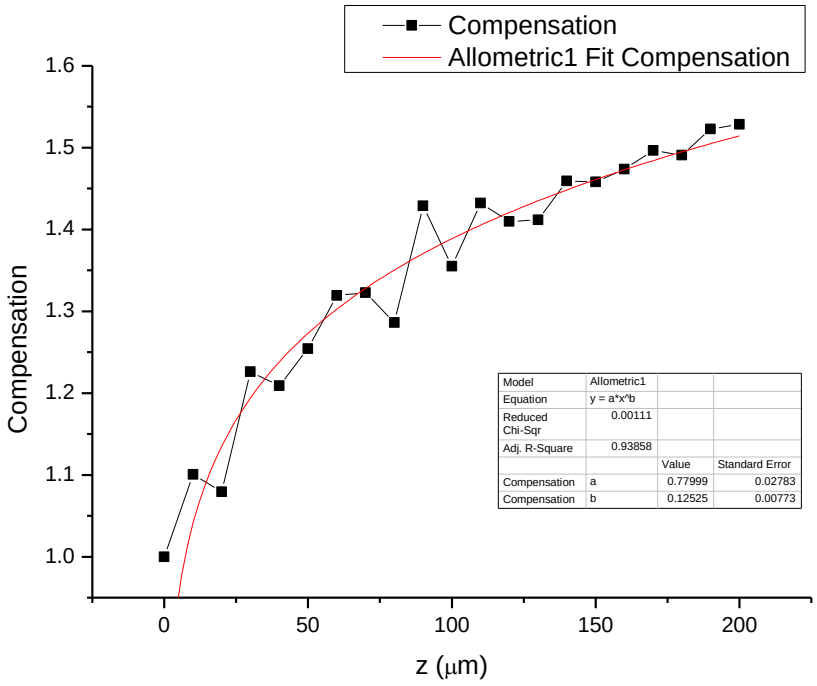

Fig.5-14. Laser compensation for Ormocer with NA=1.4.

Besides the laser compensation, the focusing z position should be also corrected since the z position shifts while increasing z depth (see Table 5-2). Such correction is also implemented in the laser compensation software.

5.2 Large TPP structures and parallel beams fabrication

In this section, we'll display the large structures we made for bio-medical application and discuss the feasibility of massive parallel beams fabrication in TPP by applying diffractive optical elements.

5.2.1 Fabrication of scaffold

For designing the shape of bio scaffold, the parameters are shown in Fig.5-15.

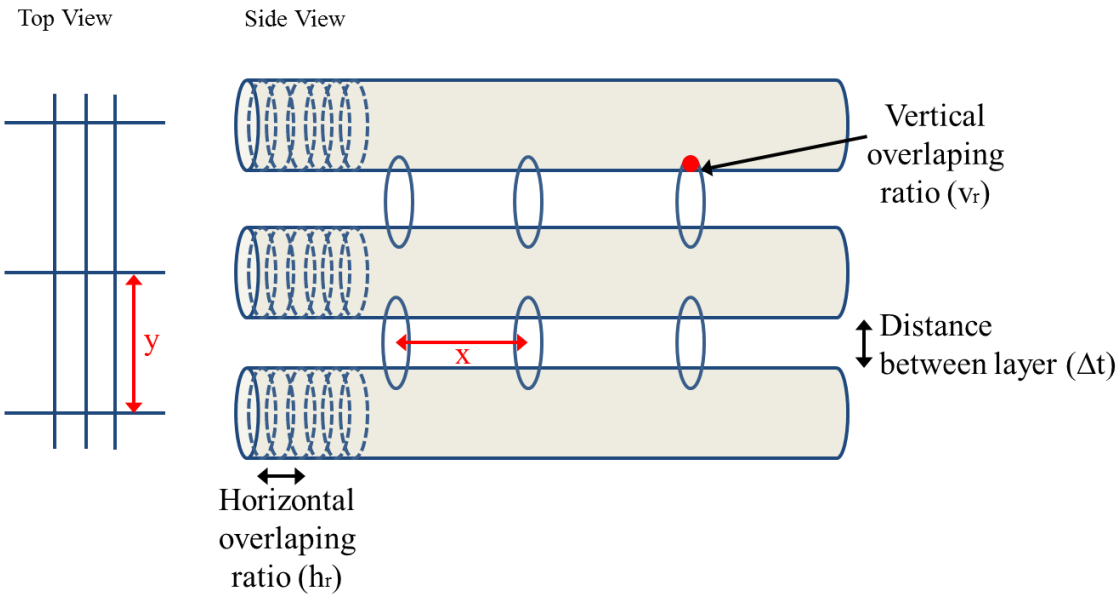

Fig.5-15.The illustration of scaffold parameters.

The purpose of bio scaffold is to support and maintain the cells, thus the porosity should be high enough for storing function. In recent bio applications, the cells should be maintained in the square size of 50 μm, which is set as our parameters ($x = y = \Delta t$). The size of scaffold is preliminary set as a square with 1 mm in width. Before fabrication, it takes two steps for pre-processing, including autofocus and tilt correction for quality control. The laser compensation and z depth correction is also carried out while fabricating. For fabricating such big products, MS200 X-Y is needed for achieving large working distance. Moreover, the large NA objective is no longer suitable. In this case, the Zeiss 40X with NA=0.85 was selected to obtain a good compromise with lateral and longitudinal resolutions. The overlapping ration Hr and Vr is also plans an important role. For example, Fig.5-16 shows the scaffold after washing step. Some top layers were collapse due to lack of vertical overlapping ratio. In TPP, the overlapping ratio between two voxels for good mechanical properties should at least 40%, which is controlled by the speed of X-Y motor and the laser power.The speed is set as 1 mm/s, and the voltage of laser is set as 1.2V. The power and voltage relation is shown in Fig.5-17.

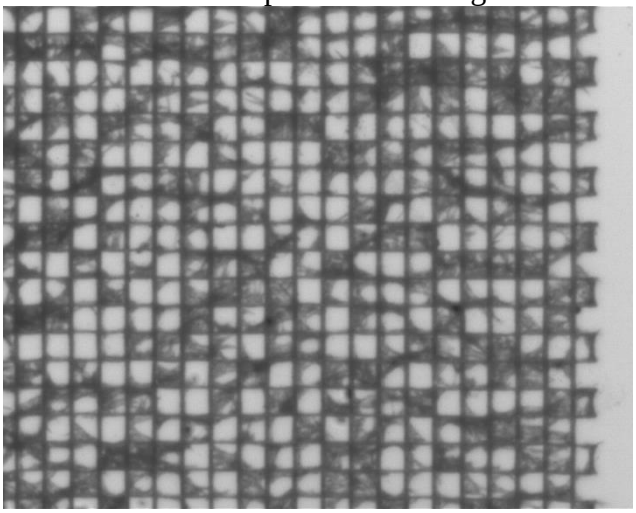

Fig.5-16. Scaffold with bad selection of overlapping ratio after washing steps.

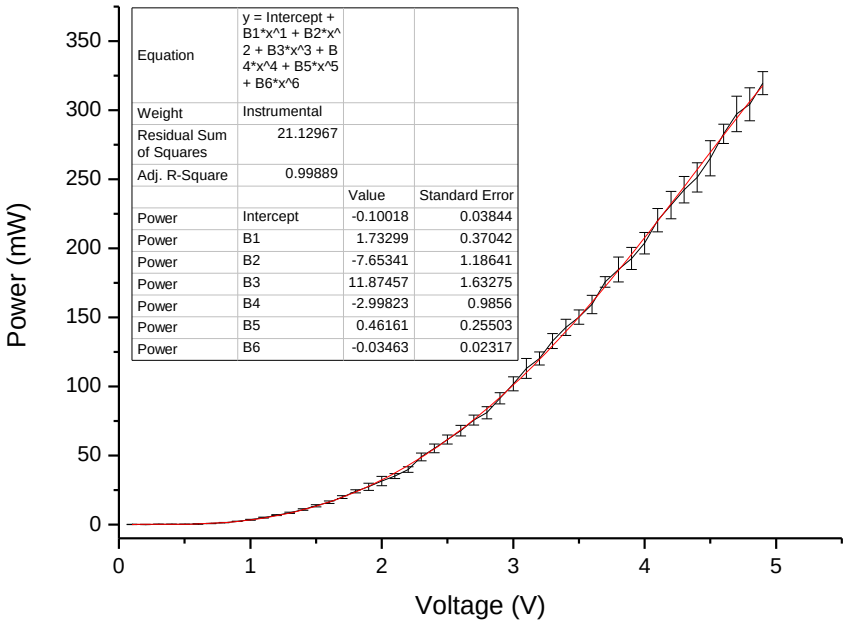

Fig.5-17. Power-voltage relation of TPP system we use.

In ormocer resin, the threshold power is around 0.6mw (FWHMxy=0.36 μm and FWHMz=1.83 μm). Therefore, from Fig.5-17, 1.2V is equals to 6.742mw, which means the focal point at z=0 μm is FWHMxy=0.792 μm, FWHMz=4.03 μm computed by Equation (1.16) and Equation(1.17). Based on the voxel size and the velocity we selected, the parameters of overlapping ratio can be determined.

Fig.5-18 shows the $1mm \times 1mm \times 100\mu m$ scaffold we fabricated. Although the size is set as 1 mm square, the shrinkage effect results in only 850 μm in each side and the vacancy space is around 30 μm. The fabrication linear speed was operated at 6.8 cm/sec and the total fabrication time was within 5 mins.

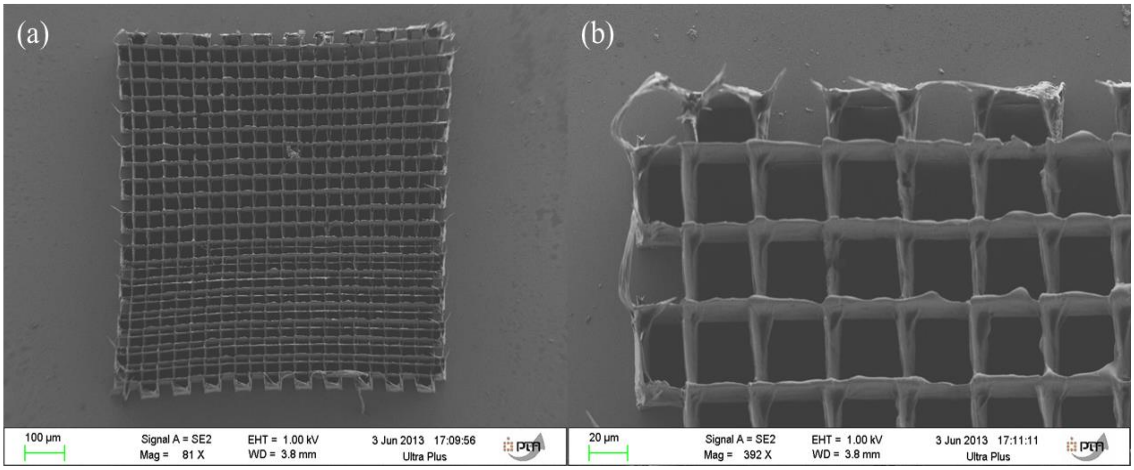

Fig.5-18. Scaffold with size $1mm \times 1mm \times 100\mu m$: (a) overall view reveals the shrinkage effect is around 150 μm, (b) the detail view of vacancy space.

5.2.2 Fabrication of needles

The reason we applied TPP technology is to discuss the feasibility of new type rotary needles that can be used in future dental treatment. With high bio-compatible resin ormocer used as the material of needle, the occurrence of infections while it breaking inside the canal is much lower than Ni-Ti rotary needle.
In this study, the high aspect ratio needle was fabricated with Zeiss 40X/0.85 and z position is controlled by Axiovert 200M Zeiss motorized microscope, which resolution in z is 50nm. In the beginning the resin ormocer was put into the PMMA container as shown in Fig.5-19 so that the height of resin is around 1.5cm. The planning process of solid model by CAD is as mentioned in Section 3.7.4.

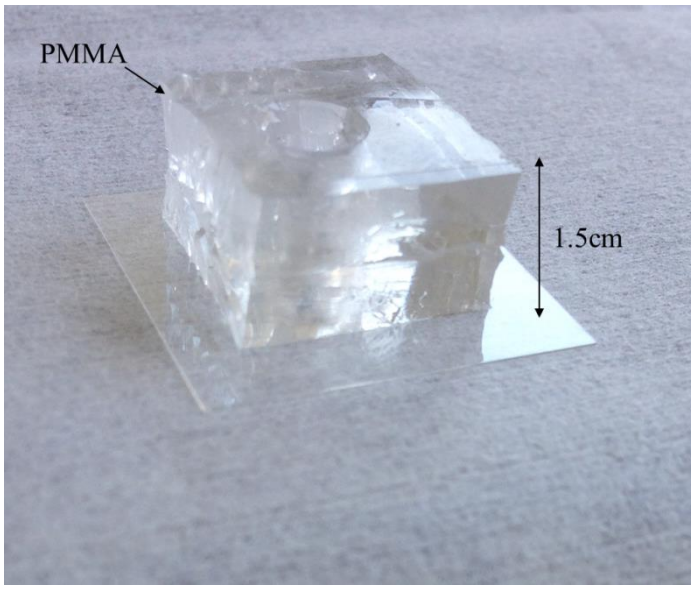

Fig.5-19.PMMA container for the purpose of increasing resin height.

So far,the cm-size needle as shown in Fig.5-20 was fabricated to demonstrate that the power available with the amplified laser was sufficient to compensate for the spot size degradation by spherical aberration when the focus to substrate height increases.

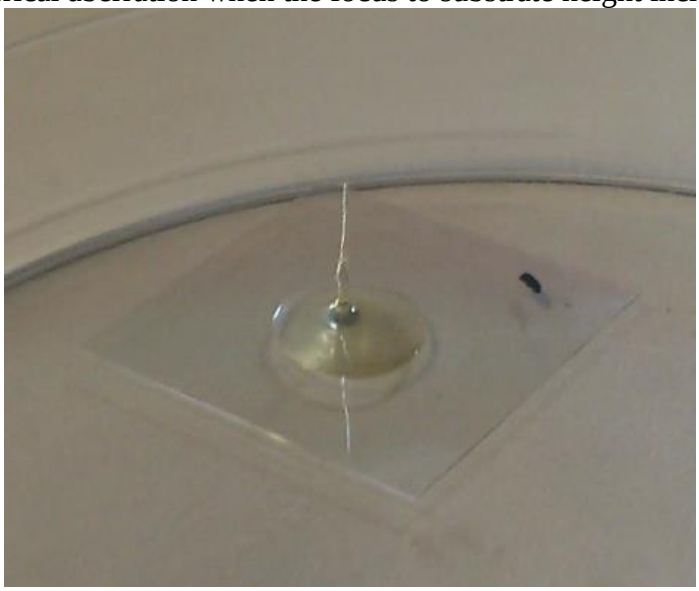

Fig.5-20. Needle of 1.2 cm height fabricated with 130 kHz amplified microchip laser with maximum average power of 200 mW to compensate for spherical aberration.

5.2.3 Parallel beams fabrication

The purpose of parallel beams fabrication is to speed up the fabrication process in mass production. The concept is to employ the diffractive optical elements before the laser beam enters the microscope objectives for multiple beams generation. The related principles had been introduced in Section 2.3.3. Here, we mainly focus on the DOEs applications and its potential in TPP manufacturing.

Fig.5-21 shows the DOEs we use, including 3×3, 25×25 and 47×47 array. The green mark on the DOE is its fabrication parameter, indicating the exposure time in the DOE fabrication process for the purpose of finding which parameter can eliminate zero order effect the most. Different separation angles had been applied;including $0.058°$, $0.166°$, $0.233°$, $0.466°$ and $0.930°$ in 3×3 array, $0.334°$, $0.446°$ and $0.669°$ in 47×47 array, $0.233°$ in 25×25 array.

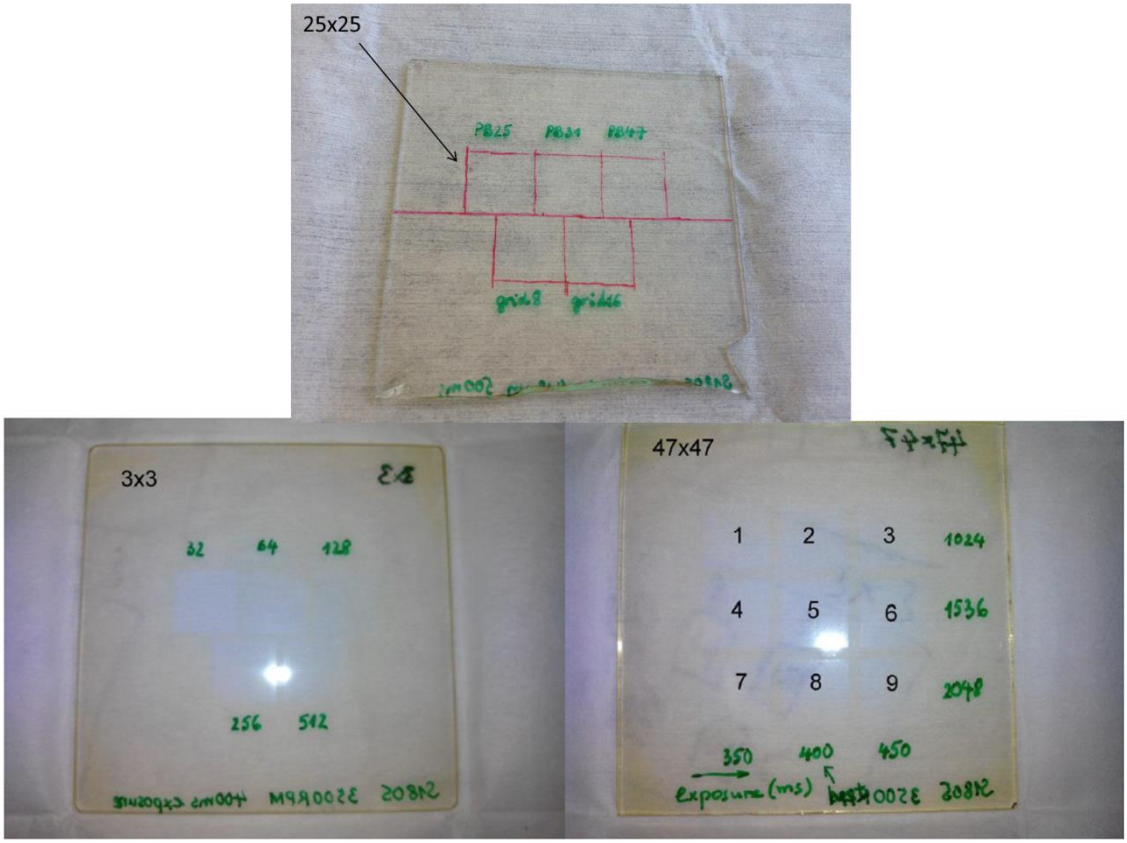

Fig.5-21.Different DOE with different manufacturing parameters.

The experiment was done by OLYMPUS PlanApo N 60X/1.45 objectiveinstalled on the Zeiss microscope and the material of resin is Photomer. The equivalent magnification is followed by the ratio square of focal length of tube

length: $60\times\left(\frac{\text{Microscope Axiovert}}{\text{Objective}}\right)^2=60\times\left(\frac{165mm}{180mm}\right)^2=50.41$. Since the laser intensity distribution after DOEs may change due to some defects in DOEs fabrication, it is better to check the laser beams array intensity on the focal point before fabrication. Fig.5-22 to Fig.5-26 shows some characteristiclaser beams pattern after DOEs.

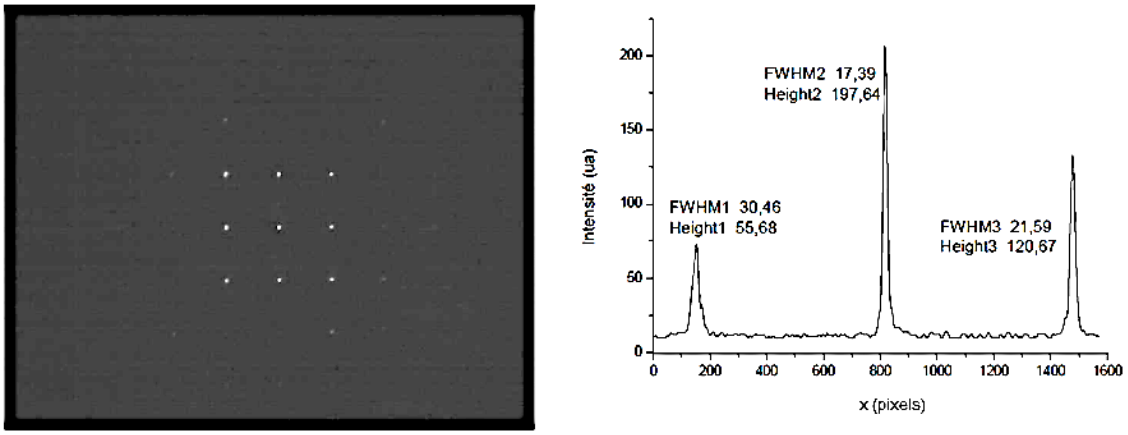

Fig.5-22.Laser beams focused after 3×3 DOEs 128 with $0.233°$ separation angle: (left), the overall view, (right), theintensity distribution.

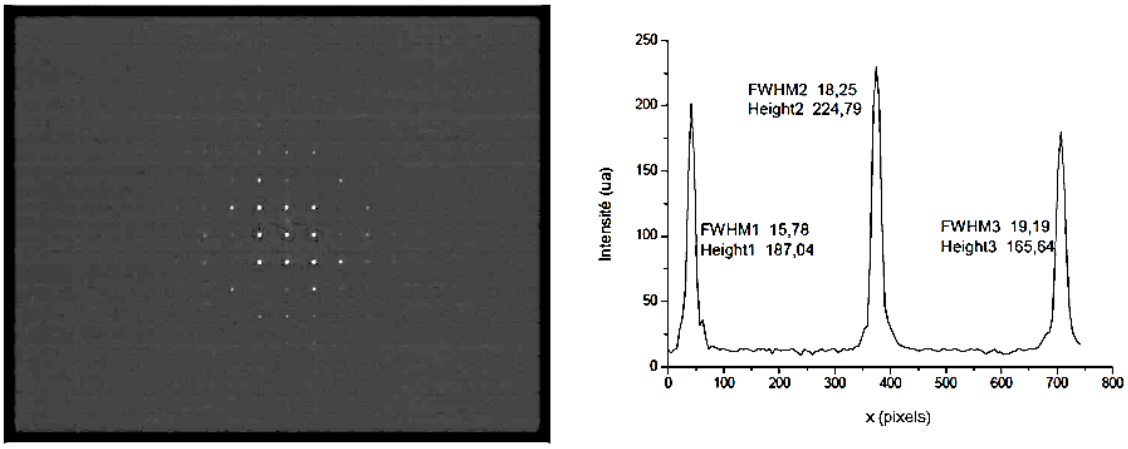

Fig.5-23. Laser beams focused after 3×3 DOEs 256 with $0.166°$ separation angle: (left), the overall view, (right), theintensity distribution.

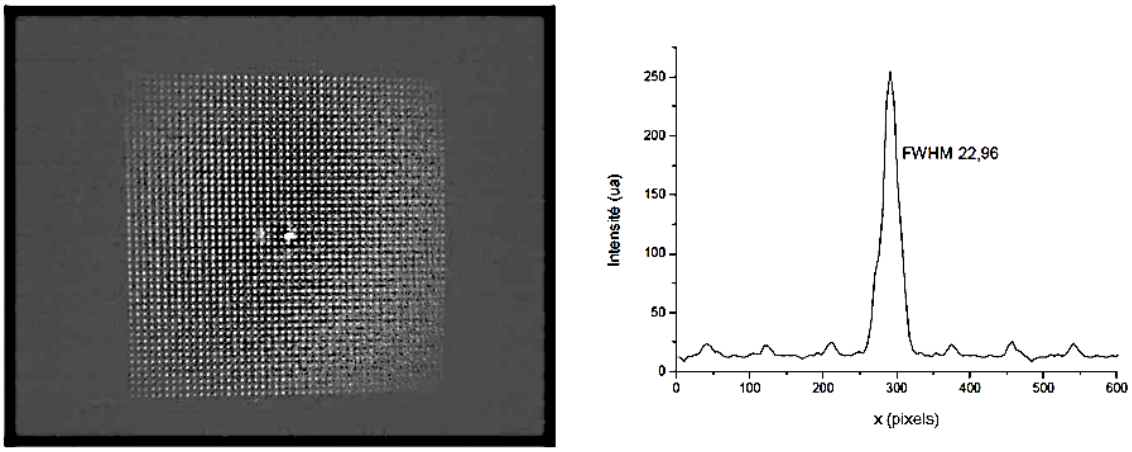

Fig.5-24. Laser beams focused after 47×47 DOEs No.2 with $0.669°$ separation angle: (left), the overall view, (right), theintensity distribution.

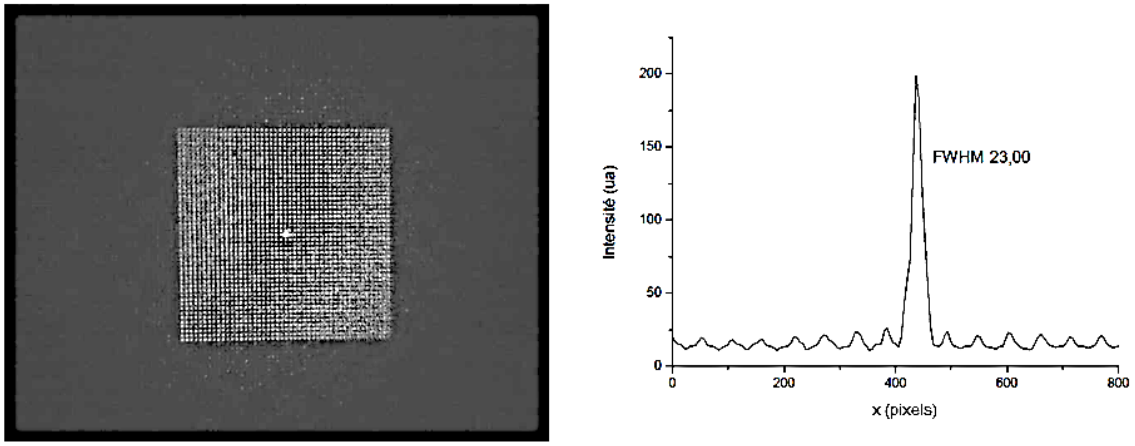

Fig.5-25. Laser beams focused after 47×47 DOEs No.5 with $0.446°$ separation angle: (left), the overall view, (right), theintensity distribution.

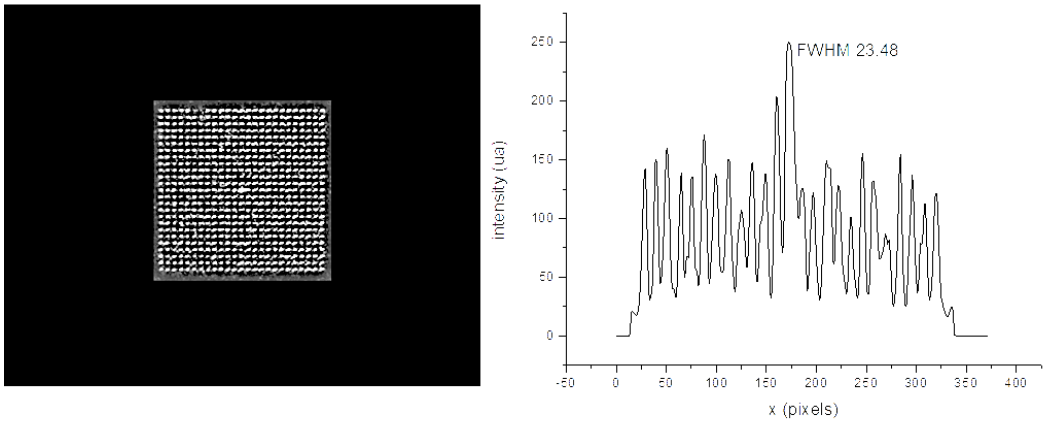

Fig.5-26. Laser beams focused after 25×25 DOEs with $0.233°$ separation angle: (left), the overall view, (right), theintensity distribution.

The intensity distribution is defined by:

$$\text{Intensity distribution}(\%)=\frac{\text{intensity of secondary points-noise}}{\text{intensity of central point-noise}}\times100\% \qquad (4.9)$$

And the factor of enlargement in the intensity secondary points relative to the central point is followed by:

$$\text{Enlargement}=\frac{\text{width of secondary points}}{\text{width of cenntral point}} \qquad (4.10)$$

Thus the intensity distribution (%) and enlargement is 70%/1.45 in Fig.5-22, 95%/0.8 in Fig.5-23, 5%/0.7 in Fig.5-24, 5%/0.8 in Fig.5-25 and 60%/0.8 in Fig.5-26. In TPP fabrication, the products resolution is based on the parameter we mentioned above. Therefore the best solution is to use 70%/1.45 and 95%/0.8 in 3×3 array, 5%/0.8 in 47×47 array and 60%/0.8 in 25×25 array.

Fig.5-27 shows the typical results made by 70%/1.45 and 95%/0.8 in 3×3 array. Obviously, we have certain degree of tilt problem in 70%/1.45 3×3 DOE, since in parallel beams fabrication, it's not able to adjust the intensity of focal point voxel by voxel like we did in

previous single beam fabrication. Therefore, the surface area of products should be small like Fig.5-27.b. Besides the tilt problem, the intensity distribution and secondary beams enlargement also affects the quality of products. Fig.5-27.a shows the square was even not completed at the edge due to lack of intensity (70%). Some voxels of the edge squares are bigger than the central one due to the secondary beams was expanded 1.45 times. To prevent this, one should have the perfect DOE without the zero order effect or control the intensity difference within 10%.

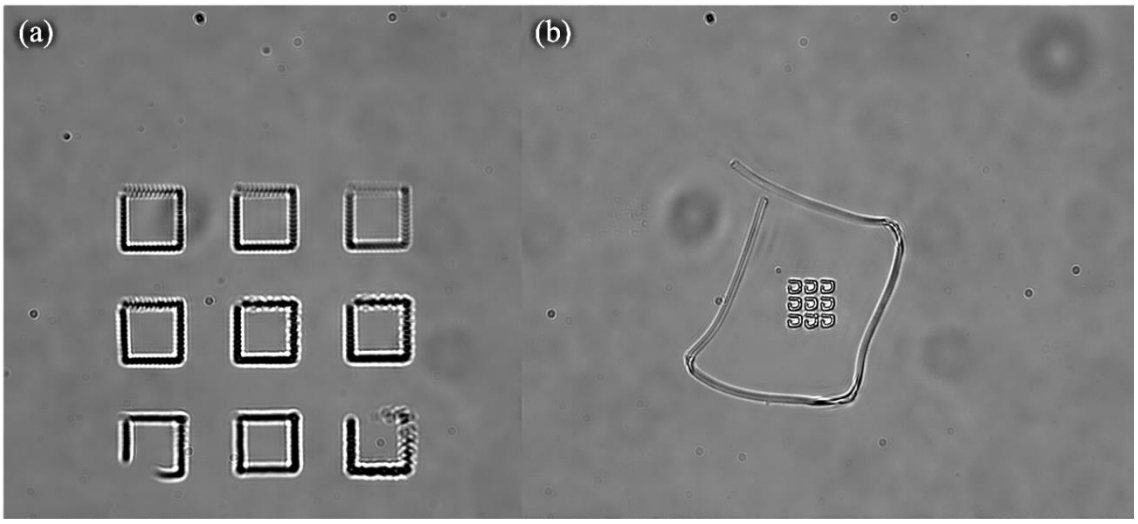

Fig.5-27. 3×3 Square array fabricated by (a) 70%/1.45 3×3 DOEwith separation angle $0.233°$ and (b) 95%/0.8 3×3 DOE with separationangle $0.166°$.

As for the two kinds of 47×47 DOEs we mentioned, since the distance between dots governed by separation angle and number of beams is too small to allow enough resolution, the result is bad as shown inFig.5-28.a. If we further changed it into bigger separation angle $0.669°$ as shown in Fig.5-28.b, too much energy was accumulated in the central due to the effect of zero order.This gives us the basic idea of the selection in the combination of separation angle and number of beams. Too small amount of beams doesn't benefit for mass production while too many beams doesn't good for products resolution due to the zero order effect.

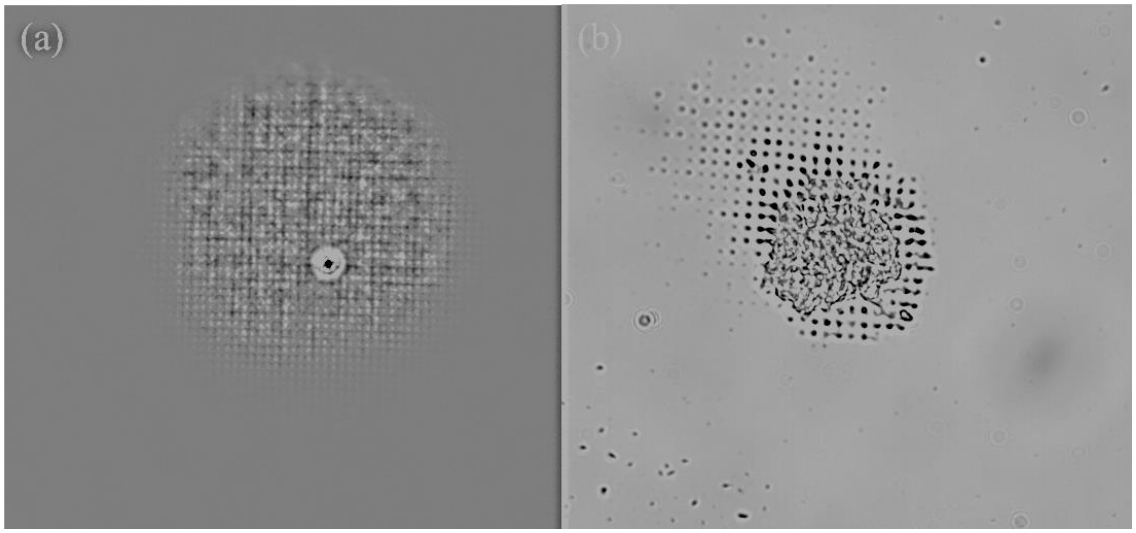

Fig.5-28. 47×47 Dots array fabricated by (a) DOEs No.2 with separation angle $0.446°$, (b) DOEs No.5 with separationangle $0.669°$.

In 25×25 dots array test, we took compromise with the number of beams and separation angle, applying 60%/0.8 as our parameters of intensity distribution and factor of secondary beam enlargement. The result is shown in Fig.5-29.

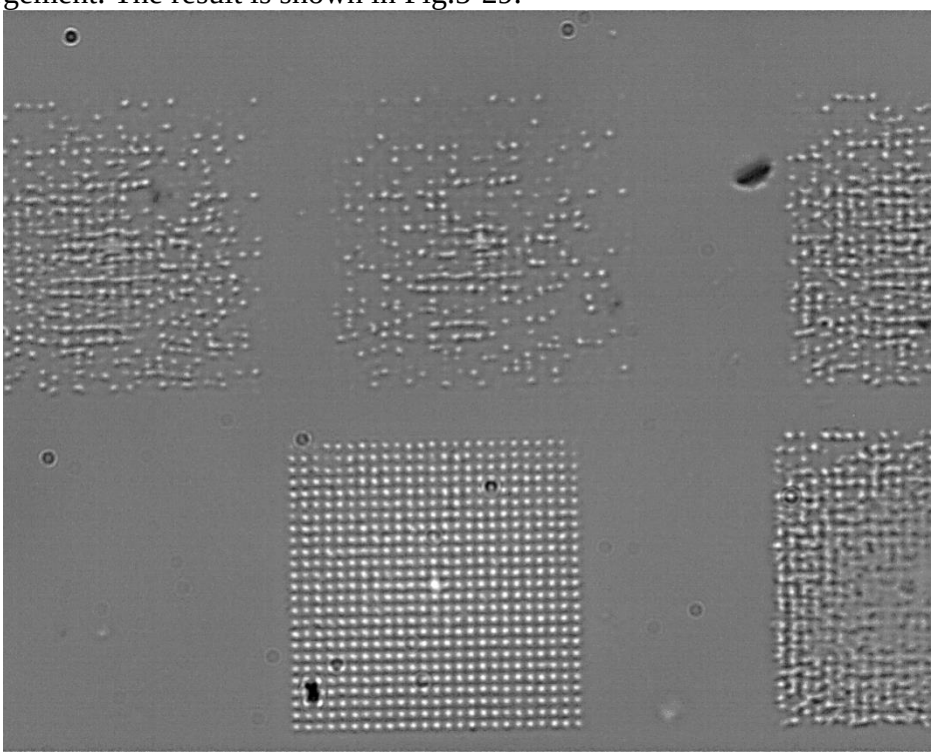

Fig.5-29. 25×25 Dots array fabricated by 60%/0.8 DOE with separationangle $0.233°$. (power 48mW, exposure time 10ms)

Unlike previous dots array, 25×25 DOE 60%/0.8 displays relatively good performance on dots, giving us the feasibility in mass production. However, the zero order effect still strong making too much energy accumulated in the center. This is a trade-off between quality and number of beams. In this case, the dots size can be computed by the Fig.5-30, thus the working distance is only 500nm.

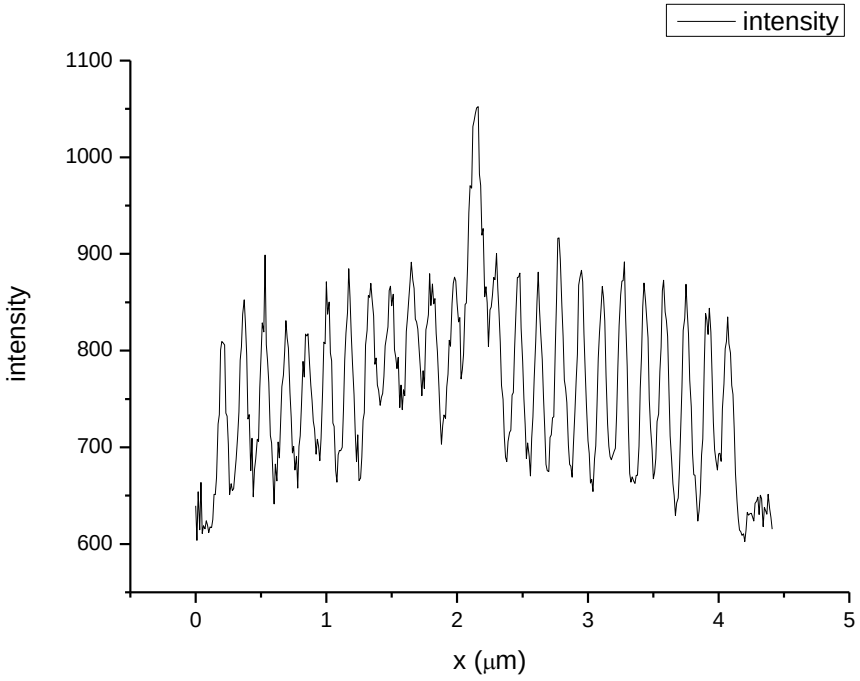

Fig.5-30.The size of 25 dots in the central horizontal line. (dots size is around 500nm)

In practical, it's really difficult to fabricate complex 3-D structures with only 500nm distance available. The most practical way is to apply 3×3, 4×4 or 5×5 DOEs working at the same separation angle, thus will get $4\,\mu m$, $3\,\mu m$ and $2\,\mu m$ working distance respectively.

Chapter 6 Conclusions and Recommendations

This study is focus on the improvement of fatigue life and cutting properties in Ni-Ti rotary instruments. So far, we demonstrate different methods to either prolong the fatigue life or increase the cutting efficiency. Besides, we have successfully developed a new FBG-based sensor for the monitoring of cyclic fatigue failure development in Ni-Ti rotary instruments. With the current wavelength interrogation system, we can detect every slight changes caused by strain waves at any time. Furthermore, we applied TPP technology to discuss the feasibility of new type needles made by polymer with high bio-compatibility. The following conclusions can be drawn:

6.1 Heat treatment effect

6.1.1 Fatigue life improvement

(1). Different heat treatments will affect the structure of Ni-Ti alloy and its phase transformation temperature. In HT400, around 2.12 to 2.43 times fatigue life as original Ni-Ti rotary instruments has been observed. It can be attributed to the phase of HT400 in the room temperature is almost Martensite, thus decreasing the crack propagation speed in the rotary instruments.

(2). HT600 has around 2.21 to 5.13 times fatigue life as original Ni-Ti instruments. Deducing its reason is recrystallization. It is observed that Ni-Ti alloy has recrystallization phenomenon when experiencing $500\,°C$ environment. The grain re-growth eliminates the residual stresses of endodontic files, decreasing the crack propagation speed, thus improving the fatigue life

(3). HT400+HT600 has a medium performance between HT400 and HT600. It's around 2.11 to 4.63 times fatigue life as the original.

(4). CT ha around 1.1 to 1.35 times fatigue life as original. The improvement is not as large as other heat treatment. It is because that the function of CT is to transform the residual austenite into martensite phase; however, in the room temperature, original file is almost in austenite phase. Therefore, the residual austenite is not enough to be transformed into martensite phase to improve fatigue life

6.1.2 Cutting properties

The cutting properties were tested by reciprocating movement. The conclusions are as follows:

(1). By comparing all data with the original file in different heat treatments, we find all of them more or less smaller than the original condition: -4.8% to -7.4% in HT400, -27.6% to -29.4% in HT600, -1.9% to -4.8% in HT400+CT, -11.1% to -25% in HT600+CT.

(2). CT is the good way to compensate the lack of cutting efficiency due to heat treatment. It has improvement around 2.7% to 3.3% in HT400 and 6.9% to 24.8% in HT600.

(3). HT400+HT600 still has a medium performance between HT400 and HT600.

6.2 Reciprocating movement

The reciprocating movement can reduce the tension stress on the rotary instrument, thus increasing the fatigue life. The conclusions are as follows:

(1). 1.34 to 2.54 times as traditional movement in HT400 condition.

(2). 6.42 to 11.31 times as traditional movement in HT600 condition.

(3). 1.2 to 1.59 times as traditional movement in CT condition.

(4). HT400+HT600 still has a medium performance between HT400 and HT600.

(5). Unlike tradition rotation, which has only one crack initiation point, the SEM fractographic analysis showed there were multi-crack initiation points at the edge of the fracture surface, increasing the time in crack propagation to have a better fatigue life performance.

6.3 Fatigue crack monitoring system

(1). The specific stress wave during instrument operation can be monitored.

(2). Frequencies and energy of characteristic frequency sections varied in a well-defined pattern during crack propagation and may reveal the microcosmic structure status in rotary instruments.

(3). The frequency of the signal components that exhibits the highest intensity are related to the instrument cutting frequency and its multiple.

(4). A large intensity spike in the characteristic frequency occurred during the latter stage of the instrument fatigue life and its occurrence is associated with the occurrence of a fatigue crack. This phenomenon may be made use of to provide a warning of imminent instrument fracture during clinical therapy.

(5). The criterion that the average of first 3 seconds data in real-time system can be used to warn the fracture for clinical therapy in most cases.

6.4 TPP fabrication

(1). By comparing the pixel intensity of camera at different z position, the maximum intensity can be found as focused point.

(2). Tilt correction based on autofocus method can be adjusted by rotating the coordinate system in fabrication process.

(3). Laser compensation can be identified by keeping the exposure condition same at different z position and it's useful in high aspect ratio structure.

(4). Large scale micro-fabrication is possible with Ormocer resin using 130 kHz amplified laser and XY motorized stage at a 5 mm/s linear speed.

(5). Massive parallel beams fabrication in TPP can be achieved by DOEs.

6.5 Recommendations

The suggestions are listed as follows:

(1). Experimental data shows that HT400+CT is the best choice in cutting efficiency perspective without taking compromise with fatigue life. However, in the real clinical application, the issue of cost in heat treatments still needs to be considered.

(2). The fatigue crack monitoring system can be more precisely by applying 3 FBGs for capturing stress wave signals in the future.

(3). New type of polymer based needle can be made by TPP. Unlike Ni-Ti alloy, the polymer based one gives us the opportunity to put some reinforcement materials inside to strengthen the mechanical properties.

(4). For fabricating scaffold or gratings by TPP, half-wave plate or quarter-wave plate can be applied to rotate the focal spot 90 or 45 degree to fabricate the vertical line with smaller line width of linear polarization. This can make the gap between parallel lines smaller.

(5). Motor control parameters like velocity and acceleration is important in large structure fabrication. Optimization of these parameters is needed in the future work.

(6). Parallel beams fabrication achieved by DOEs has huge zero order effect in the center, the quality of products is actually based on the quality of DOEs. To improve this, the fabrication process of DOEs should be modified in the future.

REFERENCES

[1] C. S. Shin and M. W. Lin,"An optical fiber based curvature sensor for endodontic files inside a tooth root canal," IEEE Sensors.,10(6), pp. 1061-1065, 2010.

[2] Lionel S. Marks, Marks' standard handbook for mechanical engineers, New York:McGraw-Hill, 10_{th}ed, pp. 20-25, 1996.

[3] 蕭琮仁, 牙齒根管治療之鎳鈦旋轉器械完整性檢測與評估, 碩士學位論文, 國立台灣大學, 2004.

[4] S. A. Thompson, "An overview of nickel-titanium alloys used in dentistry," International Endodontic Journal., 33(4), pp. 297-310, 2000.

[5] M. G. A. Bahia, R. C. Martins, "Physical and mechanical characterization of cyclic loading on the behavior of nickel-titanium wires employed in the manufacture of rotary endodontic instruments," International Endodontic Journal., 38, pp. 795-801, 2005.

[6] W. J. Buehler, F. E. Wang, "A summary of recent research on the Nitinol alloys and their potential application in ocean engineering,"Journal of Ocean Engineering, 1, pp. 105-120, 1967

[7] H. Funakubo, Shape Memory Alloys, New York: Gordon and Bleach, 1987.

[8] K. Otsuka, K. Shimizu, "Memory effect and thermoelasticmartensite transformation in Cu-Al-Ni alloy,"Scripta Metall., 4(6), 469, 1970.

[9] B. Sattapan, G. J. Nervo, J. E. A. Palamara, H. H. Messer, "Defects in rotary nickel-titanium files after clinical use," Journal of Endodontics., 26, pp.161-165, 2000.

[10] G. S. P. Cheung, B. Peng, Z. Bian, Y. Shen, B. W. Darvell, "Defects in ProTaperS1 instruments after clinical use: fractographic examination," International Endodontic Journal., 38, pp. 802-809, 2005.

[11] A. P. Spanaki-Voreadi, N. P. Kerezoudis, S. Zinelis, "Failure mechanism of ProTaper Ni-Ti rotary instruments during clinical use: fractographic analysis," International

Endodontic Journal, 39, pp. 171-178, 2006.

[12] 李俊傑, 鎳鈦旋轉器械之疲勞行為檢測, 碩士論文, 國立台灣大學, 2006.

[13] S. Miyazaki, K. Mizukoshi, T. Ueki, T. Sakuma and Yinong Liu, “Fatigue life of Ti-50 at.% Ni and Ti-40Ni-10Cu(at.%) shape memory alloy wires,” Materials Science & Engineering A., 273-275, pp.658-663, 1999.

[14] cH.Tobushi, T. Hachisuka, S. Yamada, P. H. Lin, “Rotating-bending fatigue of aTiNi shape-memory alloy wire,”Mechanics of Materials., 26, pp. 35-42, 1999.

[15] H.Tobushi,T.Nakahara,Y.Shimeno and T.Hachisuka, “Low-cycle fatigue of TiNi shape memory alloy and formulation of fatigue life,” J. of Engng. Mater. & Technology, Trans. ASME, Vol. 122, pp. 186-191, 2000.

[16] T.Sawaguchi, G.Kaustrater, A.Yawny,M. Wagner, and G.Eggeler, “Crack Initiation and Propagation in 50.9 At. pct Ni-TiPseudoelastic Shape-Memory Wires in Bending-RotationFatigue,”METALLURGICAL AND MATERIALS TRANSACTIONS A, VOLUME 34A, pp. 2847-2860, 2003.

[17] G. Eggeler, E. Hornbogen, A. Yawny , A. Heckmann and M. Wagner, “ Structural and functional fatigue of NiTi shape memory alloy,” Materials Science and Engineering, A378, pp.24–33, 2004.

[18] E. Hornbogen, “Some effects of martensitic transformation on fatigue resistance,”Fatigue Fract. Engng. Mater. Struct. Vol.25, pp.785-790, 2002.

[19] M. Wagner, T. Sawaguchi, G. Kaustrater, D. Hoffken and G. Eggeler, “ Structural fatigue of pseudoelasticNiTi shape memory wires,” Materials Science and Engineering A 378, pp.105-109, 2004.

[20] E. Hornbogen, “ReviewThermo-mechanical fatigue of shapememory alloys,”Journalof Material Science, 39, pp.385–399, 2004.

[21] R. Matsui, H.Tobushi, Y. Furuichi and H. Horikawa, “Tensile Deformation and Rotating-Bending Fatigue Properties of a Highelastic Thin Wire, a Superelastic Thin

Wire, and a Superelastic Thin Tube of NiTi Alloys," Journal of Engineering Materials and Technology, Transactions of the ASME, vol. 126, pp.384-391, 2004.

[22] Mitesh M. Patel, "Characterizing Fatigue Response of Nickel-Titanium Alloysby Rotary Beam Testing,"Journal of ASTM International, Vol. 4, No. 6, pp.1-11, 2007.

[23] N. H.Luebke,W. A.Brantley, Z. I.Sabri, F. L.Luebke, L. L.Lausten,"Physical dimensions, torsional performance, bending properties, and metallurgical characteristics of rotary endodontic instruments," J Endodon.,21, pp. 259-63, 1995.

[24] J.Pruett, D.Climent, D.Cames,"Cyclic fatigue testing of nickel-titanium endodontic instruments," J Endodon., 23(2), pp. 77-85, 1997.

[25] S.B. Mize et al., "Effect of sterilization on cyclic fatigue of rotary nickel-titanium endodontic instruments," J Endod., 24(12), pp. 843-847, 1998.

[26] G.M.Yared, F.E. BouDagher, and P. Machtou, "Cyclic fatigue of Profile rotary instruments after simulated clinical use,"IntEndod J., 32(2), pp. 115-9, 1999.

[27] Y.Haikel, R.Serfaty, G.Batemann, "Dynamic and cyclic fatigue of engine-driven rotary nickel-titanium endodontic instruments," J Endodon., 25(6), pp. 434-40, 1999.

[28] G.M.Yared, F.E. BouDagher, and P. Machtou, "Cyclic fatigue of Profile rotary instruments after clinical use,"IntEndod J., 33, pp. 204-207, 2000.

[29] D. B.Dietz, P. M.DiFiore, J. K.Bahcall, E. P.Lautenschlager,"Effect ofrotational speed on the breakage of nickel-titanium rotary files," J Endodon., 26, pp. 68-71, 2000.

[30] G. Gambarini, "Cyclic fatigue of ProFile rotary instruments after prolonged clinical use,"International Endodontic Journal, 34, pp. 386–389, 2001.

[31] U. M. Li, B. S. Lee, C. T. Shih, W. H.Lan and C. P. Lin, "Cyclic fatigue of endodontic nickel titanium rotary instruments: static and dynamic tests," J Endod.,28, pp. 448–451, 2002.

[32] C. J.Ullmann, O. A. Peters, "Effect of Cyclic Fatigue on Static Fracture Loads inProTaper Nickel-Titanium Rotary Instruments,"J Endod., 31,pp.183-186, 2005.

[33] N. M.Grande, G.Plotino, R.Pecci, R.Bedini, V. A.Malagnino, F.Somma, “Cyclic fatigue resistance and three-dimensional analysis of instruments from two nickel-titanium rotary systems,”IntEndod J.,39(10), pp. 755-63, 2006.

[34] G.Plotino, N. M.Grande, E.Sorci, V. A.Malagnino, F.Somma, “A comparison of cyclic fatigue between used and new Mtwo Ni-Ti rotary instruments,”IntEndod J., 39(9), pp. 716-23, 2006.

[35] A. C. D. Viana, B. M. Gonzalez, V. T. L. Buono, and M. G. A. Bahia, “Influence of sterilization on mechanical propertiesand fatigue resistance of nickel–titanium rotaryendodontic instruments,”International Endodontic Journal., 39, pp. 709-715, 2006.

[36] G. Plotino, N. M. Grande, E. Sorci, V. A. Malagnino, and F. Somma, “Influence of a brushing working motion on the fatigue life of NiTi rotary instruments,” International Endodontic Journal., 40, pp. 45-51, 2007.

[37] K. N. Melton, andO. Mercier, “Fatigue of NiTithermoelasticmartensites,”ActaMetall., 27, pp.137-144,1979.

[38] S.Miyazaki, M.Suizu, K.Otsuka, T.Takashima,“Effect of Various Factors onFatigue Crack Propagation Rate in Ti--Ni Alloys,” Proceedings of the MRSInternational Meeting on Advanced Materials Vol 9 Shape Memory Materials, pp. 263-268, 1989.

[39] S. W.Schneider, “A comparison of canal preparations in straight and curved canals,” Oral Surg.,32, pp. 271-5, 1971.

[40] J. M. Young and K. J. Van Vliet, “Predicting in vivo failure of pseudoelasticNiTi devices under low cycle, high amplitude fatigue,”Journal of Biomedical Materials Research Part B: Applied Biomaterials, 72B, pp. 17-26, 2005.

[41] I.Wang, M.Bouriau, P. L. Baldeck, C.Martineau, and C.Andraud,“Three-dimensional microfabrication by two-photon-initiated polymerization with a low-cost microlaser," Opt Lett., 27(15), pp. 1348-1350, 2002.

[42] S.Engelhardt, Y. L.Hu, N.Seiler, D. Riester, W.Meyer, H. Kruger, M. Wehner,

E.Bremus-Kobberling, and A. Gillner, "3D-microfabrication of polymer-protein hybrid structures with a Q-switched microlaser," J. Laser Micro Nanoeng., 6(1), pp. 54-58, 2011.

[43] E.Kapyla,S.Turunen, J.Pelto, J.Viitanen, and M.Kellomaki,"Investigation of the optimal processing parameters for picosecond laser-induced microfabrication of a polymer-ceramic hybrid material," J. Micromech. Microeng.,21(6), p. 10, 2011.

[44] K. S.Lee, D. Y. Yang, S. H. Park, and R. H.Kim, "Recent developments in the use of two-photon polymerization in precise 2D and 3D microfabrications," Polymers for Advanced Technologies., 17(2), pp. 72-82, 2006.

[45] S. R.Marder, J. L. Bredas, and J. W. Perry,"Materials for multiphoton 3D microfabrication," Mrs Bulletin., 32(7), pp. 561-565, 2007.

[46] K.Kaneko, H. B. Sun, X. M. Duan,and S.Kawata, "Two-photon photoreduction of metallic nanoparticle gratings in a polymer matrix," ApplPhysLett., 83(7), pp. 1426-1428, 2003.

[47] K.Mukai,T.Yoshimura, S.Kitayama, and S.Maruo, "Electroless and electrolytic plating of photopolymerized resin for use in the micro-molding of three-dimensional nickel structures," Journal of Photopolymer Science and Technology., 20(2), pp. 285-290, 2007.

[48] K.Mukai, T. Yoshimura, and S.Maruo,"Micromolding of three-dimensional metal structures by electroless plating of photopolymerized resin," Japanese Journal of Applied Physics Part 1-Regular Papers Brief Communications & Review Papers., 46(4B), pp. 2761-2763, 2007.

[49] A.Ovsianikov, S.Schlie, A.Ngezahayo, A.Haverich, and B. N.Chichkov, "Two-photon polymerization technique for microfabrication of CAD-designed 3D scaffolds from commercially available photosensitive materials," Journal of Tissue Engineering and Regenerative Medicine., 1(6), pp. 443-449, 2007.

[50] J.Fischer, G. von Freymann, and M.Wegener, "The materials challenge in diffraction-unlimited direct-laser-writing optical lithography," Advanced Materials., 22(32), pp. 3578-3582, 2010.

[51] K.Masui, S. Shoji, K.Asaba, T. C. Rodgers, F.Jin, X.M.Duan, and S.Kawata, "Laser fabrication of Au nanorod aggregates microstructures assisted by two-photon polymerization," Opt. Express., 19(23), pp. 22786-22796, 2011.

[52] K. S.Lee, D. Y. Yang, S. H. Park, and R. H.Kim, "Recent developments in the use of two-photon polymerization in precise 2D and 3D microfabrications," Polymers for Advanced Technologies., 17(2), pp. 72-82, 2006.

[53] K. S.Lee, R. H. Kim, and P.Prabhakaran, "Two-photon stereolithography," Journal of Nonlinear Optical Physics & Materials., 16, pp. 59-73, 2007.

[54] S. M.Kuebler, M. Rumi, T. Watanabe, K. Braun, B. H.Cumpston, A. A.Heikal, L. L. Erskine, S.Thayumanavan, S. Barlow, S. R.Marder, and J. W. Perry, "Optimizing two-photon initiators and exposure conditions for three-dimensional lithographic microfabrication," Journal of Photopolymer Science and Technology., 14, pp. 657-668, 2001.

[55] H. B.Sun, T. Tanaka, and S.Kawata, "Three-dimensional focal spots related to two-photon excitation," ApplPhysLett., 80(20), pp. 3673-3675, 2002.

[56] K. K.Seet, S.Juodkazis, V.Jarutis, and H.Misawa, "Feature-size reduction of photopolymerized structures by femtosecond optical curing of SU-8," ApplPhysLett., 89(2), 2006.

[57] K.Takada, K.Kaneko, Y. D. Li, S.Kawata, Q. D. Chen, and H. B.Sun,"Temperature effects on pinpoint photopolymerization and polymerized micronanostructures," ApplPhysLett., 92(4), p. 041902, 2008.

[58] N.Uppal, and P. S.Shiakolas, "Modeling of temperature-dependent diffusion and polymerization kinetics and their effects on two-photon polymerization dynamics," J.

Micro-Nanolithogr. MEMS MOEMS., 7(4), p. 10, 2008.

[59] N.Uppal, "A mathematical model development and sensitivity analysis of two photon polymerization for 3D micro/nano fabrication," Doctoral Dissertation., The University of Texas at Arlington, 2008.

[60] N.Uppal, and P. S.Shiakolas, "Process sensitivity analysis and resolution prediction for the two photon polymerization of micro/nano structures," Journal of Manufacturing Science and Engineering.,Vol. 131, p. 051018, 2009.

[61] S. Maruo, and S. Kawata, "Two-photon absorbed Near-infrared photopolymerization for Three-dimensional Microfabrication," Journal of Microelectromechanical Systems., Vol. 7, pp. 411-415, 1998.

[62] J. Serbin, A. Egbert, A. Ostendorf, B. N. Chichkov, R. Houbertz, G. Domann, J. Schulz, C. Cronauer, L. Frohlich, and M. Popall, "Femtosecond laser-induced two-photon polymerization of inorganic-organic hybrid materials for appliactions in photonics," Opt. Lett., Vol. 28, pp. 301-303, 2003.

[63] R. J. DeVoe, H. Kalweit, C. A. Leatherdale, and T. R. Williams, "Voxels shapes in two-photon microfabrication," Proceedings of SPIE., Vol. 4797, 2003.

[64] R.Guo, S. Z.Xiao, X. M. Zhai, J. W. Li, A. D. Xia, and W. H.Huang,"Micro lens fabrication by means of femtosecond two photon photopolymerization," Opt. Express., 14(2), pp. 810-816, 2006.

[65] C. L. Lin, Y. H. Lee, C. T. Lin, Y. J. Liu, J. L. Hwang, T. T. Chung, and P. L. Baldeck, "Multiplying optical tweezers force using a micro-lever," Optics Express., Vol. 19, pp.20604-20609, 2011.

[66] P. L. Baldeck, C. L. Lin, Y. S. Lin, C. T. Lin, T. T. Chung, M. Bouriau, and G. Vitrant, "Optically driven Archimedes micro-screws for micropump applications: multiple blade design," Proc. SPIE., Vol. 8097, pp. 809713/1-809713/5, 2011.

[67] C. L. Lin, G. Bitrant, M. Bouriau, R. Casalegno, and P. L. Baldeck, "Optically driven

Archimedes micro-screws for micropump application,” Optics Express., Vol. 19, pp. 8267-8276, 2011.

[68] C. Heller, M. Schwentenwein, F. Varga, R. Liska and J. Stampfl, ”Biocompatible and biodegradable photopolymers for microstereolithography,” Proceedings of LAMP., 2009.

[69] P. Danilevicius, S. Rekstyte, E. Balciunas, A. Kraniauskas, R. Jarasiene, R. Sirmenis, D. Baltriukiene, V. Bukelskiene, R. Gadonas and M. Malinauskas, “Micro-structured polymer scaffolds fabricated by direct laser writing for tissue engineering,” Journal of Biomedical Optics., Vol.17/8, pp. 081405-1-081405-5, 2012.

[70] M. L. Roessle, A. Fatemi, “Strain controlled fatigue properties of steels and some simple approximations,” International Journal of Fatigue., Vol.22, pp. 495-511, 2000.

[71] B. E. A. Saleh and M. C. Teich, “fundamentals of photonics,” Wiley Interscience, 1991.

[72] R. Kashyap, “Fiber Bragg Grating,” Academic Press, 1998.

[73] C. L. Lin, “Opto-Mechanical Applications of Microstructured Materials,” PhD thesis, Joseph Fourier University/National Taiwan University, 2004.

[74] A. Bertholds and R. Dandliker, “Determine of Individual Strain-Optics Coefficient in Single-Mode Optical Fibers,” J. Lightwave Technol., Vol. 6, pp. 17-20, 1988.

[75] P. C. Hill and B. J. Eggleton, “Strain gradient chirp of fiber bragg gratings,” Electronic Letter., Vol.30, pp. 1172-1174, 1994.

[76] I. Wang, “Matériauxorganiquesmicrostructurésetoptique non linéaire: 1) Nanocristauxorganiques en matrice sol-gel pour l'optiquequadratique, 2) Polymérisationinitiée par absorption à deux photons pour la microfabrication 3D,” Doctoral Dissertation Thesis, Université Joseph-Fourier - Grenoble I, Grenoble, 2002.

[77] Y. H. Hsueh, “Automatic micro manufacturing system for two –photon polymerization,” Master thesis, National Taiwan University, 2013.

[78] C. T. Lin, “Simulation and Improvements of Two-Photon Polymerization Fabricating

Process," Doctoral thesis, National Taiwan University, 2012.

[79] R. Paschotta, "Encyclopedia of laser physics and technology,"http://www.rp-photonics.com/encyclopedia.html, 2012.

[80] M. Abramowitz, and M. W. Davidson, "Numerical aperture and resolution,"http://micro.magnet.fsu.edu/primer/anatomy/numaperture.html, 1998.

[81] C. M. Chang, "Evaluation of Fatigue and Cutting Properties of Endodontic Rotary Instrument," Master thesis, National Taiwan University, 2008.

[82] S. K. Sadrnezhaad and S. H. Mirabolghasemi, "Optimum temperature for recovery and recrystallization of 52Ni-48Ti shape memory alloy," Material & Design., Vol. 28, pp. 1945-1948, 2007.

[83] C. T. Lin, "Root canal cleanliness after preparation with different tapers of Ni-Ti rotary instrument," Master thesis, Kaohsiung Medical University, 2004.

[84] E. Shafer, "Comparison of Cutting Efficiency and Instrumentation of Curved Canals with Nickel-Titanium and Stainless-Steel Instruments," Journal of Endodontics., Vol. 25, pp. 427-430, 1999.

[85] W. S. Chang, "Plasma Immersion Ion Implantation of Nitrogen on Nickel-Titanium Endodontic Instruments," Master thesis, National Taiwan University, 2007.

[86] B. B. Tung, "Effect of ElectropolishingProFile Nickel-Titanium Rotary Instruments on Cyclic Fatigue Resistance, Torsional Resistance and Cutting Efficiency," Journal of Endodontics., Vol. 34, pp. 190-193, 2008.

[87] E. Shafer, "Effect of Physical Vapor Deposition on Cutting Efficiency of Nickel-Titanium Files," Journal of Endodontics., Vol. 28, pp. 800-802, 2002.

[88] J. C. Lin, "Study of Cutting Efficiency of Ni-Ti Endodontic Rotary Instrument," Master thesis, National Taiwan University, 2009.

[89] N. Zhao, H. Man, Z. Cui, and X. Yang, "Structure and wear properties of laser gas nitride Ni-Ti surface," Surf Coat Technol., Vol. 200, pp. 4879-4884, 2006.

[90] G. R. Zadno, T. W. Duerig, K. N. Melton, D. Stoeckel, C. M. Wayman, “Engineering Aspects of Shape Memory Alloys,” Butterworth-Heinmann, England, pp. 414-419, 1990.

[91] K. Tsuchiya, M. Inuzuka, M. D. Tomus, A. Hosokawa, H. Nakayama, K. Morii, Y. Todaka, M. Umemoto, “Martensitic Transformation in Nanostructured TiNi Shape Memory Alloy Formed Via Severe Plastic Deformation,” Material Science and Engineering., pp. 643-648, 2006.

[92] A. Wick, O. Vohringer, A. R. Pelton, “The bending behavior of NiTi,” Journal de Physique IV.,Colloque C8 (ICOMAT-95), Vol. 5, pp. 789-794, 1995.

[93] X. Huang, Y. Liu, “Effect of annealing on the transformation behavior and superelasticity of NiTi shape memory alloy,”ScriptaMaterialia., Vol. 31, pp. 153-160, 2001.

[94] S. Zhirafar, A. Rezaeian, M. Pugh, “Effect of cryogenic treatment on the mechanical properties of 4340 steel,” Journal of Materials processing Technology., Vol. 186, p. 298, 2007.

[95] G. Yared, “Canal Preparation using only one Ni-Ti rotary instrument: preliminary observations,” International Endodontic Journal., Vol. 41, pp. 339-344, 2008.

[96] G. De-Deus, E. J. L. Moreira, H. P. Lopes, C. N. Elias, “Extended cyclic fatigue life of F2 ProTaper instruments used in reciprocating movement,” International Endodontic Journal., Vol. 43, pp. 1063-1068, 2010.

[97] Y. H. Huang, “Reciprocating movement on the fatigue life of endodontic rotary instrument,” Master thesis, National Taiwan University, 2011.

[98] C. S. Shin, B. L. Chen, “A comparison of interrogation schemes for impact event monitoring using fiber bragg gratings,” Proc. SPIE 7493, pp. 749314-739316, 2009.

[99] N. Mandelker, G. Gheorghiu, H. Sheinkopf, I. Cohen and O. Levy, “Assessment of fatigue striation counting accuracy using high resolution scanning electron microscope,”

Engineering Failure Analysis., pp. 20-27, 2008.

[100] C. Martineau, R. Anemian, C. Andraud, I. Wang, M. Bouriau and P. L. Baldeck, "Efficient initiators for two-photon induced polymerization in the visible range," Chem. Phys. Lett., Vol. 362, pp. 291-265, 2002.

[101] C. L. Tseng, "Design and Fabrication of Micro Devices by Two-Photon Polymerization," Master thesis, National Taiwan University, 2011.

[102] C. P. Hung, "Quality Improvement for Micro Products Fabricated by Two-Photon Polymerization Technology," Master thesis, National Taiwan University, 2012.

[103] S. E. Huang, "Effect of Heat treatment on the Fatigue Life of Endodontic Rotary Instrument," Master thesis, National Taiwan University, 2010.

[104] C. S. Shin and C. C. Chiang, "Fatigue damage monitoring in polymeric composites using multiple fiber bragg gratings," International Journal of Fatigue., Vol. 28, pp. 1315-1321, 2006.

Appendix

Appendix 1: R7.5A40 fatigue test results operated at 400 rpm.

Radius(R)Angle(A)	Heat Treatment	Cycle number
R7.5A40°	As-Received	1401
		1377
		1488
		1277
		1534
	HT400	3496
		3848
		3011
		3234
		3660
	HT600	3234
		2898
		3001
		3358
		3364
	HT400+HT600	3282
		3588
		3030
		3255
		3307
	CT	1980
		1898
		1761
		2020
		1888

Appendix 2: R10A60 fatigue test results operated at 400 rpm.

Radius(R)Angle(A)	Heat Treatment	Cycle number
R10A60°	As-Received	878
		700
		812
		1043
		818
	HT400	1931
		1788
		1843
		1907
		1985

	HT600	1765
		1965
		1746
		1933
		1999
	HT400+HT600	1677
		1698
		1789
		1941
		1902
	CT	1020
		1044
		988
		1243
		1109

Appendix 3: R7.5A60° fatigue test results operated at 400 rpm.

Radius(R)Angle(A)	Heat Treatment	Cycle number
R7.5A60°	As-Received	704
		688
		809
		554
		698
	HT400	1691
		1288
		1487
		1901
		1877
	HT600	3674
		3874
		3080
		3354
		3679
	HT400+HT600	2980
		3033
		3541
		3402
		3061
	CT	880
		760
		744
		788

		707

Appendix 4: R5A60° fatigue test results operated at 400 rpm

Radius(R)Angle(A)	Heat Treatment	Cycle number
R5A60°	As-Received	612
		595
		529
		633
		654
	HT400	1292
		1343
		1277
		1109
		1398
	HT600	1898
		2641
		2439
		2332
		2358
	HT400+HT600	2952
		2877
		2910
		2444
		2569
	CT	684
		651
		688
		702
		606

Appendix 5: R7.5A40 with $\theta = 45°$ and $\alpha = 7°$ fatigue test results.

Radius(R)Angle(A)	Heat Treatment	Equivalent cycles(2π)
R7.5A40°	As-Received	5161
		4319
		4044
		4786
		5708
	HT400	11730
		13601
		13614
		12183

		10052
	HT600	34742
		39512
		23243
		29808
		26926
	HT400+HT600	31519
		18902
		28239
		29257
		19855
	CT	7324
		8041
		7709
		7144
		8107

Appendix 6: R10A60° with $\theta = 45°$ and $\alpha = 7°$ fatigue test results.

Radius(R)Angle(A)	Heat Treatment	Equivalent cycles(2π)
R10A60°	As-Received	3005
		3759
		4252
		3294
		4318
	HT400	5245
		6339
		3929
		4400
		5158
	HT600	29519
		19474
		36314
		22770
		20556
	HT400+HT600	31286
		19374
		22215
		17831
		24171
	CT	4898
		4193

		4470
		4540
		4318

Appendix 7: R7.5A60° with $\theta = 45°$ and $\alpha = 7°$ fatigue test results.

Radius(R)Angle(A)	Heat Treatment	Equivalent cycles(2π)
R7.5A60°	As-Received	1476
		2474
		2283
		1994
		2785
	HT400	5866
		4315
		5150
		6010
		5235
	HT600	25365
		23810
		22124
		22180
		31170
	HT400+HT600	22183
		28898
		27346
		25441
		29364
	CT	2843
		2422
		2647
		2109
		2040

Appendix 8: R5A60° with $\theta = 45°$ and $\alpha = 7°$ fatigue test results.

Radius(R)Angle(A)	Heat Treatment	Equivalent cycles(2π)
R5A60°	As-Received	2025
		2506
		2577
		2122
		3310
	HT400	5711

		5927
		5879
		4680
		5890
	HT600	24397
		13132
		18778
		14257
		17817
	HT400+HT600	21136
		16627
		18242
		15871
		21088
	CT	3030
		3788
		2817
		2965
		3322

Appendix 9:Fatigue life test of homogeneity of variance

Test of Homogeneity of Variances

	Levene Statistic	df1	df2	Sig.
R7.5A40 (strain 3.18%)-Traditional Fatigue Test	2.720	4	20	.059
R7.5A40 (strain 3.18%)-Reciprocating Movement(±45°+7°)	10.810	4	20	.000
R10A60 (strain 3.44%)-Traditional Fatigue Test	.480	4	20	.750
R10A60 (strain 3.44%)-Reciprocating Movement(±45°+7°)	8.156	4	20	.000
R7.5A60 (strain 3.8%)-Traditional Fatigue Test	5.821	4	20	.003
R7.5A60 (strain 3.8%)-Reciprocating Movement(±45°+7°)	4.486	4	20	.009
R5.0A60 (strain 4.25%)-Traditional Fatigue Test	3.295	4	20	.031

R5.0A60 (strain 4.25%)-Reciprocating Movement(±45°+7°)	5.199	4	20	.005

Appendix 10: ANOVA results on fatigue life test

One-Way ANOVA (comparison between CR and PR)

		Sum of Squares	df	Mean Square	F	Sig.
R7.5A40 (strain 3.18%)-Traditional Fatigue Test	Between Groups	16985874.678	4	4246468.669	98.659	.000
	Within Groups	860837.052	20	43041.853		
	Total	17846711.730	24			
R7.5A40 (strain 3.18%)-Reciprocating Movement(±45°+7°)	Between Groups	2602226981.686	4	650556745.422	42.103	.000
	Within Groups	309032694.592	20	15451634.730		
	Total	2911259676.278	24			
R10A60 (strain 3.44%)-Traditional Fatigue Test	Between Groups	4936107.704	4	1234026.926	103.447	.000
	Within Groups	238581.916	20	11929.096		
	Total	5174689.620	24			
R10A60 (strain 3.44%)-Reciprocating Movement(±45°+7°)	Between Groups	2409464921.840	4	602366230.460	38.057	.000
	Within Groups	316560921.280	20	15828046.064		
	Total	2726025843.120	24			
R7.5A60 (strain 3.8%)-Traditional Fatigue Test	Between Groups	35916870.374	4	8979217.593	178.809	.000
	Within Groups	1004337.136	20	50216.857		
	Total	36921207.510	24			
R7.5A60 (strain 3.8%)-Reciprocating Movement(±45°+7°)	Between Groups	3069221141.594	4	767305285.398	164.273	.000
	Within Groups	93418419.368	20	4670920.968		
	Total	3162639560.962	24			
R5.0A60 (strain 4.25%)-Traditional Fatigue Test	Between Groups	18993985.014	4	4748496.254	167.503	.000
	Within Groups	566975.644	20	28348.782		
	Total	19560960.658	24			
R5.0A60 (strain 4.25%)-Reciprocating Movement(±45°+7°)	Between Groups	1266864540.182	4	316716135.046	59.996	.000
	Within Groups	105579612.332	20	5278980.617		
	Total	1372444152.514	24			

Appendix 11: post hoc test at p=0.05 on fatigue life

Multiple Comparisons

Dependent Variable		(I) Group	(J) Group	Mean Difference (I-J)	Std. Error	Sig.
R7.5A40 (strain 3.18%)-Traditional Fatigue Test	Bonferroni	As-Received	HT400	-2034.48000	131.21258	.000
			HT600	-1755.82000	131.21258	.000
			HT400+HT600	-1877.18000	131.21258	.000
			CT	-493.94000	131.21258	.012
		HT400	As-Received	2034.48000	131.21258	.000
			HT600	278.66000	131.21258	.464
			HT400+HT600	157.30000	131.21258	1.000
			CT	1540.54000	131.21258	.000
		HT600	As-Received	1755.82000	131.21258	.000
			HT400	-278.66000	131.21258	.464
			HT400+HT600	-121.36000	131.21258	1.000
			CT	1261.88000	131.21258	.000
		HT400+HT600	As-Received	1877.18000	131.21258	.000
			HT400	-157.30000	131.21258	1.000
			HT600	121.36000	131.21258	1.000
			CT	1383.24000	131.21258	.000
		CT	As-Received	493.94000	131.21258	.012
			HT400	-1540.54000	131.21258	.000
			HT600	-1261.88000	131.21258	.000
			HT400+HT600	-1383.24000	131.21258	.000
	Games-Howell	As-Received	HT400	-2034.48000	155.44903	.000
			HT600	-1755.82000	104.89637	.000
			HT400+HT600	-1877.18000	99.52228	.000
			CT	-493.94000	63.34483	.000
		HT400	As-Received	2034.48000	155.44903	.000
			HT600	278.66000	176.46232	.552
			HT400+HT600	157.30000	173.32163	.885
			CT	1540.54000	155.39714	.001
		HT600	As-Received	1755.82000	104.89637	.000
			HT400	-278.66000	176.46232	.552
			HT400+HT600	-121.36000	129.92011	.876
			CT	1261.88000	104.81946	.000
		HT400+HT600	As-Received	1877.18000	99.52228	.000
			HT400	-157.30000	173.32163	.885
			HT600	121.36000	129.92011	.876
			CT	1383.24000	99.44121	.000
		CT	As-Received	493.94000	63.34483	.000

			HT400	-1540.54000	155.39714	.001
			HT600	-1261.88000	104.81946	.000
			HT400+HT600	-1383.24000	99.44121	.000
R7.5A40 (strain 3.18%)-Reciprocating Movement(±45°+7°)	Bonferroni	As-Received	HT400	-7432.40000	2486.09209	.072
			HT600	-26042.60000	2486.09209	.000
			HT400+HT600	-20750.80000	2486.09209	.000
			CT	-2861.74000	2486.09209	1.000
		HT400	As-Received	7432.40000	2486.09209	.072
			HT600	-18610.20000	2486.09209	.000
			HT400+HT600	-13318.40000	2486.09209	.000
			CT	4570.66000	2486.09209	.809
		HT600	As-Received	26042.60000	2486.09209	.000
			HT400	18610.20000	2486.09209	.000
			HT400+HT600	5291.80000	2486.09209	.459
			CT	23180.86000	2486.09209	.000
		HT400+HT600	As-Received	20750.80000	2486.09209	.000
			HT400	13318.40000	2486.09209	.000
			HT600	-5291.80000	2486.09209	.459
			CT	17889.06000	2486.09209	.000
		CT	As-Received	2861.74000	2486.09209	1.000
			HT400	-4570.66000	2486.09209	.809
			HT600	-23180.86000	2486.09209	.000
			HT400+HT600	-17889.06000	2486.09209	.000
	Games-Howell	As-Received	HT400	-7432.40000	726.24456	.000
			HT600	-26042.60000	2883.44965	.004
			HT400+HT600	-20750.80000	2597.96244	.006
			CT	-2861.74000	352.39868	.001
		HT400	As-Received	7432.40000	726.24456	.000
			HT600	-18610.20000	2943.79547	.011
			HT400+HT600	-13318.40000	2664.78117	.026
			CT	4570.66000	689.80770	.008
		HT600	As-Received	26042.60000	2883.44965	.004
			HT400	18610.20000	2943.79547	.011
			HT400+HT600	5291.80000	3858.48538	.660
			CT	23180.86000	2874.48872	.006
		HT400+HT600	As-Received	20750.80000	2597.96244	.006
			HT400	13318.40000	2664.78117	.026
			HT600	-5291.80000	3858.48538	.660
			CT	17889.06000	2588.01320	.010
		CT	As-Received	2861.74000	352.39868	.001
			HT400	-4570.66000	689.80770	.008

			HT600	-23180.86000	2874.48872	.006
			HT400+HT600	-17889.06000	2588.01320	.010
R10A60 (strain 3.44%)-Traditional Fatigue Test	Bonferroni	As-Received	HT400	-1040.62000	69.07705	.000
			HT600	-1031.38000	69.07705	.000
			HT400+HT600	-950.90000	69.07705	.000
			CT	-230.30000	69.07705	.033
		HT400	As-Received	1040.62000	69.07705	.000
			HT600	9.24000	69.07705	1.000
			HT400+HT600	89.72000	69.07705	1.000
			CT	810.32000	69.07705	.000
		HT600	As-Received	1031.38000	69.07705	.000
			HT400	-9.24000	69.07705	1.000
			HT400+HT600	80.48000	69.07705	1.000
			CT	801.08000	69.07705	.000
		HT400+HT600	As-Received	950.90000	69.07705	.000
			HT400	-89.72000	69.07705	1.000
			HT600	-80.48000	69.07705	1.000
			CT	720.60000	69.07705	.000
		CT	As-Received	230.30000	69.07705	.033
			HT400	-810.32000	69.07705	.000
			HT600	-801.08000	69.07705	.000
			HT400+HT600	-720.60000	69.07705	.000
	Games-Howell	As-Received	HT400	-1040.62000	65.89751	.000
			HT600	-1031.38000	76.92418	.000
			HT400+HT600	-950.90000	77.16112	.000
			CT	-230.30000	72.06547	.074
		HT400	As-Received	1040.62000	65.89751	.000
			HT600	9.24000	62.77861	1.000
			HT400+HT600	89.72000	63.06872	.635
			CT	810.32000	56.72087	.000
		HT600	As-Received	1031.38000	76.92418	.000
			HT400	-9.24000	62.77861	1.000
			HT400+HT600	80.48000	74.51517	.812
			CT	801.08000	69.22502	.000
		HT400+HT600	As-Received	950.90000	77.16112	.000
			HT400	-89.72000	63.06872	.635
			HT600	-80.48000	74.51517	.812
			CT	720.60000	69.48822	.000
		CT	As-Received	230.30000	72.06547	.074
			HT400	-810.32000	56.72087	.000
			HT600	-801.08000	69.22502	.000

			HT400+HT600	-720.60000	69.48822	.000
R10A60 (strain 3.44%)-Reciprocating Movement(±45°+7°)	Bonferroni	As-Received	HT400	-1288.60000	2516.19125	1.000
			HT600	-22001.00000	2516.19125	.000
			HT400+HT600	-19249.80000	2516.19125	.000
			CT	-758.50000	2516.19125	1.000
		HT400	As-Received	1288.60000	2516.19125	1.000
			HT600	-20712.40000	2516.19125	.000
			HT400+HT600	-17961.20000	2516.19125	.000
			CT	530.10000	2516.19125	1.000
		HT600	As-Received	22001.00000	2516.19125	.000
			HT400	20712.40000	2516.19125	.000
			HT400+HT600	2751.20000	2516.19125	1.000
			CT	21242.50000	2516.19125	.000
		HT400+HT600	As-Received	19249.80000	2516.19125	.000
			HT400	17961.20000	2516.19125	.000
			HT600	-2751.20000	2516.19125	1.000
			CT	18491.30000	2516.19125	.000
		CT	As-Received	758.50000	2516.19125	1.000
			HT400	-530.10000	2516.19125	1.000
			HT600	-21242.50000	2516.19125	.000
			HT400+HT600	-18491.30000	2516.19125	.000
	Games-Howell	As-Received	HT400	-1288.60000	485.72811	.164
			HT600	-22001.00000	3181.05033	.010
			HT400+HT600	-19249.80000	2364.77659	.005
			CT	-758.50000	284.72566	.179
		HT400	As-Received	1288.60000	485.72811	.164
			HT600	-20712.40000	3197.11490	.012
			HT400+HT600	-17961.20000	2386.34256	.006
			CT	530.10000	428.40540	.735
		HT600	As-Received	22001.00000	3181.05033	.010
			HT400	20712.40000	3197.11490	.012
			HT400+HT600	2751.20000	3946.86967	.951
			CT	21242.50000	3172.80327	.012
		HT400+HT600	As-Received	19249.80000	2364.77659	.005
			HT400	17961.20000	2386.34256	.006
			HT600	-2751.20000	3946.86967	.951
			CT	18491.30000	2353.67111	.007
		CT	As-Received	758.50000	284.72566	.179
			HT400	-530.10000	428.40540	.735
			HT600	-21242.50000	3172.80327	.012
			HT400+HT600	-18491.30000	2353.67111	.007

R7.5A60 (strain 3.8%)-Traditional Fatigue Test	Bonferroni	As-Received	HT400	-958.14000	141.72771	.000
			HT600	-2859.38000	141.72771	.000
			HT400+HT600	-2512.48000	141.72771	.000
			CT	-85.02000	141.72771	1.000
		HT400	As-Received	958.14000	141.72771	.000
			HT600	-1901.24000	141.72771	.000
			HT400+HT600	-1554.34000	141.72771	.000
			CT	873.12000	141.72771	.000
		HT600	As-Received	2859.38000	141.72771	.000
			HT400	1901.24000	141.72771	.000
			HT400+HT600	346.90000	141.72771	.237
			CT	2774.36000	141.72771	.000
		HT400+HT600	As-Received	2512.48000	141.72771	.000
			HT400	1554.34000	141.72771	.000
			HT600	-346.90000	141.72771	.237
			CT	2427.46000	141.72771	.000
		CT	As-Received	85.02000	141.72771	1.000
			HT400	-873.12000	141.72771	.000
			HT600	-2774.36000	141.72771	.000
			HT400+HT600	-2427.46000	141.72771	.000
	Games-Howell	As-Received	HT400	-958.14000	123.72497	.003
			HT600	-2859.38000	151.85297	.000
			HT400+HT600	-2512.48000	119.60688	.000
			CT	-85.02000	50.08022	.489
		HT400	As-Received	958.14000	123.72497	.003
			HT600	-1901.24000	187.23714	.000
			HT400+HT600	-1554.34000	162.18578	.000
			CT	873.12000	120.44272	.006
		HT600	As-Received	2859.38000	151.85297	.000
			HT400	1901.24000	187.23714	.000
			HT400+HT600	346.90000	184.54182	.401
			CT	2774.36000	149.19084	.000
		HT400+HT600	As-Received	2512.48000	119.60688	.000
			HT400	1554.34000	162.18578	.000
			HT600	-346.90000	184.54182	.401
			CT	2427.46000	116.20838	.000
		CT	As-Received	85.02000	50.08022	.489
			HT400	-873.12000	120.44272	.006
			HT600	-2774.36000	149.19084	.000
			HT400+HT600	-2427.46000	116.20838	.000
R7.5A60 (strain	Bonferroni	As-Received	HT400	-3112.80000	1366.88273	.339

3.8%)-Reciprocating Movement(±45°+7°)			HT600	-22727.40000	1366.88273	.000
			HT400+HT600	-24444.00000	1366.88273	.000
			CT	-210.02000	1366.88273	1.000
		HT400	As-Received	3112.80000	1366.88273	.339
			HT600	-19614.60000	1366.88273	.000
			HT400+HT600	-21331.20000	1366.88273	.000
			CT	2902.78000	1366.88273	.464
		HT600	As-Received	22727.40000	1366.88273	.000
			HT400	19614.60000	1366.88273	.000
			HT400+HT600	-1716.60000	1366.88273	1.000
			CT	22517.38000	1366.88273	.000
		HT400+HT600	As-Received	24444.00000	1366.88273	.000
			HT400	21331.20000	1366.88273	.000
			HT600	1716.60000	1366.88273	1.000
			CT	24233.98000	1366.88273	.000
		CT	As-Received	210.02000	1366.88273	1.000
			HT400	-2902.78000	1366.88273	.464
			HT600	-22517.38000	1366.88273	.000
			HT400+HT600	-24233.98000	1366.88273	.000
	Games-Howell	As-Received	HT400	-3112.80000	374.90159	.000
			HT600	-22727.40000	1685.35062	.001
			HT400+HT600	-24444.00000	1328.72485	.000
			CT	-210.02000	270.31339	.930
		HT400	As-Received	3112.80000	374.90159	.000
			HT600	-19614.60000	1697.61026	.001
			HT400+HT600	-21331.20000	1344.24090	.000
			CT	2902.78000	338.44233	.001
		HT600	As-Received	22727.40000	1685.35062	.001
			HT400	19614.60000	1697.61026	.001
			HT400+HT600	-1716.60000	2122.93172	.920
			CT	22517.38000	1677.61697	.001
		HT400+HT600	As-Received	24444.00000	1328.72485	.000
			HT400	21331.20000	1344.24090	.000
			HT600	1716.60000	2122.93172	.920
			CT	24233.98000	1318.90171	.000
		CT	As-Received	210.02000	270.31339	.930
			HT400	-2902.78000	338.44233	.001
			HT600	-29911.4357	1677.61697	.001
			HT400+HT600	-30016.6196	1318.90171	.000
R5.0A60 (strain 4.25%)-Traditional Fatigue Test	Bonferroni	As-Received	HT400	-679.40000	106.48715	.000
			HT600	-1729.28000	106.48715	.000

			HT400+HT600	-2145.92000	106.48715	.000
			CT	-61.66000	106.48715	1.000
		HT400	As-Received	679.40000	106.48715	.000
			HT600	-1049.88000	106.48715	.000
			HT400+HT600	-1466.52000	106.48715	.000
			CT	617.74000	106.48715	.000
		HT600	As-Received	1729.28000	106.48715	.000
			HT400	1049.88000	106.48715	.000
			HT400+HT600	-416.64000	106.48715	.009
			CT	1667.62000	106.48715	.000
		HT400+HT600	As-Received	2145.92000	106.48715	.000
			HT400	1466.52000	106.48715	.000
			HT600	416.64000	106.48715	.009
			CT	2084.26000	106.48715	.000
		CT	As-Received	61.66000	106.48715	1.000
			HT400	-617.74000	106.48715	.000
			HT600	-1667.62000	106.48715	.000
			HT400+HT600	-2084.26000	106.48715	.000
	Games-Howell	As-Received	HT400	-679.40000	53.05608	.000
			HT600	-1729.28000	123.40094	.001
			HT400+HT600	-2145.92000	104.54038	.000
			CT	-61.66000	27.46206	.258
		HT400	As-Received	679.40000	53.05608	.000
			HT600	-1049.88000	130.86200	.002
			HT400+HT600	-1466.52000	113.25089	.000
			CT	617.74000	51.49016	.000
		HT600	As-Received	1729.28000	123.40094	.001
			HT400	1049.88000	130.86200	.002
			HT400+HT600	-416.64000	158.86664	.158
			CT	1667.62000	122.73582	.001
		HT400+HT600	As-Received	2145.92000	104.54038	.000
			HT400	1466.52000	113.25089	.000
			HT600	416.64000	158.86664	.158
			CT	2084.26000	103.75442	.000
		CT	As-Received	61.66000	27.46206	.258
			HT400	-617.74000	51.49016	.000
			HT600	-1667.62000	122.73582	.001
			HT400+HT600	-2084.26000	103.75442	.000
R5.0A60 (strain 4.25%)-Reciprocating Movement(±45°+7°)	Bonferroni	As-Received	HT400	-3109.40000	1453.13188	.449
			HT600	-19750.5068	1453.13188	.000
			HT400+HT600	-20667.1068	1453.13188	.000

			CT	-676.76000	1453.13188	1.000
		HT400	As-Received	3109.40000	1453.13188	.449
			HT600	-16641.1068	1453.13188	.000
			HT400+HT600	-17557.7068	1453.13188	.000
			CT	2432.64000	1453.13188	1.000
		HT600	As-Received	15168.20000	1453.13188	.000
			HT400	12058.80000	1453.13188	.000
			HT400+HT600	-916.60000	1453.13188	1.000
			CT	14491.44000	1453.13188	.000
		HT400+HT600	As-Received	16084.80000	1453.13188	.000
			HT400	12975.40000	1453.13188	.000
			HT600	916.60000	1453.13188	1.000
			CT	15408.04000	1453.13188	.000
		CT	As-Received	676.76000	1453.13188	1.000
			HT400	-2432.64000	1453.13188	1.000
			HT600	-19073.7468	1453.13188	.000
			HT400+HT600	-19990.3468	1453.13188	.000
	Games-Howell	As-Received	HT400	-3109.40000	328.35432	.000
			HT600	-23930.0846	1997.17146	.007
			HT400+HT600	-20667.1068	1120.70890	.000
			CT	-676.76000	284.63991	.221
		HT400	As-Received	3109.40000	328.35432	.000
			HT600	-16641.1068	1998.37059	.016
			HT400+HT600	-17557.7068	1122.84442	.001
			CT	2432.64000	292.93521	.000
		HT600	As-Received	15168.20000	1997.17146	.007
			HT400	12058.80000	1998.37059	.016
			HT400+HT600	-916.60000	2267.52219	.993
			CT	14491.44000	1991.65467	.008
		HT400+HT600	As-Received	16084.80000	1120.70890	.000
			HT400	12975.40000	1122.84442	.001
			HT600	916.60000	2267.52219	.993
			CT	15408.04000	1110.84784	.001
		CT	As-Received	676.76000	284.63991	.221
			HT400	-2432.64000	292.93521	.000
			HT600	-19073.7468	1991.65467	.008
			HT400+HT600	-19990.3468	1110.84784	.001

Appendix 12: post hoc test for cutting efficiency evaluation in different position

Multiple Comparisons

Dependent Variable:SUM

	(I) MM	(J) MM	Mean Difference (I-J)	Std. Error	Sig.	95% Confidence Interval	
						Lower Bound	Upper Bound
Bonferroni	2~4.5mm	4.5~7mm	-.22300	.01979	.000	-.2755	-.1705
		7~9.5mm	-.50667	.01979	.000	-.5592	-.4542
		9.5~12mm	-.98956	.01979	.000	-1.0421	-.9371
	4.5~7mm	2~4.5mm	.22300	.01979	.000	.1705	.2755
		7~9.5mm	-.28367	.01979	.000	-.3362	-.2312
		9.5~12mm	-.76656	.01979	.000	-.8191	-.7141
	7~9.5mm	2~4.5mm	.50667	.01979	.000	.4542	.5592
		4.5~7mm	.28367	.01979	.000	.2312	.3362
		9.5~12mm	-.48289	.01979	.000	-.5354	-.4304
	9.5~12mm	2~4.5mm	.98956	.01979	.000	.9371	1.0421
		4.5~7mm	.76656	.01979	.000	.7141	.8191
		7~9.5mm	.48289	.01979	.000	.4304	.5354
Games-Howell	2~4.5mm	4.5~7mm	-.22300	.01244	.000	-.2553	-.1907
		7~9.5mm	-.50667	.01469	.000	-.5449	-.4685
		9.5~12mm	-.98956	.02246	.000	-1.0482	-.9309
	4.5~7mm	2~4.5mm	.22300	.01244	.000	.1907	.2553
		7~9.5mm	-.28367	.01670	.000	-.3270	-.2403
		9.5~12mm	-.76656	.02382	.000	-.8286	-.7046
	7~9.5mm	2~4.5mm	.50667	.01469	.000	.4685	.5449
		4.5~7mm	.28367	.01670	.000	.2403	.3270
		9.5~12mm	-.48289	.02507	.000	-.5480	-.4177
	9.5~12mm	2~4.5mm	.98956	.02246	.000	.9309	1.0482
		4.5~7mm	.76656	.02382	.000	.7046	.8286
		7~9.5mm	.48289	.02507	.000	.4177	.5480

Appendix 13: post hoc test for cutting efficiency evaluation in different HT

Bonferroni	(I) Group	(J) Group	Mean Difference (I-J)	Std. Error	Sig.
Position1	As-Received	HT 400	0.02667	0.01361	0.801
		HT 600	0.12467	0.01361	0
		HT400 + CT	0.024	0.01361	1
		HT600 + CT	0.10533	0.01361	0
		HT400+HT600	0.13	0.01361	0
Position2	As-Received	HT 400	0.05067	0.01856	0.116
		HT 600	0.20133	0.01856	0
		HT400 + CT	0.03133	0.01856	1
		HT600 + CT	0.164	0.01856	0

		HT400+HT600	0.21333	0.01856	0
Position3	As-Received	HT 400	0.06267	0.0227	0.106
		HT 600	0.268	0.0227	0
		HT400 + CT	0.026	0.0227	1
		HT600 + CT	0.13867	0.0227	0
		HT400+HT600	0.26333	0.0227	0
Position4	As-Received	HT 400	0.02667	0.01432	0.446
		HT 600	0.12467	0.01554	0
		HT400 + CT	0.024	0.0136	0.505
		HT600 + CT	0.10533	0.01515	0
		HT400+HT600	0.13	0.01374	0

Publications

1. C.S. Shin, C.Y. Liu, S.C. Hsu, “In-situ Fatigue Crack Initiation Monitoring in NiTi Rotary Endodontic Instruments,” Advanced Material Research, 2013;647:3-8. (EI)
2. C.Y. Liu, C.S. Shin, “Application of Fiber Bragg Grating Sensors in Monitoring Fatigue Failure of NiTi Rotary Endodontic Instruments,” Smart Materials and Nanotechnology in Engineering, Proc. SPIE 84091V, 2012. (EI)
3. P. Baldeck, P. Prabakharan, C.Y. Liu, M. Bouriau, L. Gedy, O. Stephan, T. Vergote, H. Chaumeil, J.P. Malval, Y.H. Lee, C.L. Lin, C.T. Lin, Y.H. Hsueh, T.T. Chung, “Recent Advances in Two-Photon 3D Laser Lithography with Self-Q-Switched Nd:YAG microchip lasers,” Optical Processes in Organic Materials and Nanostructures, Proc. SPIE 8827E, 2013. (EI)
4. C.S. Shin, C.Y. Liu, C.P. Lin, “Frequency and temperature effects on fatigue of endodontic instruments,” Biological Medical and Chemical Engineering, Proc. DESTech, 2013. (EI)
5. C.Y. Liu, C.S. Shin, C.P. Lin, “Monitoring system for warning fatigue crack in NiTi rotary instruments in clinical therapy,” J Formosa Medical Association. (to be submitted) (SCI)
6. C.Y. Liu, C.S. Shin, C.P. Lin, “The quantitative analysis of mechanical properties in NiTi rotary endodontic instruments,” PLOS One (to be submitted) (SCI)
7. C.Y. Liu, P. Baldeck, “Two-photon-polymerization in mm-size structure byamplified Nd:YAG microchip laser,” Optical Express (to be submitted) (SCI)